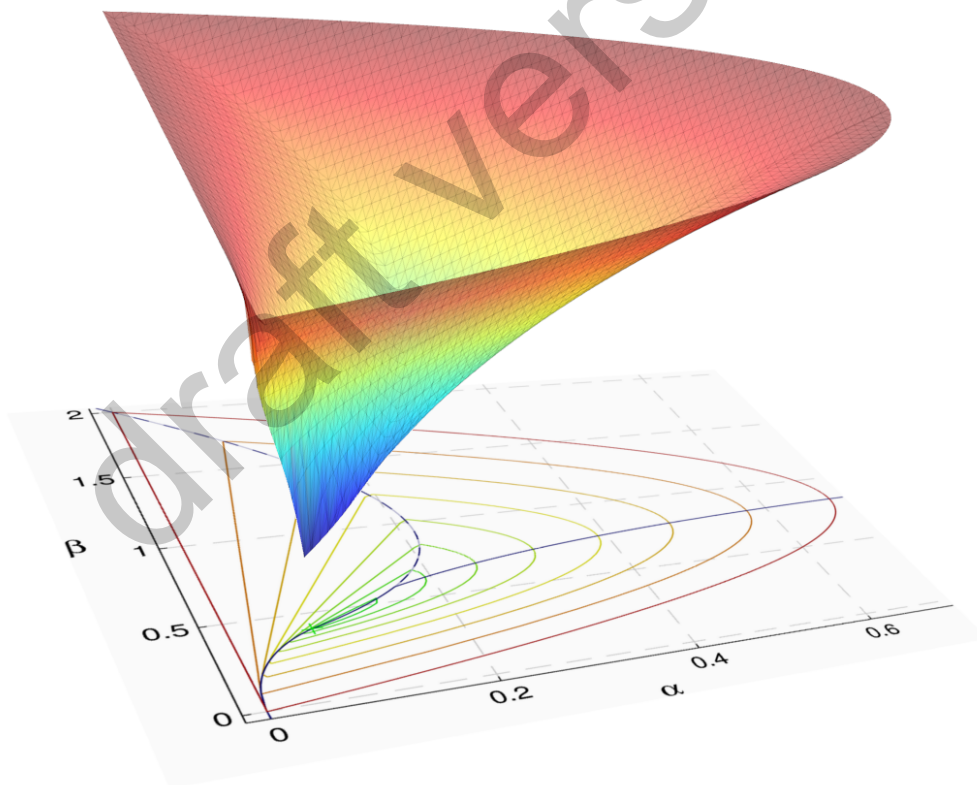


Control of Hybrid Systems Affected by Time Delay with Application in Haptic Rendering

Von der Fakultät für Maschinenbau
der Gottfried Wilhelm Leibniz Universität Hannover
zur Erlangung des akademischen Grades
Doktor-Ingenieur
genehmigte Dissertation

von

Dipl.-Ing. Thomas Hulin



2017

1. Referent: Prof. Dr.-Ing. Tobias Ortmaier
 2. Referent: Prof. Dr.-Ing. Eduard Reithmeier
- Tag der Promotion: 18. Januar 2017

Preface

Interacting with a virtual environment without perceiving haptic feedback is like eating without smelling the delicious fragrance of the food or watching a movie without hearing its impressive sound effects. Researching on haptic feedback has been my main research interest in the past years, since I started my work as a young researcher at the Institute of Robotics and Mechatronics. This thesis summarizes important results of my research on haptic control carried out at the Institute of Robotics and Mechatronics at the DLR (German Aerospace Center). I have already published parts of this work within several conference and journal papers and the present thesis contains text passages from these publications. The introductory sections of the respective chapters contain appropriate references accordingly.

It is important to me to mention that the findings of my research do not only apply to haptic systems but in fact to a wide variety of physical systems. This is mainly due to electromechanical analogies [13] and the analytical representation of the investigated hybrid control system. Hence, I hope that my findings will also inspire and advance the research in domains other than haptics. To this end, I tried to present the results as clear as possible in an understandable language with numerous meaningful figures, and I want to motivate other researchers to also put emphasis on a clear and comprehensible form of presentation of their research activities.

A lot of people supported me in conducting my research and made this thesis possible. In particular, I would like to express my gratitude to the following people for their valuable and constructive support. First of all, I would like to thank Professor Gerhard Hirzinger, the former head of the institute, who largely founded this great institute and who managed to create an amazingly inspiring working atmosphere. My particular thanks go also to Professor Alin Albu-Schäffer, the head of the DLR's Institute of Robotics and Mechatronics, who understands well how to motivate his colleagues in publishing their research activities and writing doctoral theses. Christian Ott, the head of the department for Analysis and Control of Advanced Robotic Systems, created the freedom for me to work on my research topics and to finalize the thesis. It is a great privilege to work in this institute and in this research department.

I want to thank Professor Jürgen Ackermann and Naim Bajcinca, who introduced me into the fascinating field of parameter space control design during my diploma thesis under their supervision. I have learned a lot during these few months of work and, more importantly, the interest in this topic has never left me since. Professor Tobias Ortmaier deserves my special thanks for supervising my doctoral studies and

providing valuable advices for improving the thesis.

I want to express my particular gratitude to Carsten Preusche for establishing the research group for telepresence and virtual reality, of which I have been a member since I started working at DLR. He inspired my work with a remarkable number of various ideas. My special thanks go also to the whole research group for telepresence and virtual reality, and all the colleagues that were involved in building the amazing robotic systems that I could use for conducting my research work.

I gratefully acknowledge the fruitful and constructive collaboration with Bernhard Vodermayr in the international research project STAMAS. My sincere thanks also go to my office mates Joseph Reill, Andreas Tobergte, and Phillip Schmidt, who often had to listen to my desperation and who encouraged me in finalizing my thesis. I also thank all my students in supporting me in my research activities. The reviewers and editors of my scientific publications also deserve my gratitude, as they provided valuable input and excellent suggestions for improvements.

My special thanks go to Jorge Juan Gil, who shared with me his extensive experience and knowledge in the field of stable haptic control and who get never tired to discuss on control issues. I have learned a lot from him during the six months that he was visiting our institute as a guest scientist, and also afterwards during numerous short visits and intense discussions.

There are three persons to whom I want to express my sincerest gratitude: Philipp Kremer, Katharina Hertkorn, and Mikel Sagardia, who proofread this thesis and also motivated and pushed me to finalize it. They had invested hours of their time and I sincerely appreciate their excellent ideas and comments. Also, my grateful thanks go to Anja Hellings and Phillip Schmidt for proofreading parts of this thesis.

I want to express my gratitude to the VR-Lab of the Volkswagen AG, which funded a research project on haptic assembly simulations. I also acknowledge the support from the EU for funding three research projects that I have worked on, in particular ENACTIVE (IST-2004-002114), SKILLS (FP6-IST-035005), and STAMAS (Project reference: 312815). Finally, I would like to thank the reader in advance for taking the time to read this thesis and I am convinced that the time spent is a worthwhile investment.

Oberpfaffenhofen, January 2017

Thomas Hulin

The pictures on the cover page show (i) the haptic device HUG that was used for the experiments (photo: DLR, CC-BY 3.0), (ii) the investigated model, and (iii) a three-dimensional illustration of the left contour plot of Fig. 5.2. The lower tip of this three dimensional-shape is the optimum point with respect to the pole-based settling time.

Abstract

Haptic rendering denotes the process of computing and displaying forces from a virtual environment to a human operator via a haptic device. From the control point of view, the haptic system comprising virtual environment, haptic device, and human operator is a hybrid control system that contains both discrete- and continuous-time elements. Discrete-time sampling as well as time delay that is typically present in such haptic systems may lead to unstable behavior.

This thesis investigates stability, passivity, and control design of such hybrid system. Its primary goal is to close some of the existing lacks in the current state of research, in particular to analyze the influence of the human operator on a haptic system behavior, to investigate the precise effect of delay and discrete-time sampling, and to introduce optimal control methods to the field of haptic rendering. A unique characteristic of the presented approach is the exact combination of discrete- and continuous-time elements, while taking into account time delay and user dynamics.

A linear stability analysis is presented to determine the stability boundaries of the haptic system and to investigate the influence of both delay and human operator. This analysis leads to the definition of normalized dimensionless parameters greatly simplifying calculations and presentation of results. The analysis reveals that the human operator modeled as mass-spring-damper system has a stabilizing effect, which is mainly constituted by its mass contribution. For small parameter values of the virtual environment, the relationship between the parameters may be approximated by a linear stability condition.

Passivity is analyzed by enhancing an existing passivity approach towards delayed haptic systems. The influence of the system parameters on passivity is completely different than for stability. For realistic parameter values, passive regions result as small subregions of the stable regions, which emphasizes the fact that passivity is highly conservative with regard to stability. This is because passivity admits human arm stiffnesses that are orders of magnitudes higher than realistically feasible.

To analyze the performance of a haptic system, various optimization criteria are investigated that are either based on the system poles or on the transient response. Each of these criteria is based on a dimensionless performance measure resulting in cost maps and in optimal points that hold for any positive mass and sampling rate. A polynomial approximation function is found to predict the optimal performance of the haptic system in these optimal points under the influence of delay. This function leads to the formulation of an easy-to-remember rule of thumb for the optimal settling time.

The theoretical investigations are accompanied by a series of experiments on two different devices, a Novint Falcon and a DLR/KUKA light-weight robot. They exhibit a remarkable accordance to the theoretical results. The practical impact of this thesis on haptic rendering applications was already demonstrated in haptic assembly simulations and haptically supported training. In addition, the theoretical results lead to design guidelines of haptic devices and provide the theoretical basis for future psychophysical studies.

Keywords: haptic rendering, time delay, stability analysis, passivity analysis, optimal control

Kurzfassung

Titel der Arbeit: Regelung totzeitbehafteter hybrider Systeme mit Anwendung für haptisches Rendern

Haptisches Rendern beschreibt die Berechnung von Kräften aus der virtuellen Welt und deren Darstellung an den Menschen über ein haptisches Gerät. Aus regelungstechnischer Sicht ist das haptische System bestehend aus virtueller Umgebung, haptischem Gerät und dem Menschen ein hybrides System, das sowohl zeitdiskrete als auch zeitkontinuierliche Elemente enthält. Die zeitdiskrete Abtastung sowie eine zusätzliche Totzeit, die typischerweise in solchen haptischen Systemen vorhanden ist, können zu einem instabilen Systemverhalten führen.

Diese Dissertationsschrift untersucht Stabilität, Passivität und den Reglerentwurf für solche hybriden Systeme. Das primäre Ziel dieser Arbeit ist es einige grundlegende Lücken im Stand der Forschung auf diesem Gebiet zu schließen. Im einzelnen wird der Einfluss des Menschen auf das Verhalten haptischer Systeme analysiert, die genaue Auswirkung von Totzeit und zeitdiskreter Abtastung untersucht und Methoden der optimalen Regelung in das Gebiet des haptischen Renderns eingeführt. Ein Alleinstellungsmerkmal des vorgestellten Ansatzes ist die exakte Kombination von zeitdiskreten und -kontinuierlichen Elementen unter gleichzeitiger Berücksichtigung von Totzeit und der Dynamik des Benutzers.

In einer linearen Stabilitätsanalyse werden die Stabilitätsgrenzen des haptischen Systems bestimmt und untersucht, wie sie sich durch die Totzeit und den Benutzer verändern. Die Analyse führt zu normierten, dimensionslosen Parametern, mit denen sich die Berechnungen stark vereinfachen lassen und die eine klare Präsentation der Ergebnisse ermöglichen. Sie offenbart auch, dass der Mensch, als Masse-Feder-Dämpfer System modelliert, stabilisierend auf das haptische System wirkt, was hauptsächlich an der zusätzlich eingebrachten Trägheit liegt. Für kleine Parameterwerte der virtuellen Wand kann das Verhältnis zwischen den Parametern durch eine lineare Stabilitätsbedingung angenähert werden.

Passivität wird unter Verwendung eines existierenden Passivitätsansatzes für haptische Systeme analysiert, der dazu bezüglich Totzeiten verallgemeinert wird. Es zeigt sich, dass sich der Einfluss der Systemparameter auf Passivität strukturell von dem für Stabilität unterscheidet. Für realistische Parameterwerte resultieren darüber hinaus die passiven Parametergebiete als Teile der stabilen Gebiete. Dies unterstreicht die Tatsache, dass Passivität stark konservativ bezüglich Stabilität ist. Der Grund dafür liegt in dem von der Passivitätsanalyse betrachteten Steifigkeitsbereich des menschlichen

Arms, der realistische Werte um Größenordnungen übersteigt.

Die Performanz haptischer Systeme wird anhand verschiedenartiger Optimierungskriterien untersucht, die entweder auf der Lage der Systempole oder auf dem Einschwingverhalten basieren. Für jedes dieser Kriterien wird ein dimensionsloses Performanzmaß eingeführt, mit welchem Kostenkarten und optimale Punkte berechnet werden können, die unabhängig von der Masse und der Abtastrate sind. Mit Hilfe einer polynomischen Approximationsfunktion lässt sich die optimale Performanz des haptischen Systems unter dem Einfluss der Totzeit vorhersagen. Diese Funktion führt außerdem zu einer leicht zu merkenden Faustregel für die optimale Einschwingzeit.

Die theoretischen Untersuchungen werden von einer Reihe an Experimenten an zwei unterschiedlichen Geräten begleitet, einem Novint Falcon und einem DLR/KUKA Leichtbauroboter. Sie weisen bemerkenswerte Übereinstimmungen zu den theoretischen Ergebnissen auf. Der praktische Nutzen der in dieser Dissertationsschrift neu vorgestellten Erkenntnisse konnte bereits erfolgreich in zwei Anwendungen demonstriert werden, in einer haptischen Einbausimulation und in haptisch unterstütztem Training. Darüber hinaus führen die theoretischen Ergebnisse zu Gestaltungsrichtlinien für haptische Geräte und liefern die theoretische Grundlage für zukünftige psychophysische Studien.

Schlagnworte: haptisches Rendern, Totzeit, Stabilitätsanalyse, Passivitätsanalyse, optimale Regelung

Table of Contents

Titlepage	i
Preface	iii
Abstract	v
Kurzfassung	vii
Table of Contents	xi
Notations	xiii
1 Introduction	1
1.1 Fields of Application	3
1.2 Technological Developments	4
1.3 Motivation and Problem Definition	5
1.4 Key Contributions and Thesis Structure	5
2 Control Approaches for Haptic Rendering	7
2.1 Stability-based Approaches	8
2.2 Passivity-based Approaches	10
2.3 Discussion	12
3 Stability Analysis	15
3.1 System Description	15
3.1.1 Haptic Device	16
3.1.2 Virtual Environment	16
3.1.3 Time Delay	16
3.1.4 Human Arm	17
3.1.5 Control Loop	18
3.2 Closed-Loop Transfer Function	19
3.2.1 Discrete-Time Equivalent	19
3.2.2 Normalized Characteristic Polynomial	19
3.3 Parameter Range	21

3.4	Stability Boundaries	23
3.5	Linear Stability Condition	28
3.6	Discussion	30
4	Passivity Analysis	33
4.1	Passivity Condition	34
4.2	Passivity Boundaries	35
4.3	Comparison of Passivity to Stability	37
4.3.1	Relation between Passivity and Stability Boundaries	38
4.3.2	Maximum Passive and Stable Stiffness	39
4.3.3	Passivity and Robust Stability	39
4.4	Discussion	43
5	Control Design	45
5.1	Pole-based Design	46
5.1.1	Minimum Settling Time	47
5.1.2	Maximum Damping	49
5.2	Response-based Design	50
5.2.1	Minimum Settling Time	52
5.2.2	Minimum Overshoot	56
5.2.3	Minimal System Energy	59
5.3	Relation to Continuous-Time Design Criteria	63
5.4	Influence of Delay	66
5.4.1	Influence of Delay on the Optimal Parameters	66
5.4.2	Influence of Delay on the Optimal Costs	68
5.5	Discussion	71
6	Experiments	75
6.1	Experiments with the Novint Falcon	75
6.1.1	Experimental Setup and Procedure	76
6.1.2	System Parameter Estimation	77
6.1.3	Stability Boundaries	80
6.1.4	Cost Maps for Optimal Control Design	82
6.2	Experiments with the Light-Weight Robot	88
6.2.1	Experimental Setup and Procedure	88
6.2.2	System Parameter Estimation	90
6.2.3	Stability Boundaries	90
6.2.4	Cost Maps for Optimal Control Design	90
6.2.5	Influence of Delay on the Optimal Costs	95
6.3	Discussion	95

7 Conclusion	99
7.1 Summary	99
7.1.1 Stability	100
7.1.2 Passivity	100
7.1.3 Optimal Control	101
7.1.4 Experiments	101
7.2 Future Research Work and Perspectives	102
A Discrete-Time Equivalentents	105
A.1 Damped Mass	105
A.2 Mass-Spring-Damper System	107
B Tables for the Influence of Delay	109
C Tables for Optimal Control Design	113
C.1 No Delay ($d=0$)	114
C.2 One Sampling Step Delay ($d=1$)	116
C.3 Two Sampling Steps Delay ($d=2$)	118
D Experimental Results	121
D.1 Falcon	121
D.2 LWR	123
E Electrical Analogon	125
Bibliography	137

Notations

List of Abbreviations

Table 1: Abbreviations

abbreviation	description
BIBO stability	bounded input-bounded output stability
CAD	computer-aided design
DLR	German Aerospace Center
DoF	degree of freedom
ISE	integral of the square of the error
ITSE	integral of time multiplied by the squared error
ISTSE	integral of squared time multiplied by the squared error
LWR	Light-Weight Robot
VR	virtual reality
ZOH	zero-order hold

List of Mathematical Abbreviations

Table 2: Mathematical abbreviations

operator	description
$\cos(\cdot)$	cosine function
$\deg(\cdot)$	degree of a polynomial
$\ln(\cdot)$	natural logarithm
$\max(\cdot)$	maximum of a set or function
$\min(\cdot)$	minimum of a set or function
$\sin(\cdot)$	sine function

Conventions

Throughout this dissertation, italic letters indicate scalars while vectors and matrices are denoted by bold letters. Dots denote derivatives with respect to time t .

Table 3: Subscripts and superscripts

sub-/superscripts	description
x_D	parameter x associated with the haptic device
x_E	parameter x associated with an energy
x_F	parameter x associated with a force
x_H	parameter x associated with the human operator
x_k	parameter x at time instant $t = k \cdot T$ with $k \in \mathbb{N}_0$
x_{\max}	maximum value of parameter x
x_{obs}	observed value of parameter x
x_{opt}	optimal value of parameter x
x_{ov}	parameter x associated with the relative overshoot
x_{rot}	parameter x for a rotational movement
x_{settle}	parameter x associated with system settling time
x_x	parameter x associated with a position
x_0	initial or specific value of parameter x
x_∞	abbreviation for $\lim_{t \rightarrow \infty} x(t)$
x^*	discrete-time sampled signal of a parameter x
O^{step}	optimization criterion based on the step response
O^{impulse}	optimization criterion based on the impulse response

List of Symbols

The following table summarizes the symbols that are used in this thesis. Their units are also given in the last column, where dashes (–) stand for dimensionless parameters and stars (*) marks ambiguous parameters units. The units for the rotational case are given in parentheses, if applicable.

Table 4: Symbols

symbol	description	unit
b	physical damping	Ns/m (Nms/rad)
B	virtual damping	Ns/m (Nms/rad)
c_i	substitution variable	–
C	cost function	–
d	delay factor	–
$\delta(\cdot)$	Dirac delta function	–
e	Euler's number	–

E	energy	Nm
F	force	N
$\mathcal{F}(\cdot)$	Fourier transform	*
g	slope of a function	–
$G_x(\cdot)$	closed-loop transfer function with output parameter x	*
$H_x(\cdot)$	open-loop transfer function with output parameter x	*
I	moment of inertia	kg·m ²
j	imaginary unit	–
k	physical stiffness	N/m (Nm/rad)
K	virtual stiffness	N/m (Nm/rad)
$l(\cdot)$	function of a line	–
m	mass	kg
$n(\cdot)$	polynomial in the numerator of a transfer function	*
O	optimization criterion	–
$p(\cdot)$	characteristic polynomial of a transfer function	*
r	radius of a concentric circle in the complex z -plane	–
\Re	real part of a complex argument	*
s	Laplace variable	1/s
t	time	s
t_d	time delay	s
t_r	effective time delay	s
T	sampling period	s
$u(\cdot)$	unit step function or Heaviside step function	–
w	weighting factor or exponent	–
x	position	m
z	Z-transform variable	–
\mathcal{Z}	Z-transform	*
α	normalized virtual stiffness	–
β	normalized virtual damping	–
γ	normalized physical stiffness	–
δ	normalized physical damping	–
ϵ	arbitrarily small positive quantity	*
ζ	system damping ratio	–
η	ratio of two parameters	–
Θ	joint angle	rad
κ	integer time index of discrete-time systems	–
ρ	relative error	–
τ	variable of integration representing time	s
τ	torque	Nm
χ	weighted position	N (Nm)
ω	angular frequency	rad/s
ω_N	Nyquist frequency	rad/s

Haptic rendering is the process of computing and generating forces in response to user interactions with virtual objects.

Salisbury et al. [100]

1

Introduction

The huge progress in the area of computer technology of the last decades enables nowadays visualizing complex virtual worlds photorealistically and in real-time. By using suitable human-machine interfaces, a user is able to look around in a virtual world and may even manipulate virtual objects. However, such interaction does not need to be limited to visual feedback only. A special kind of human-machine interfaces, called haptic devices, let users feel virtual worlds by their sense of touch.

Haptic perception comprises the sensation of pressure, vibration, and temperature at the skin (tactile perception), as well as the sensation of the location and movements of human joints, and applied muscle forces (proprioception or kinesthesia) [72]. Similarly, haptic devices can be roughly grouped into tactile devices that display information to human skin, and kinesthetic haptic devices that affect the position of human joints by applying forces (impedance-type haptic devices) or limiting human movements (admittance-type haptic devices). Displayed information of tactile devices can be perceived by tactile perception only, whereas the latter group excites both kinesthesia and tactile perception [101]. The focus of the present thesis is on impedance type kinesthetic devices, which represent the majority of the commercial kinesthetic haptic devices [86].

A haptic simulation is a virtual reality (VR) simulation in which a user is provided with artificial haptic feedback from a virtual environment in addition to ideally both visual and acoustic feedback. The process of computing and generating forces upon user interactions with the virtual environment is denoted as *haptic rendering* [100]. Figure 1.1 illustrates the typical interaction paths between user and virtual world for the visual and haptic sensory modality. In the upper part of this figure, the visual path is shown, in which a graphics rendering software computes images from a virtual

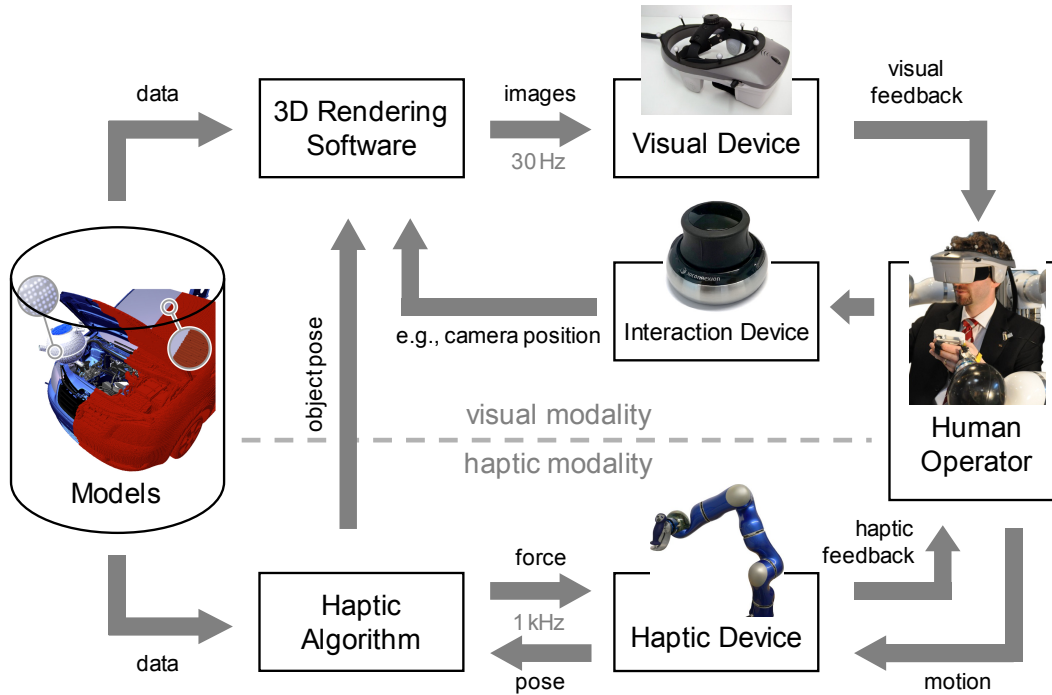


Figure 1.1: Scheme of user interaction with a virtual scene by visual and haptic means (adapted from [91]).

model. These images are displayed to the user by a visual device. The user can move the virtual camera and thus influence the view at the virtual scene through a separate sensory device, e.g., a tracking system or a 3D mouse. The lower part of Fig. 1.1 presents the haptic path. Similar to the visual path, this path also contains a software and a device: the haptic rendering algorithm computes haptic signals, while the haptic device generates the haptic feedback to the user from these signals.

Despite this similarity, however, there are two important differences between the two paths. Firstly, the update rate of the haptic path is more than an order of magnitude higher than for the visual modality. In detail, for the visual modality, an increase of the frame rate beyond 30 Hz does not significantly improve user performance in virtual environments [18], while for the haptic modality, a generally accepted convention is to provide update rates of at least 1 kHz [11]. And secondly, the signal flow between the elements of the haptic path is bidirectional, whereas this is not necessarily the case for the visual path, where the signal flow is often unidirectional. This implies that a haptic device is an interaction device that displays and measures at the same time data to and from the human operator. Moreover, it means that the three elements of human operator, haptic device, and haptic algorithm form a closed-loop system in which the haptic device links the other two elements.

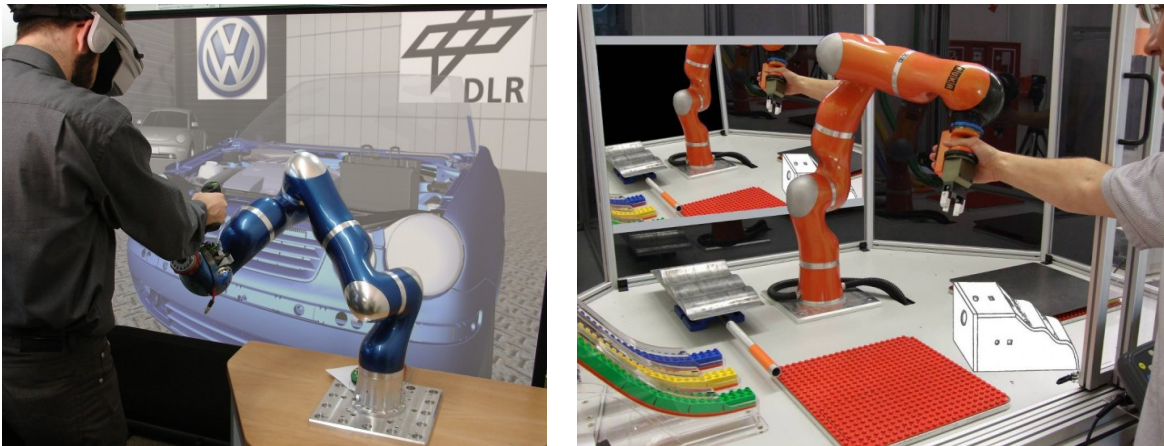


Figure 1.2: The research findings of this thesis contributed to improved haptic feedback in haptic assembly simulations [91] (left) and training [105, 59] (right).

1.1 Fields of Application

Haptic force feedback is used in applications in various domains, ranging from telerobotics, assembly simulations, ergonomics analysis, education and training, multimedia publishing, to computer games [43]. This large variety is not surprising considering that this kind of feedback brings great benefits to the user, which was confirmed in various evaluation studies. For instance, it could be shown that force feedback is beneficial in virtual assembly scenarios in terms of movement precision, mental workload, and spatial orientation [117]. Similarly, haptic feedback proved its advantageous impact during training tasks, as it has the potential to significantly accelerate skill acquisition in comparison to pure visual feedback [106]. Also during rehabilitation, it was shown that force feedback facilitates regaining motor function of stroke patients [113].

This thesis aims at optimizing the haptic feedback in haptic rendering applications using control engineering methods. The approach could already prove its practical benefit in the following two haptic rendering applications (see also Fig. 1.2):

Haptic assembly simulations have the goal of reducing the need for prototyping and thus of accelerating the development process of complex mechanical systems, such as cars, planes, or satellites [53, 91, 94]. They provide a design engineer the opportunity to detect possible construction errors and complicated assembly tasks in the CAD (computer-aided design) model in an early development stage, before a hardware prototype is built. As a result, they are an effective means for cost savings in such development processes.

Haptically supported training has the aim of accelerating skill acquisition compared to pure visual training or textbook learning. Two different training applications benefit from the research findings, i.e., training of robot programmers [57, 59, 104, 105] and of astronauts [94, 95].

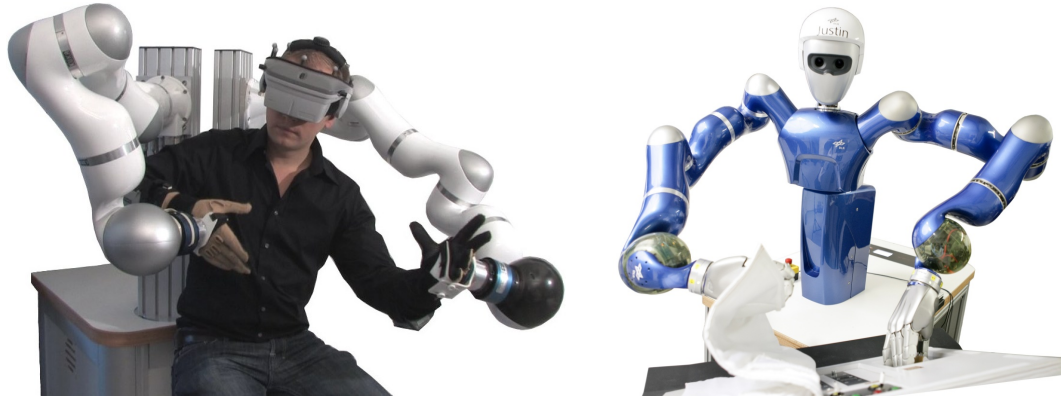


Figure 1.3: In the course of applying the research findings to haptic rendering applications, the bimanual haptic device HUG was developed [51] (left). It is also used as the haptic master station for telemanipulating the humanoid robot SpaceJustin [94] (right).

1.2 Technological Developments

In the course of investigating these haptic rendering applications, the bimanual haptic interaction device HUG [58, 51] was developed (see Fig. 1.3, left). It consists of two DLR/KUKA light-weight robots as main elements [46]. These robots were designed for physical human-robot interaction and thus have specific properties due to which they can be also used as kinesthetic haptic devices. In particular, they have a workspace similar to the human arm and are commanded at an update rate of 1 kHz. Most importantly, however, they are equipped with torque and position sensors in each of their seven joints that enable both impedance or admittance controlled operation.

A couple of technologies was developed to advance the usability of HUG as haptic device. An interactive virtual reality robot viewer intuitively visualizes robot parameters and thus contributes to a safer and more comfortable usage of the robotic system [52]. A vibro-tactile feedback device provides supplementary feedback to the human arm in order to display contacts between arm and virtual environment [102, 118]. And finally, for computing the haptic signals for these applications, a computationally efficient haptic algorithm was implemented that is able to provide the challenging haptic update rate of 1 kHz [96, 97, 98, 120].

Clearly, the technologies developed may also be used in other fields than haptic rendering. Most prominently, HUG is also used as haptic device for telemanipulating the humanoid robot SpaceJustin (see Fig. 1.3, right). However, despite its high relation to haptic rendering and the other promising applications of telerobotics, the focus of the present thesis is on the control of haptic rendering as it will be detailed in the following.

1.3 Motivation and Problem Definition

One of the most important preconditions for haptic interaction is to guarantee stability during operation. Unstable behavior may result in uncontrollable, highly dynamic movements of the haptic device, which make it impossible to realistically render forces from a virtual reality simulation. As a haptic device is a mechanical system that can apply forces to a human operator, such unstable movements also pose a risk of physical harm to the human operator. Hence, stability of a haptic system is crucial not only for enabling high quality haptic feedback, but rather also for safety.

There are plenty of sources for instability in haptic rendering that originate from the haptic system composed of the haptic device, the haptic algorithm, and the human arm. These sources include dynamics and compliance of the involved haptic device [30], velocity filtering in the device controller [21], discrete-time control of the haptic device [81], non-colocation of sensors and actuators [22, 41], and nonlinear effects such as value-discretization [4, 33], saturation, backlash, and hysteresis phenomena of the haptic device [44]. Most importantly, however, stability is compromised by time delay that is caused by communication and computation of haptic data [38].

Although much research has been conducted on how these factors affect the stability of a haptic system, there is still a clear gap of knowledge on the interplay of the parameters. Similarly, the research in the field of haptic rendering has mainly concentrated on stability, or on passivity as a tool for achieving stability. However, it is evident that stability alone is not enough to create realistic haptic feedback. A haptic system that is stable may nevertheless exhibit slow transient behavior which may destroy the haptic impression of virtual touch. Instead, a haptic device should ideally comply with conditions of optimal control in addition to stability in order to get the most out of a haptic simulation.

1.4 Key Contributions and Thesis Structure

The goal of the present thesis is to investigate the issues of stability and optimal control of haptic rendering as well as to unveil the influence of the different system parameters on the performance of a haptic system. Amongst the most important questions that will be answered in the context of this work are:

1. For which parameter values is a haptic system stable and what are the stability boundaries?
2. What is the influence of the human operator on stability?
3. How is the relation between stability and passivity in the parameter space?
4. Which parameter values result in optimal system behavior with respect to settling time, overshoot, and energy dissipation?
5. How does time delay influence stability, passivity, and optimal system behavior?

The results of this thesis are not only important for setting the parameters of haptic rendering, and hence for contributing to the success of haptic simulations, but rather are also valuable for the design of new haptic devices and may be taken as a theoretical basis for future psychophysical studies. The remainder of the thesis is structured as follows.

Chapter 2 presents a literature review on haptic control theory with the goal of identifying the gaps in the present state of research. To this end, various theoretical approaches are compared and differences in the considered models and the physical effects are highlighted. In this context, this chapter also clearly shows the contribution of the present thesis.

Chapter 3 conducts a stability analysis of a haptic system resulting in stability boundaries that define the stable parameter regions. This approach has three notable features that differentiate it from existing work. Firstly, it exactly takes into account the effects of discrete-time sampling and time delay by modeling the haptic system as hybrid (mixed continuous- and discrete-time) system. Secondly, it investigates the influence of the human operator on stability. And thirdly, it introduces normalization rules that lead to dimensionless parameters, which drastically simplify the theoretical investigations and enable a clear presentation of the results.

Chapter 4 conducts a passivity analysis that yields passivity boundaries of a time-invariant haptic system. It enhances the current state of research as it takes into account time-delay as a system parameter. Similar to the stability analysis, the passivity analysis leads to a different set of normalization rules that result in dimensionless parameters. By comparing the passivity and stability regions, this chapter quantifies the conservativeness of passivity with respect to stability and identifies the cause for this large discrepancy.

Chapter 5 investigates the optimal performance of haptic systems. It makes use of various optimization criteria from standard control theory textbooks that are either based on the poles of the transfer function or on the transient response of the haptic system and applies them to the haptic system. For each criterion, a dimensionless cost function is defined which results in a cost distribution map inside the stable parameter region. Moreover, optimal paths and optimal points inside the cost maps are determined. By investigating the influence of delay on these optimal points, this chapter derives a polynomial cost approximation function that may be used to predict the optimal performance of haptic systems.

Chapter 6 performs experimental studies on two different devices that validate the theoretical results. They also investigate the influence of the human grip strength and time delay on stability and costs. To this end, the experimental stability boundaries and cost distribution maps are compared to their theoretical counterparts. These results confirm the theoretical approach with regard to predicting the optimal performance, but also show the limitations of the approach.

Chapter 7 summarizes the main results and discusses their expected impact. It also identifies promising directions of future research.

In recent times, the importance of the sense of touch for human-computer interaction has finally been realised and it is widely believed that haptic interfaces will be a major improvement for human-system interaction. The rapid increase of research activities in this field during the past decade supports this expectation.

Bicci et al. [12]

2

Control Approaches for Haptic Rendering

The control of kinesthetic haptic devices is highly related to the field of robot control. This is because a haptic device itself may be considered as a small robot. There are, however, some basic control aspects that are different and of particular relevance for haptic interaction. For instance, a great challenge in analyzing stability of haptic systems is taking into account the influence of the human operator. Not only the diversity of human arm characteristics, but also the various possibilities of grasping haptic devices make it difficult to determine a valid model of the human arm. Another major difference concerns time-discretization and delay, which both are frequently neglected in robot control, but which clearly impair the performance of a haptic device. Similarly, some other factors including position quantization and static friction are in focus of haptic control and only play a minor role in robotics.

The research area of control for haptic rendering has been gaining increasing attention in recent years. This is due to the huge progress in the computer technology and also due to the increasing number of available kinesthetic haptic devices. Existing control approaches may be roughly grouped into stability- and passivity-based analyses. This chapter carefully reviews the literature in order to identify the major gaps in the present state of research and to clarify the contribution of this thesis. It is structured as follows: the first two sections review the control approaches based on stability and on passivity, respectively. On this basis, the most considerable approaches are assessed in a comparative table and the main contribution of the present thesis is highlighted in terms of modeled system properties and of applied analysis methods.

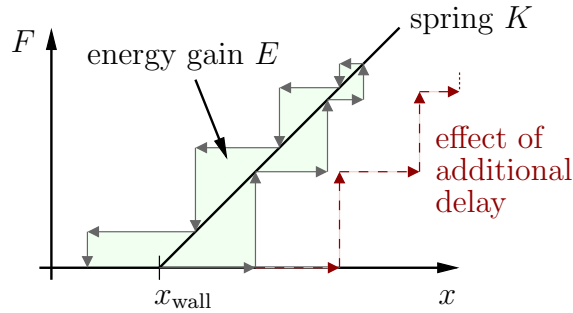


Figure 2.1: The force during a collision with a virtual wall represented by a discrete-time spring with stiffness K . Due to discrete-time sampling, the force curve takes the form of a stairs function and causes an *energy gain* E . The amount of energy generated corresponds to the green shaded area that is surrounded by the force curve. The dashed red curve exemplarily shows the effect of an additional time delay of one sampling period, which causes the amount of energy to increase drastically.

2.1 Stability-based Approaches

Stability is a necessary precondition to enable secure and efficient operation. Most literature on haptic control tackles the topic of stability by modeling the haptic system and analytically analyzing its transfer function. These analyses investigate various sources for instability as already discussed in the introductory chapter of this thesis.

The most frequently mentioned and investigated source is the time-discretization of virtual environments. The mechanisms in case of a spring-like environment are well understood. For a virtual environment with a force characteristics of an ideal spring, the resulting force F can be expressed as the product of virtual stiffness K and penetration depth Δx ,

$$F = K \Delta x. \quad (2.1)$$

The force curve of a collision with such a virtual wall, i.e., when compressing and decompressing the discrete-time spring is illustrated in Fig. 2.1. The force is only updated at the sampling instants and keeps constant between them. As energy is the integral of force over distance, the green shaded area that is enclosed by the force curve corresponds to the amount of energy that is generated by a collision with a discrete-time spring. This energy, which is also denoted as *energy gain* [11] or *energy leak* [38], may cause a haptic system to become unstable if it exceeds the amount of energy dissipated by the inherent friction of the haptic device and the human operator. The energy gain increases with higher stiffness of the wall, greater initial impact velocity, faster collision dynamics, and above all, additional time delay (see dashed curve in Fig. 2.1).

The classical approach to overcome this problem is to introduce a virtual damper B that dissipates enough energy to restore stability. The force of such a spring-damper system is

$$F = K \Delta x + B \Delta \dot{x}, \quad (2.2)$$

where $\Delta \dot{x}$ is the velocity of the haptic device with respect to the virtual wall. In terms of control theory, this system is a discrete-time PD-controller, respectively a PI-controller if the velocity is taken as control variable. In comparison to an ideal continuous-time damper that dissipates more energy for greater damping factors, its discrete-time counterpart has an upper limit with regard to stability. Above that limit, a discrete-time damper introduces itself unstable oscillations to a haptic system [99].

One of the first studies that investigated the stability of haptic rendering was conducted by Minsky et al. [81]. They performed two analyses: an analytical continuous-time analysis that approximates the discrete-time effects by a delay, and a numerical simulation of a hybrid haptic system, which contains continuous-time and discrete-time elements. This pioneering work represents a cornerstone in the control of haptic systems and motivated further extensive research from other researchers.

Salcudean and Vlaar [99] determined the analytical solution for the hybrid haptic system. They considered a haptic device modeled as simple mass that is controlled by a discrete-time PD-controller including a delay of one sampling period. However, they did not take into account a human operator. This extension was done later by Gil et al. [35], who investigated the influence of the human operator on stability by considering various human models that have been previously used in literature. On this basis, the same research group investigated the effect of vibration modes originated in structural elasticities of the haptic device [20, 30]. They found a possible negative influence of such vibration modes on the stability of a haptic device.

A common approach to counteract the stability problem of stiff contacts, is to introduce an artificial coupling between the haptic device and the virtual environment: the so-called *virtual coupling* proposed by Colgate et al. [25]. The idea is to separate the control task from the virtual environment by adding a coupling element in the form of a spatial spring-damper system. As consequence, the stiffness exhibited by the haptic device does never exceed those of the virtual coupling element, even if the virtual environment is much stiffer. A drawback of the virtual coupling approach is, however, that it affects the realism of a haptic simulation as it distorts the forces from the virtual environment. Nevertheless, virtual coupling is commonly used in haptic rendering for the *god-object method* [87, 125]. It separates the actual position of the haptic device from the visualized object, the so-called *virtual proxy* [92], in order to avoid visible penetration in the virtual scene. Adams and Hannaford [7] formulated the virtual coupling approach as two-port network and analyzed its stability and system performance.

Recently, Paine et al. [90] enhanced the stability approach towards optimal control. Optimal control methods make it possible to determine virtual parameters with which the haptic system behaves optimal with regard to a certain performance criterion. These authors optimized the performance of their system with regard to a phase margin criterion. Their work is presumably one of the first contributions that directly tackles the optimal performance of a haptic system. It was developed in parallel to this thesis although some of the research results on optimal control presented in Chapter 5 of this thesis were published in [50] more than one year before the article of Paine et al. [90] appeared.

In comparison to haptic rendering, optimal control is already a topic of interest in the related field of telerobotics since a couple of decades. It was headed by the work of Lawrence [70] on optimal transparent coupling between master and slave. For haptic rendering, however, the research focus is only gradually shifting towards optimal control.

2.2 Passivity-based Approaches

A second group of control approaches for haptic rendering focuses on passivity (for the definition of passivity used in this thesis, the reader is referred to Chapter 4). These approaches utilize the objective fact that a human can always interact in a stable manner with a passive device [33]. This human capability is convincingly supported by experiments from Hogan [47], which show that a human operator even behaves like a passive object in the frequency range of interest for haptic rendering. Moreover, passivity has the appealing property that certain interconnections of passive systems results in a passive and therefore stable¹ overall system [68], [108]. The main advantage resulting from these favorable properties of passivity is that the human operator does not need to be considered in the analysis, provided that haptic device and the virtual environment are passive.

Colgate and Schenkel [23, 24] deployed the passivity concept for haptic rendering. They derived a fundamental passivity condition for a time-invariant haptic device and virtual environment. The haptic device was modeled as a damped mass and the virtual environment as a stable linear, time-invariant transfer function. Based on this general passivity condition, they obtained a specific linear passivity condition that applies for a virtual wall modeled as discrete-time spring-damper system,

$$b > \frac{KT}{2} + |B| , \quad (2.3)$$

with continuous-time viscous damping b of the haptic device, discrete-time stiffness K and damping B of the virtual wall, and sampling period T . It states that the two virtual wall parameters are limited by the continuous-time damping b .

¹To be rigorous, the system must be strictly output passive to obtain bounded input-bounded output (BIBO) stability [3].

In terms of stability, however, Colgate and Schenkel found much higher stiffness values to be stable than admitted by this passivity condition, which means that the passivity condition is highly conservative with respect to stability. Despite of this, the work of Colgate and Schenkel inspires a bunch of research studies that aim at enhancing their passivity-based approach.

Miller et al. [80] have extended the analysis to virtual coupling and nonlinear virtual environments, and thereby relaxed the requirement of passivity. Stramigioli et al. [114] applied the port-Hamiltonian approach to haptic systems in order to connect continuous- and discrete-time elements in a passive manner. Abbott and Okamura [4] included static friction and position quantization in their system model and analyzed the influence of these nonlinearities on passivity. Their analysis revealed two restrictive conditions for the wall stiffness, one constituted by linear and the other by nonlinear effects. Both conditions must simultaneously hold to obtain passivity. This result is supported and enhanced by more comprehensive analyses of Diolaiti et al. [33] with regard to time delay, and of Iskakov et al. [60] in terms of discrete-time damping. Their research clearly shows that the destabilizing nonlinear effect of sensor resolution can be compensated by the two other nonlinearities of static friction and dead-zone, whereas the other passivity condition constituted by the linear effects remains unaffected. Or, to put it more clearly, the linear and nonlinear effects of the considered system may be investigated separately in terms of passivity.

A different class of passivity-based approaches considers time-variant controllers, i.e., controllers that may change during the haptic simulation. Compared to the above passivity analyses of time-invariant systems, the class of time-variant controllers may lead to less conservative behavior with regard to stability and hence to higher system performance. However, time-variant control comes at the cost of a more challenging analysis because the Laplace and Z-transforms cannot be applied to such systems [112].

The *time-domain passivity controller* introduced by Hannaford and Ryu [42] is the most relevant representative of such time-variant method in the field of haptic rendering. This controller observes the mechanical power transmission between haptic device and human operator. It adjusts a variable damping factor accordingly to prevent excess energy from being generated by the haptic device while rendering a virtual environment. Several enhancements of the time-domain passivity controller were suggested by different research groups with respect to various aspects, e.g., in [39, 45, 89, 93]. In theory, the controller guarantees the passivity of a haptic system and prevents it from getting unstable. The practical use of this approach, however, reveals some limitations due to imprecise energy observation and bounded energy dissipation rates [93]. Another drawback is that it dissipates the energy only after it has been detected and thus distorts the feedback from the haptic simulation. To preserve the realism of the simulation, it is more favorable to ensure in advance that a haptic interaction will not get unstable. In that case, the time-domain passivity controller may serve as an additional safety mechanism that comes into effect in case of an incident.

2.3 Discussion

This chapter reviewed the state of research in the control of haptic rendering and summarized the key publications in this domain. Existing concepts may be roughly grouped into stability- and passivity-based approaches. While most passivity-based approaches are overly conservative, the stability ones lack realistic models as they either neglect the effect of the human operator or of other system properties such as time delay.

Table 2.1 depicts this situation. This comparative table chronologically lists the most relevant approaches labeled by the first author and the publication year. It summarizes the linear and nonlinear properties that are taken into account by these approaches. Although all approaches investigate slightly different models of the haptic system, these models minimally consist of a mass and a discrete-time spring. The only exception is the time-domain passivity controller of Hannaford and Ryu [42] that achieves passivity without any model assumptions on the haptic device.

This comparative presentation of the state of research reveals four important deficiencies in the control of haptic systems:

1. Time delay in combination with a discrete-time spring-damper system has not been analytically investigated so far.
2. Optimal control was not in the focus of research for many years, and has only gained attention very recently.
3. The insights on the influence of the human operator on stability are limited.
4. There are some system properties that have only been marginally analyzed, e.g., velocity filtering and structural elasticities of the haptic device.

This thesis tackles the first three of these lacks in the current state of research. Thus, its main contribution in terms of modeled system properties is that it analyzes the influence of the human operator on a haptic system performance and that it investigates the effect of delay and time-discretization. In terms of analysis methods, it conducts a stability and a passivity analysis and deploys means of optimal control on the field of haptic rendering.

Table 2.1: Key approaches in control of haptic rendering.

timeline	1990	1994	1996	2000	2002	2003	2005	2006	2007	2008	2015	2014
first author	Minsky	Colgate	Salcudean	Miller	Hannaford	Gil	Abbott	Diolaiti	Iskakov	Diaz	Paine	Hulin
reference	[81]	[23]	[99]	[80]	[42]	[35]	[4]	[33]	[60]	[30]	[90]	[48, 50]
analysis												
stability	+	-	+	-	-	+	-	+	+	+	+	+
passivity	-	+	-	+	+	-	+	+	-	-	+	+
optimal control	-	-	-	-	-	-	-	-	-	-	+	+
linear properties												
m mass	+	+	+	+	-	+	+	+	+	+	+	+
K discrete-time stiffness	\pm^a	+	+	+	\pm^b	+	+	+	+	+	\pm^a	+
B discrete-time damping	\pm^a	+	+	+	+	+	-	-	+	-	\pm^a	+
b viscous friction	+	+	-	+	-	+	+	+	+	+	+	+
human operator	+	\pm^c	-	\pm^c	\pm^c	+	\pm^c	-	-	-	-	+
d delay	+	-	\pm^d	\pm^d	\pm^d	-	-	+	-	-	+	+
velocity filtering	-	+	-	-	-	-	-	-	-	-	+	-
structural elasticities	-	-	-	-	-	-	-	-	-	+	-	-
nonlinear properties												
unilateral wall	-	+	-	+	-	-	+	-	-	-	-	\pm^e
c static friction	-	-	+	-	-	-	+	+	+	-	-	-
Δ pos. sensor quantization	-	-	-	-	-	-	+	+	+	-	-	-

^aThe effect of time-discretization was only considered within numerical simulations.

^bThe time-domain passivity approach does not require any assumption on the virtual environment but it takes into account the effect of time-discretization, as it assumes a constant force between two sampling instants.

^cThe passivity analysis is independent of a human operator grasping the haptic device. Thus, although not investigated directly, this work takes into account humans operators.

^dA constant delay of up to one sampling period was considered.

^eThe unilateral wall is taken into account for passivity and not for stability.

The most important characteristic of the dynamic behavior of a control system is absolute stability—that is, whether the system is stable or unstable.

Ogata [85]

3

Stability Analysis

This chapter performs a linear stability analysis of the haptic system shown in Fig. 3.1 mainly following my previous work in [36], [48], [55], and [56]. This analysis for the first time takes into account the influence of time delay, device damping, and of a human operator on stability. It considers realistic parameter ranges for the human operator and the haptic device. A peculiarity of the presented approach is the exact combination of discrete- and continuous-time elements, which reveals fundamental parameter dependencies for stability. Without loss of generality, the calculations are performed for translational movements. They also hold for rotations.

At first, Sect. 3.1 describes the considered system and assumptions. Based on this system description, Sect. 3.2 derives the closed-loop transfer function. After investigating in Sect. 3.3 the possible ranges for the involved system parameters, Sect. 3.4 introduces the stability boundaries of the investigated system. In Sect. 3.5 these boundaries are linearized around the point of origin. Sect. 3.6 introduces parameter dependencies for stability and concludes this chapter.

3.1 System Description

The analyzed system consists of a human operator holding an impedance type haptic device, which is interacting with a delayed virtual environment (see Fig. 3.1). Following assumptions will be made on these system components.

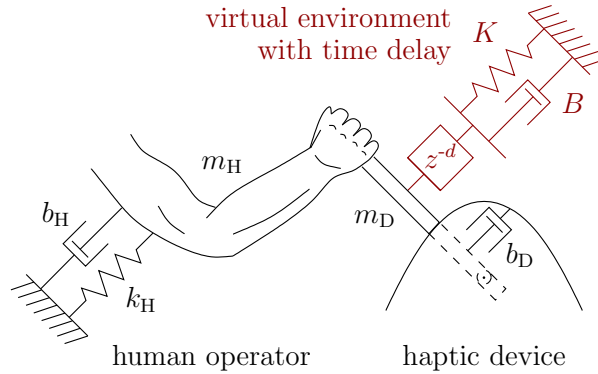


Figure 3.1: Simplified model of a human arm interacting with a 1 degree of freedom haptic device [48].

3.1.1 Haptic Device

The haptic device is a single degree of freedom (DoF) mass m_D , which is damped by a viscous damper b_D . It has constant sampling rate and constant time delay. Nonlinear effects like static friction, or quantization and saturation of sensors and actuators are not taken into account. Also the dynamics of the device actuators are neglected, such that a force F will be assumed to be applied constantly over one sampling period T . Furthermore, the device structure is assumed to be of high stiffness, such that structural compliance can be neglected.

3.1.2 Virtual Environment

For the virtual environment, the common implementation as discrete-time spring-damper system (discrete-time PD-controller) is considered, with stiffness K and damping B . Therefore, the transfer function of the virtual environment from position to force is

$$H_F(z) = K + B \frac{z-1}{Tz}, \quad (3.1)$$

with sampling time $T > 0$. In this chapter the unilateral constraint of virtual walls is not considered for stability.

3.1.3 Time Delay

Considering the effect of time delay is crucial for the validity of any stability analysis on haptic interaction. This is, because each real haptic system is affected by time delay t_d , which may originate from different sources, including communication, force computation, or motor control. Due to the typically fast sampling rate of 1 kHz of haptic systems [11], a delay of only a few milliseconds means already a delay of several sampling steps T . Although a well-accepted design goal is keeping involved delays as

short as possible, a few real haptic systems are affected by delays of clearly more than one sampling step, e.g., 5 ms [50].

Time delays in a closed control loop can be summarized without affecting the characteristic polynomial of a linear system. Therefore, without loss of generality, the round-trip delay t_d is considered as the sum of all delays involved in the closed-loop of the haptic device and the virtual world. This combined time delay is assumed to be constant and positive $t_d \geq 0$. It has a transfer function of $e^{-t_d s}$, or in the discrete-time domain z^{-d} , where d is the delay factor defined by $d = t_d/T$.

In comparison to standard discrete-time control theory, in which delay is defined as an integer multiple of the sampling period T , the calculations in this thesis admit rational numbers for the delay factor $d \in \mathbb{Q}_{\geq 0}$. Rational delay factors typically occur in haptic systems with asynchronous read and write operations, or with delays in the motor controller. This extended definition is possible, since any discrete-time transfer function with rational delay factor can be transferred into a transfer function with a whole number for the delay factor by appropriately substituting the discrete-time variable z . Note that this approximation for rational delay factors considers discrete-time systems with multiples of the original sampling rate.

3.1.4 Human Arm

The used model of the human arm is a single DoF mass-spring-damper system, with mass m_H , stiffness k_H , and viscous damping b_H . This linear and time-invariant model of the real human has already been applied in many theoretical studies (see [35]). One reason therefore is obviously that it can be quite easily employed when analyzing stability of haptic systems. But more importantly, its validity could be supported by various experimental studies, e.g. [84]. It holds for small arm movements and time periods shorter than the time needed for humans to actively change their arm parameters. Hogan [47] found that for periods up to 1.2 seconds these parameters appear not to change. On the other hand, it is known that other factors such as reflexes can limit the validity of this model, as they take effect much faster than intended human movements [111].

Many different parameter values for the second-order arm model exist in literature [35]. This diversity originates from the different directions of movements considered, the posture of the user, as well as the individual's physical properties. Therefore, for the stability analysis in this chapter, only limits for the parameter ranges of the fractions k_H/m_H and b_H/m_H will be assumed, and not specific values of the three parameters. These limits will be introduced in Sect. 3.2.

It is further assumed that the human operator holds the haptic device in such a way that the human arm mass m_H is directly coupled to the device inertia m_D . Therefore, the physical parameters of the haptic device and the human can be combined to

$$m = m_D + m_H \quad b = b_D + b_H \quad k = k_H, \quad (3.2)$$

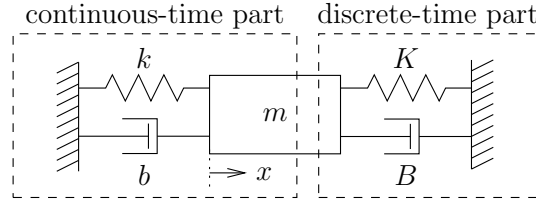


Figure 3.2: Physical equivalent of the addressed system [48].

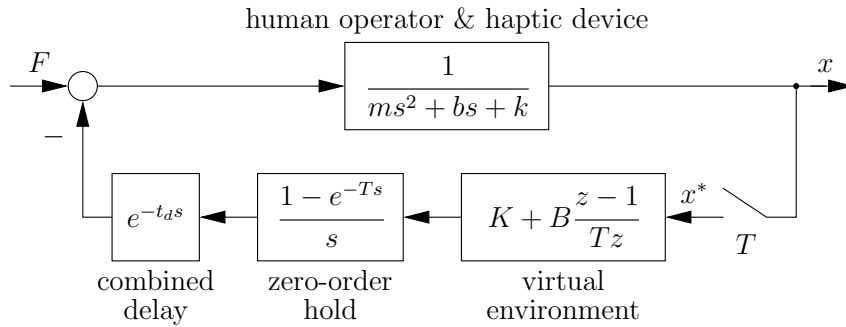


Figure 3.3: Control loop of the haptic system [48].

where m , b , and k are the effective physical mass, damping, and stiffness, respectively. The transfer function of this continuous-time mass-spring-damper is

$$H_x(s) = \frac{1}{ms^2 + bs + k}. \quad (3.3)$$

Figure 3.2 shows the physical equivalent of the addressed haptic system.

3.1.5 Control Loop

Given these assumptions, the control loop shown in Fig. 3.3 can be set up. It is a hybrid system that contains both continuous-time (time delay and physical mass-spring-damper system) and discrete-time (virtual environment) elements. The zero-order hold element has a transfer function of

$$H_0(s) = \frac{1 - e^{-Ts}}{s}. \quad (3.4)$$

The input F is an external force, representing the intended force of the human operator. The following calculations assume this force being constant during a sampling period T , which may be considered as valid assumption because the typical sampling rate of 1 kHz is much faster than the intended movements of a human [14]. Collisions of the haptic device with its real environment (e.g., the table on which the haptic device is located) are neglected as they do not occur in normal use.

3.2 Closed-Loop Transfer Function

This section derives the closed-loop transfer function of the investigated hybrid system shown in Fig. 3.3. As this linear system is a mixed discrete- and continuous-time system, first all blocks of the control loop have to be transformed into a common time domain before performing a stability analysis. The discrete-time domain is chosen because calculating the exact discrete-time transfer function of the given system is straightforward [55, 110]. Then normalized parameters will be introduced, which allows writing the resulting formulas in a significantly simpler form. Finally, the closed-loop transfer function will be derived given in these normalized parameters.

3.2.1 Discrete-Time Equivalent

The continuous-time elements of the control loop in Fig. 3.3 are delay, zero-order hold, and the mass-spring-damper system representing the human holding a haptic device. Due to the time-shift property of the Z-transform [2, 75], the delay may be handled separately when calculating the discrete-time equivalent. It holds that $e^{-dT_s} = z^{-d}$. The exact zero-order hold equivalent of the mass-spring-damper system without delay can be determined by some calculations (see Appendix A.2), while assuming the input force F only changes at the sampling instants and is constant otherwise,

$$\mathcal{Z} \{H_x(s)H_0(s)\} = \frac{2(z + e^{-bT/m}) - (z + 1)(c_2 + c_3) + bT(z - 1)(c_2 - c_3)/(mc_1)}{2k(z^2 - (c_2 + c_3)z + e^{-bT/m})} \quad (3.5)$$

with

$$\begin{aligned} c_1 &= \sqrt{(bT/m)^2 - 4kT^2/m} \\ c_2 &= e^{-(bT/m+c_1)/2} \\ c_3 &= e^{-(bT/m-c_1)/2} \end{aligned} \quad (3.6)$$

The discrete-time system with these equivalents has the exact same behavior at the sampling instants as the original system in Fig. 3.3. Note that if $b^2 < 4km$, the substitution parameters c_1 , c_2 , and c_3 become complex numbers. However, the coefficients of transfer function (3.5) are always real numbers independent of the parameters c_i being complex or not.

3.2.2 Normalized Characteristic Polynomial

Some of the parameters in discrete-time equivalent (3.5) can be grouped, such that a suited parameter substitution can simplify that formula. Salcudean and Vlaar [99] introduced such substitution for a mechanically undamped haptic device without human operator. Their substitution utilizes the linear relation of the sampling time T and the mass m on the transfer function, and resulted in a simpler equation with two parameters less.

Table 3.1: Normalization rules and the resulting dimensionless parameters as defined in [56].

parameter name	symbol	dimensionless variable
sampling period	T	—
mass	m	—
delay	t_d	$d := t_d / T$
virtual stiffness	K	$\alpha := KT^2 / m$
virtual damping	B	$\beta := BT / m$
physical stiffness	k	$\gamma := kT^2 / m$
physical damping	b	$\delta := bT / m$

For the more complex system investigated in this chapter, it is possible to extend their definition of normalized parameters replacing all physical parameters by their dimensionless counterparts [56]. Such substitution rules are summarized in Table 3.1 and transform the transfer function (3.5) into

$$\mathcal{Z} \{H_x(s)H_0(s)\} = \frac{T^2}{2m} \frac{2(z + e^{-\delta}) - (z + 1)(c_2 + c_3) + \delta(z - 1)(c_2 - c_3)/c_1}{\gamma(z^2 - (c_2 + c_3)z + e^{-\delta})} \quad (3.7)$$

with

$$\begin{aligned} c_1 &= \sqrt{\delta^2 - 4\gamma} \\ c_2 &= e^{-(\delta+c_1)/2} \\ c_3 &= e^{-(\delta-c_1)/2}. \end{aligned} \quad (3.8)$$

As now all elements of the investigated system in Fig. 3.3 are present in the discrete-time domain, its closed-loop transfer function can be set up easily. This transfer function from force F^* to position x^* results in

$$G_x(z) = \frac{T^2 z^{1+d}}{m} \frac{n(z)}{p(z)} \quad (3.9)$$

with

$$\begin{aligned} n(z) &= ((c_2 + c_3 - 2)c_1 - (c_2 - c_3)\delta)z \\ &+ (c_2 + c_3 - 2e^{-\delta})c_1 + (c_2 - c_3)\delta \end{aligned} \quad (3.10)$$

and

$$\begin{aligned} p(z) &= ((c_3 + c_2 - 2)c_1 + (c_3 - c_2)\delta)(\alpha + \beta)z^2 \\ &+ \left(((c_3 + c_2 - 2e^{-\delta})c_1 + (c_2 - c_3)\delta)\alpha \right. \\ &\quad \left. + 2((1 - e^{-\delta})c_1 + (c_2 - c_3)\delta)\beta \right)z \\ &- 2(z^2 - z(c_3 + c_2) + e^{-\delta})c_1\gamma z^{1+d} \\ &+ ((2e^{-\delta} - c_3 - c_2)c_1 + (c_3 - c_2)\delta)\beta, \end{aligned} \quad (3.11)$$

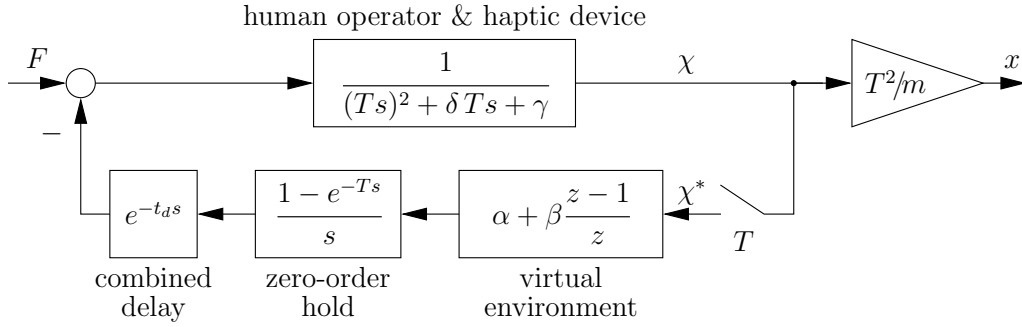


Figure 3.4: Control loop equivalent to Fig. 3.3 expressed by normalized parameters.

where the force F^* and the position x^* are the discrete-time counterparts of the continuous-time signals F and x . It is important to note that the normalized characteristic polynomial $p(z)$ depends only on the five dimensionless parameters α , β , γ , δ and d . The dependency of the mass m and the sampling time T is only implicit. Therefore, the parameter substitution transforms the original seven parameters system into a system with only five explicit parameters, which will drastically simplify the following stability analysis.

On the other hand, the complete transfer function $G_x(z)$ in (3.9) is scaled by the two parameters m and T . This relation is clearly illustrated in the normalized control loop in Fig. 3.4, where

$$\chi(t) := m/T^2 x(t). \quad (3.12)$$

is a scaled position and has the same unit of measurement as the input force F . This scaled position will be employed in Chapter 5 to draw transient responses independent of mass m and sampling period T . Similar to the normalized characteristic polynomial, the scaled transient responses only depend implicitly on these two parameters.

3.3 Parameter Range

The physical parameters involved in the system can strongly vary depending on the grasp of a human holding the haptic device. The range comprises from not holding the haptic device to holding it with full stiffness. Moreover, the physical parameters also highly depend on the direction of movement analyzed, as well as on the type of haptic device used. This section determines realistic ranges for the two normalized physical parameters γ and δ , similar to [56]. To this end, the definitions of these two parameters are recalled first,

$$\begin{aligned} \gamma &= T^2 k_H / (m_D + m_H) \\ \delta &= T (b_D + b_H) / (m_D + m_H). \end{aligned} \quad (3.13)$$

Table 3.2: Possible parameter values of a human arm (extension of [35]).

author(s)	m_H/kg	$k_H/\text{N/m}$	$b_H/\text{Ns/m}$
Daniel et al. [29] ^a	1	39.5	12.6
Hogan [47]	0.8	568	5.5
Kazerooni et al. [62]	4.54	12.5	6.83
Kosuge et al. [66]	1.95	55	2.46
Kuchenbecker et al. [67]	0.15	1000	7.5
Lakatos et al. [69]	2.79	345	33.8
Lawrence [70]	17.51	175.1	175.1
Lawrence and Chapel [71]	0.5	40	6
Lee et al. [73]	0.15	7	0.5
Tsuji et al. [116]	1.8	199.1	26.2
Yokokohji et al. [123]	2.0	10.0	2.0

^aThis article considers a combined system of a human arm and a haptic device.

Assuming positive masses and dampers, these definitions can be used to derive the following two inequalities,

$$\begin{aligned}\gamma &< T^2 k_H/m_H \\ \delta &< T (b_D/m_D + b_H/m_H).\end{aligned}\tag{3.14}$$

Therefore, it is sufficient to determine independent upper limits for the human and the haptic device, to obtain conservative upper limits for γ and δ . Table 3.2 lists several values for mass, stiffness, and damping of human arms that were used in literature, comprising various grasps and different directions of movement. Figure 3.5 shows the location of the fractions k_H/m_H and b_H/m_H for the values listed in that table. It appears that the fractions of Kuchenbecker et al. [67] are much higher compared to all the others, which is mainly due to two reasons.

First, in that study the arm was fixated by a strap, such that only the joint stiffness of the hand was measured. In contrast, the human arm stiffness results as series connection of many joint stiffnesses, and is therefore much smaller. Second, the human hand has better ratios of stiffness to mass, and damping to mass than the human arm because its actuators (muscles) are located in the lower arm and therefore do not contribute to the hand mass. Due to these two reasons, these value pairs will be excluded when determining the parameter ranges.

For all the other values, the following limits hold,

$$\begin{aligned}k_H/m_H &\leq 710 \text{ s}^{-2} \\ b_H/m_H &\leq 14.6 \text{ s}^{-1},\end{aligned}\tag{3.15}$$

where s means seconds, and should not be mixed up with the Laplace variable s .

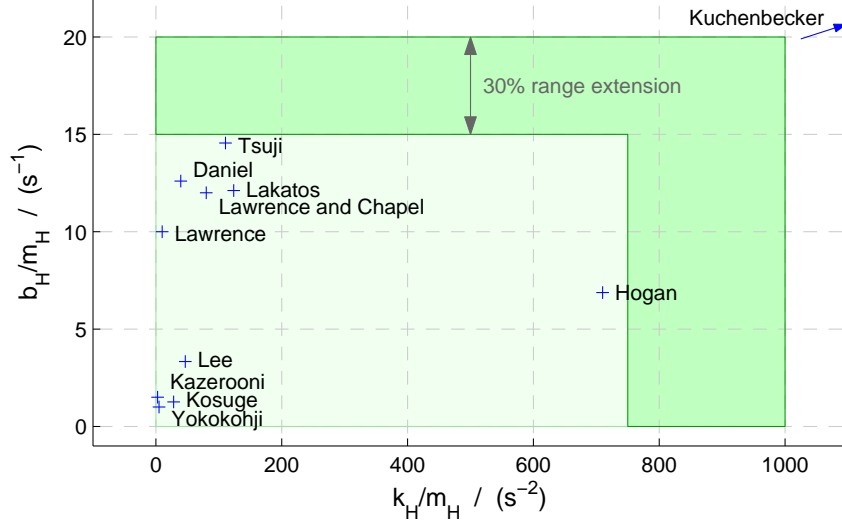


Figure 3.5: Parameter values of the human arm of Table 3.2 normalized by the mass m_H . The parameter range considered in this thesis for the stability analysis is extended by 30%.

Normally, haptic devices are designed to exhibit very low physical damping, such that optimal haptic transparency (in the notion of Lawrence [70]) for unconstrained movements can be achieved easily. Diolaiti et al. [33] lists the parameters of several haptic devices. For all of them, the ratio of physical damping to mass b_D/m_D is smaller than $0.625s^{-1}$. With these findings, the following limits for the normalized parameters can be stated,

$$\begin{aligned} 0 &\leq \gamma < T^2 \cdot 710 s^{-2} \\ 0 &\leq \delta < T \cdot 15.225 s^{-1}, \end{aligned} \quad (3.16)$$

if the cases of an ungrabbed device $k_H = b_H = 0$, and of an ideal undamped device $\delta = 0$ are also permitted. To account for the fact that reliable values for the physical parameters of human operators and haptic devices are in general quite imprecise values, parameter ranges extended by roughly 30% will be considered, see Fig. 3.5. Finally, it will be assumed that the sampling time T for haptic systems is limited from above at 1 ms because this is a widely accepted limit for haptic rendering [11]. Therefore, the following parameter ranges will be considered:

$$\begin{aligned} 0 &\leq \gamma \leq 1 \cdot 10^{-3} \\ 0 &\leq \delta \leq 20 \cdot 10^{-3}. \end{aligned} \quad (3.17)$$

The following section determines stability boundaries for these parameter ranges.

3.4 Stability Boundaries

The previous sections derived the normalized characteristic polynomial of the control loop in Fig. 3.3 and identified realistic parameter ranges for the two parameters γ and δ .

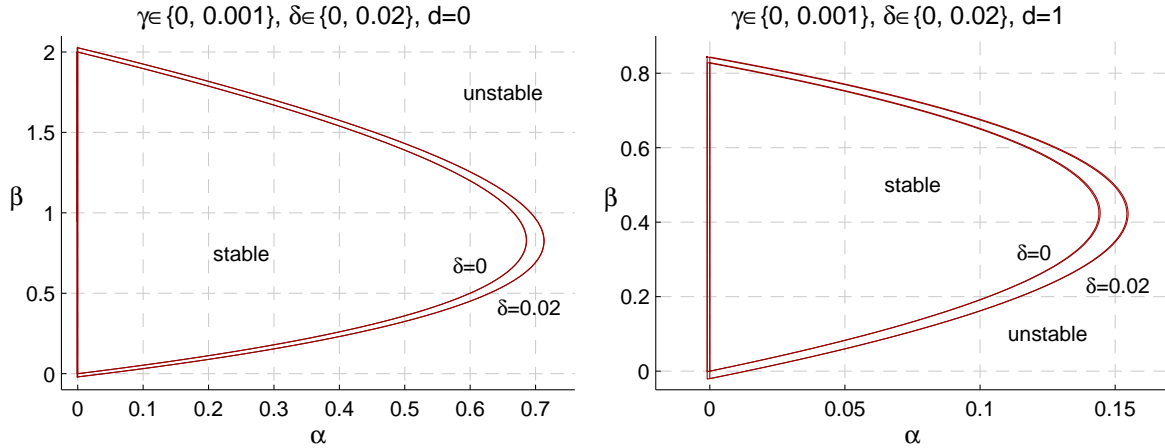


Figure 3.6: Stability boundaries in the (α, β) -plane for $d = 0$ (left) and $d = 1$ (right), and for the limits of the parameter range $\gamma \in [0, 0.001]$ and $\delta \in [0, 0.02]$.

This section utilizes these results to derive the stability boundaries of the considered system. These boundaries are determined in the parameter plane of the two virtual parameters α and β , since these parameters are usually the parameters of a haptic system that can be changed most easily. Moreover, the boundaries define the stable parameter regions, which size is often denoted as Z-width in the context of haptic rendering [21].

Analytical solutions for stability could be found by using standard stability analysis methods, such as the Jury or the Routh-Hurwitz stability criterion [75]. These methods yield a set of inequalities. The stable parameter space is the intersection of the parameter spaces defined by these inequalities. As the number of inequalities and their complexity depends directly on the degree of the characteristic polynomial (3.11),

$$\deg(p(z)) = d + 3, \quad (3.18)$$

the analytical stability analysis quickly becomes quite complex for increasing delay d . An explicit solution for the case $d = 0$ and $\gamma = 0$, i.e., without time delay and physical stiffness, was derived by Gil et al. [35]. Already for a delay of $d = 1$, only an implicit solution could be determined [37]. Therefore, for larger delays or non-zero stiffness γ an iterative gridding method is used to determine the stable parameter space of the considered system.

This iterative method uses grid values of the investigated system parameters, and performs a stability check for each grid point by computing the poles of the discrete-time transfer function (3.9). The system is stable if all the poles are located inside the unit circle [61]. If there is a transition from stable to unstable, or vice-versa, between two adjoining grid points, a more precise transition point is determined by iterating the stability check on a finer grid, until a predefined threshold¹ has been reached. The

¹For the stability boundaries presented in this work, a threshold of $10^{-8}/(d+0.5)^2$ has been chosen for α , and $10^{-8}/(d+0.5)$ for β .

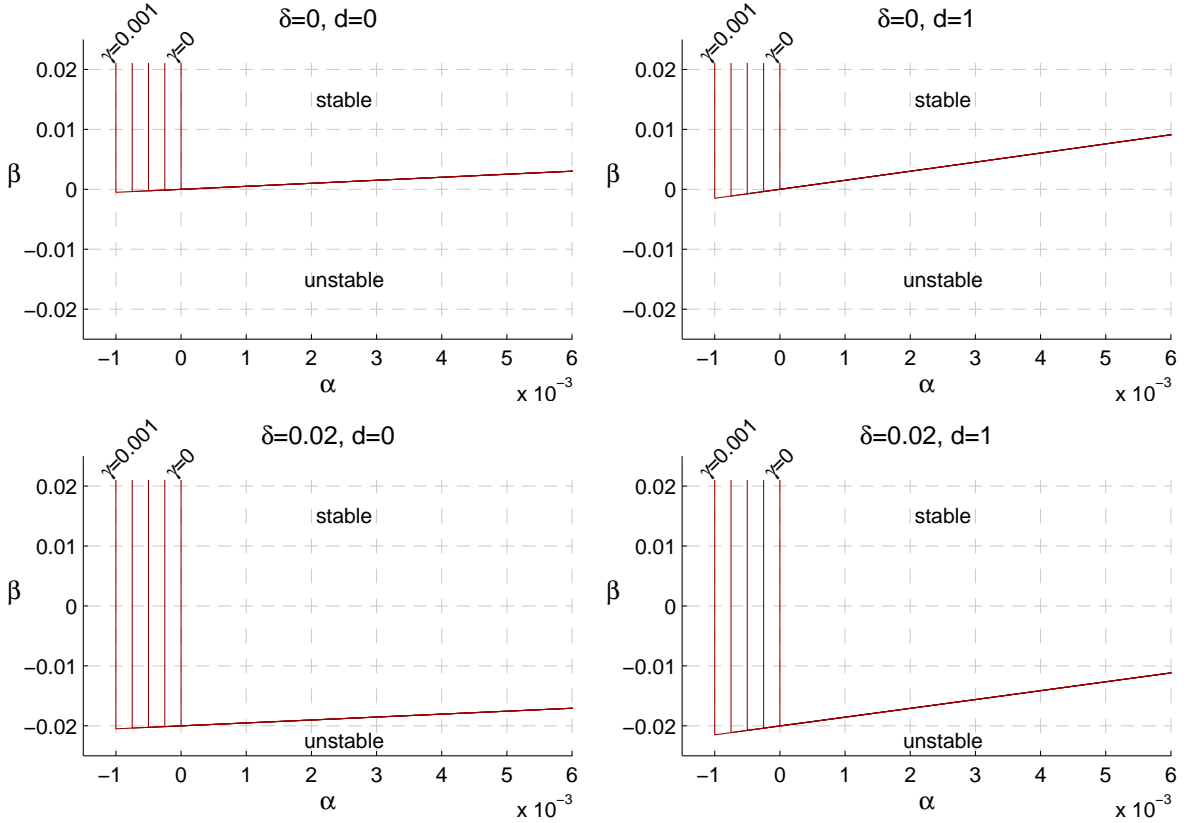


Figure 3.7: Close-up of Fig. 3.6 around the origin, with additional values for γ , i.e., $\gamma \in \{0, 0.25, 0.5, 0.75, 1\} \cdot 0.001$. Physical stiffness γ shifts the left boundary to $\alpha = -\gamma$ and does not visibly influence the bottom boundary.

two most common cases for delay are addressed first, i.e.

d=0: direct (undelayed) action

d=1: one sampling step delayed action

Figure 3.6 shows the stability boundaries in the normalized (α, β) -plane for these two cases, and for the limits of the possible parameter ranges of γ and δ , which were derived in the previous subsection. The system is stable in the areas that are surrounded by the boundaries.

These stable regions have a left vertical straight bound at $\alpha = -\gamma$. From the right side, i.e., for $\alpha > -\gamma$, they are bounded by parabola-like curves. When considering the normalization rule for the virtual stiffness, $\alpha = KT^2/m$, it becomes obvious that the (non-normalized) maximum stable virtual stiffness K depends quadratically on the sampling period T . Thus, a double sampling frequency with constant delay factor d (i.e., half time delay $t_d = dT$) enables a four times higher virtual stiffness K .

It is interesting to note that an increase of virtual damping does not automatically result in higher dissipation. Rather, as there is an upper bound for β , a too high virtual damping itself can destabilize the system. This bound for the virtual damping B (as non-normalized parameter) depends linearly on the mass m and the sampling rate $1/T$.

On the other hand, physical damping δ increases the stable region, which can be explained by the dissipative behavior of a physical damper. Only the left vertical bound of the stable region is uninfluenced by δ . This left vertical bound is affected solely by the physical stiffness γ , which shifts it further to the left towards $\alpha = -\gamma$. This means that also negative values of virtual stiffness can lead to stable behavior as long as the sum of virtual and physical stiffness is greater than zero. This relationship is illustrated by the close-up views around the origin in Fig. 3.7. The influence of γ on the parabola-like part of the boundaries is rather marginal. Only for much higher stiffness values than admitted by the possible range $\gamma \gg 0.001$, the influence becomes clear, as will be detailed in the next chapter.

For an increasing delay, the stable region quickly becomes smaller. This detrimental effect of delay on the stable regions is illustrated in Fig. 3.8, which shows the stability boundaries for several delay factors $d \in \{0, 0.25, 0.5, 1, 2, 4, 8\}$ exemplarily for the upper bounds of the admitted parameter ranges $\gamma = 0.001$ and $\delta = 0.02$. With increasing delay, the stable region shrinks towards the point of origin. The dash-dotted line in Fig. 3.8 crosses the right-most points of all stability boundaries and therefore represents the curve for maximum stable stiffness α_{\max} .

The effect of delay on this maximum stiffness can be illustrated more clearly, when drawing α_{\max} over the delay factor d , as shown in the left plot of Fig. 3.9 for the considered parameter ranges of γ and δ . The numerical values for α_{\max} on these curves can be found in Appendix B. This result reveals that a delay of only one sampling period causes the maximum stable stiffness to decrease already to less than 22% of the undelayed counterpart. For a delay of two sampling steps $d = 2$, not even 10% of the undelayed stiffness can be reached. The right plot of Fig. 3.9 shows similarly the curves for maximum stable virtual damping β_{\max} . For this parameter, the relative influence on delay is weaker compared to α_{\max} , so that the maximum virtual damping β_{\max} experiences a drop to approximately 41% of the undelayed counterpart for $d = 1$, and 27% for $d = 2$.

It is interesting to note that due to the high dependency of the stable region on time delay, the influence of physical stiffness γ inside its bounds becomes visible in the overall shape of the stable region with a delay of only two sampling periods $d = 2$. Thus, it appears that the physical stiffness γ shifts the stability boundaries to the left and at the same time increases the overall size of the stable region, as shown in Fig. 3.10 for $d = 2$ and $d = 4$. This effect will become clearer in the next chapter, in which much greater values for γ are considered.

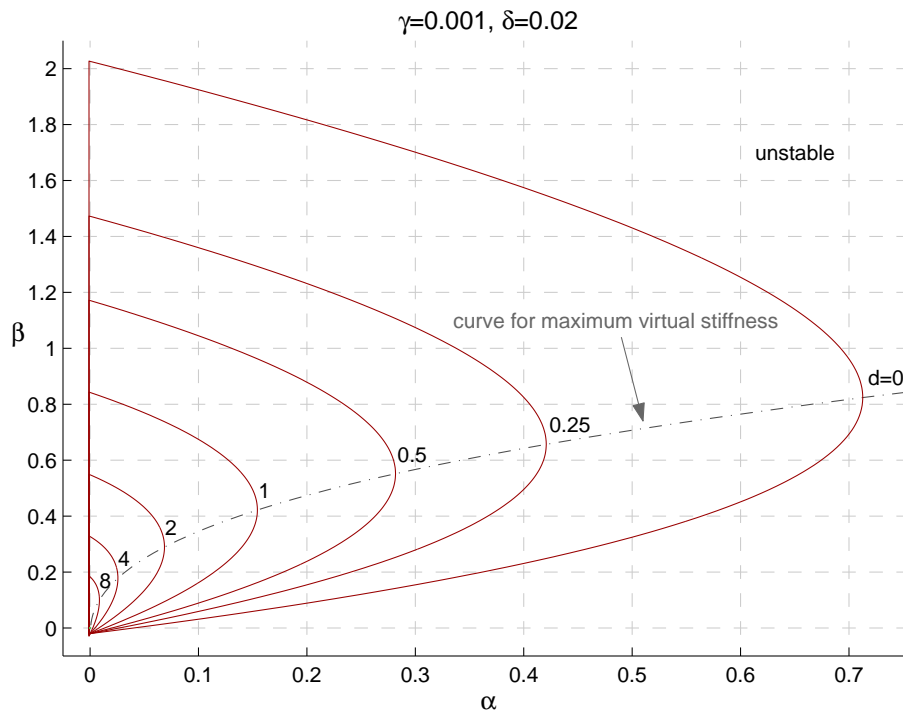


Figure 3.8: Stability boundaries in the (α, β) -plane for $\gamma = 0.001$, $\delta = 0.02$ and delay factors $d \in \{0, 0.25, 0.5, 1, 2, 4, 8\}$. The dash-dotted line is the curve for maximum stable stiffness α_{\max} .

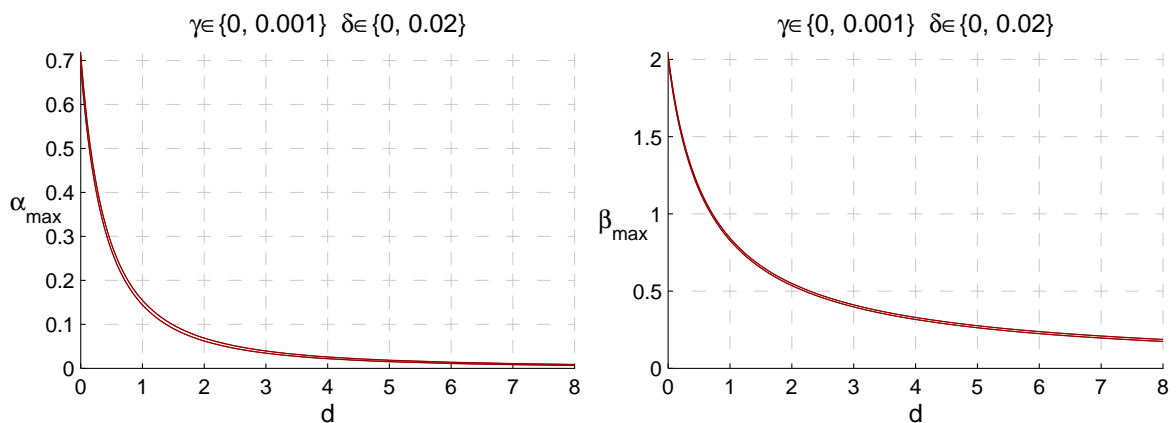


Figure 3.9: Influence of the delay factor d on the maximum stable stiffness α_{\max} (left) and damping β_{\max} (right). See Appendix B for the numerical values.

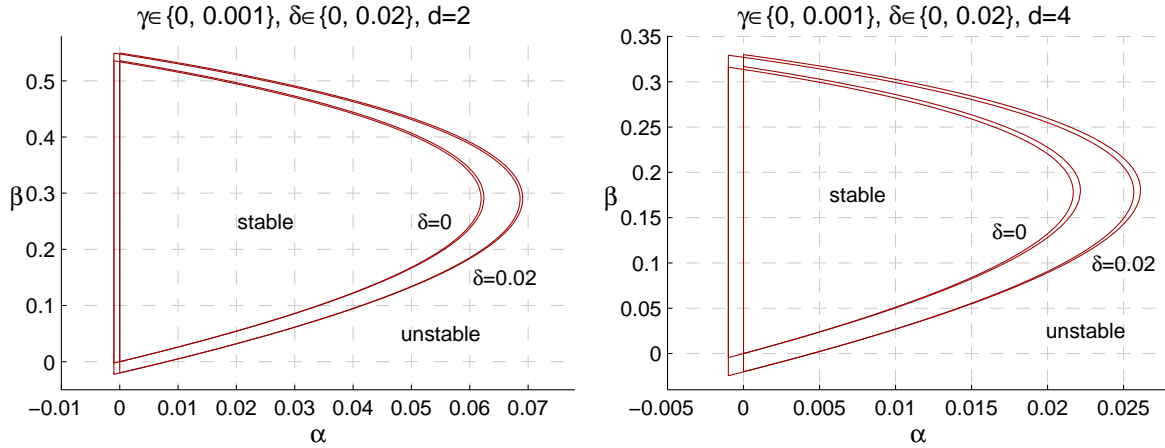


Figure 3.10: Stability boundaries in the (α, β) -plane for $d = 2$ (left) and $d = 4$ (right) for the limits of the parameter range $\gamma \in [0, 0.001]$ and $\delta \in [0, 0.02]$. The physical stiffness γ shifts the boundaries to the left.

To conclude, physical damping increases the stable region, whereas delay decreases it. The physical stiffness increases the size of the stable region and shifts it to the left. Thus, it contributes to stability around the point of origin, whereas it reduces stability for large virtual stiffnesses. Due to the normalization rules, which have the total (i.e., contributing human and device) mass m in the denominator, also this mass contributes to stability, as it linearly scales the stable regions for the non-normalized parameters K and B . The influence of the human is mainly constituted by its mass, as the influence of spring and damper are very limited due to the numerically small parameter ranges.

3.5 Linear Stability Condition

When considering the virtual stiffness values typically employed in haptic simulations, it appears that for α usually small numerical values occur. For all devices listed by Diolaiti et al. [33], a value of $\alpha = 0.03$ is not exceeded. For such small values, the stability boundary can be linearized around the origin. It will turn out that such a linear condition is very useful because it reveals fundamental parameter dependencies for small values of α and β in non-normalized parameters. In accordance with [36, 56, 37], the linear condition will be obtained by applying the Routh-Hurwitz criterion in the Laplace domain.

If the effect of sampling and hold is approximated by a delay of half a sampling step $T/2$, which is a valid approximation for slow dynamics [2], then the continuous-time characteristic equation of the control loop in Fig. 3.3 yields

$$1 + \frac{K + Bs}{ms^2 + bs + k} e^{-(t_d + T/2)s} = 0. \quad (3.19)$$

Further, substituting the effective delay $t_r = t_d + T/2$ and approximating $e^{-t_r s} \approx \frac{1}{1 + t_r s}$

yields

$$mt_r s^3 + (bt_r + m)s^2 + (kt_r + b + B)s + k + K = 0. \quad (3.20)$$

By applying the Routh-Hurwitz criterion and assuming that the physical parameters m, T, t_d, b, k are positive, three inequalities result:

$$b + B > -kt_r, \quad (3.21)$$

$$K > -k, \text{ and} \quad (3.22)$$

$$bt_r(b + B + kt_r) + m(b + B - Kt_r) > 0. \quad (3.23)$$

The last inequality can be rewritten as

$$b + B + \underbrace{bt_r(b + B + kt_r)/m}_{\epsilon} > Kt_r. \quad (3.24)$$

Under the assumption of fast haptic sampling rates $T \leq 1$ ms and small delay d , and under condition (3.21), the summand ϵ is a small positive value that can be neglected. Then inequality (3.24) simplifies to

$$K < \frac{b + B}{t_r}. \quad (3.25)$$

Since (3.21) is implied in (3.22) and (3.25), it is not representing an additional constraint.

This linear condition states that the virtual stiffness K must be smaller than the sum of dampings $b + B$ divided by the effective delay t_r , or in other words

$$\text{Virtual Stiffness} < \frac{\sum \text{Damping}}{\sum \text{Delay}}. \quad (3.26)$$

It is the same condition as for haptic systems without a human operator [37] because the physical stiffness k does not influence this condition. Physical stiffness only shifts the lower limit in which the condition holds to $K > -k$. Note that the linear condition differs slightly to the condition determined by Minsky et al. in [81], as they did not distinguish between discrete-time and continuous-time stiffnesses. In their calculations the human stiffness k_H has the same destabilizing effect as a discrete-time spring.

The linear condition (3.25) can be also written in normalized parameters,

$$\beta + \delta > \alpha(1/2 + d), \quad (3.27)$$

in order to compare it to the curved stability boundaries introduced in the previous subsection. Figure 3.11 shows the exact curved boundaries (solid) and this linear condition (dashed) in the same plots for values of the physical parameters that are inside the considered parameter range. As physical stiffness in its admissible range hardly influences the stability boundaries, this figure shows exemplarily the curves for

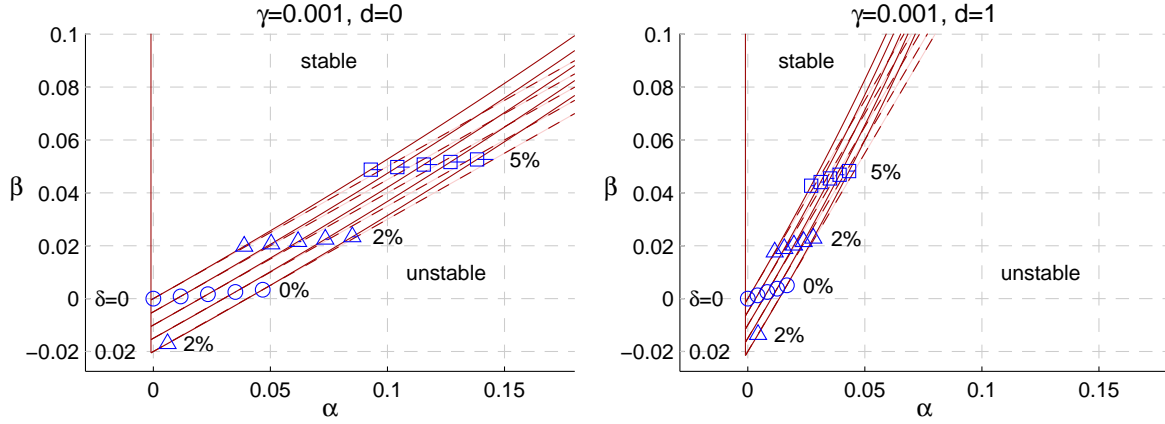


Figure 3.11: Comparison of the linear stability condition (dashed) to the exact stability boundaries (solid), for $\gamma = 0.001$, $\delta \in \{0, 0.005, 0.01, 0.015, 0.02\}$, and $d = 0$ (left) resp. $d = 1$ (right). The relative error of the linear condition is marked in three levels, 0% (circles), 2% (triangles) and 5% (squares).

the upper limit $\gamma = 0.001$. It visualizes also the points at which the relative error of the linear condition, defined by

$$|(\alpha_{\text{lin}} - \alpha)/(\alpha + \gamma)|, \quad (3.28)$$

reaches levels of 0% (circles), 2% (triangles) and 5% (squares), whereby α and α_{lin} are located on the exact respectively linear stability boundary for the same β . It appears that for damping values greater than $\delta > 0.015$ there are cases in which the relative error is greater than 2% also for negative β .

The linear condition crosses the stability boundaries at the points where the relative error is 0%, i.e. at the blue circles in Fig. 3.11. Above these crossing points the linear condition is located on the unstable side of the stability boundary. Therefore, strictly speaking the linear stability condition cannot be used to design stable control parameters for the virtual wall in this parameter range. Although these findings limit the use of the linear condition, this condition remains instructive with respect to the parameter dependencies for stability.

3.6 Discussion

This chapter presented a stability analysis on a one degree of freedom haptic device that is held by a human arm. The haptic device is interacting with a virtual environment represented by a discrete-time spring-damper system including time delay. The human arm is modeled as linear mass-spring-damper system. For this model, the set of admissible human operator parameters was defined, taking into account various findings from other research groups.

A peculiarity of the presented approach is the exact combination of discrete- and continuous-time elements. This exact analytical formulation leads to a system that can be significantly simplified by certain parameter normalizations. In detail, the two parameters sampling time T and mass m could be removed from the characteristic polynomial. Their influence is only constituted implicitly by scaling the normalized parameters. With this parameter normalization, it was possible to determine stability boundaries analytically (for $d \in \{0, 1\}$) and numerically (for arbitrary delay d), and draw these curves in a normalized parameter plane. This representation allowed to analyze and clearly illustrate the effect of each system parameter on stability. The following lines detail the influence of delay, sampling rate, physical damping, and mass on the stable parameter region.

Time delay drastically affects the stability of the haptic system. A delay of one sampling period decreases the maximum stable virtual stiffness to less than 22% of its undelayed value. Similarly, the maximum virtual damping reduces to approximately 41%. In comparison, the **sampling rate** is directly scaling the normalized parameters and hence the size of the stable region. For the virtual stiffness, the dependency is quadratic, whereas virtual damping is linearly affected by the sampling rate. As these relations assume a constant delay factor d , time delay is scaling with the sampling period. In other words, two times faster sampling and accordingly half delay enables four times higher virtual stiffness, but only two times higher damping.

Physical damping dissipates kinetic energy and hence increases the stable region. Therefore, with higher physical damping, higher maximum virtual stiffness and damping factors can be adjusted. In comparison, **physical stiffness** increases the overall size of the stable region, but at the same time shifts it to the left towards lower virtual stiffness. That is why the maximum stable virtual stiffness decreases with increasing physical stiffness (this relation will be more extensively discussed in the next chapter). However, inside their admissible ranges these two physical parameters are only marginally affecting stability, as they are numerically small compared to their maximum stable discrete-time counterparts.

The dynamic **mass**, which is a combination of human arm and device mass, is proportionally scaling the stable region. Therefore, the influence of the human arm as a mass-spring-damper system is mainly constituted by the additional mass contribution. A doubling of the total dynamic mass enables a doubling of virtual stiffness and damping. However, higher virtual stiffness and damping do not lead to faster dynamics, if mass increases equally. The dynamics rather depend on the ratios of stiffness and damping to the total dynamic mass.

From these dependencies the following guidelines for designing stable haptic systems can be derived:

1. Try to minimize effective delay, composed of time delay and the phase shift caused by discrete-time sampling. A much faster sampling does not significantly improve performance, if time delay outweighs the effect of discrete-time sampling.
2. In order to improve the transparency of a haptic device, try to minimize physical damping as it contributes only marginally to stability.
3. As a haptic device with very low mass is highly affected by the human mass, do not try to minimize the haptic device mass. This recommendation contrasts traditional design goals for haptic devices, which aim at maximizing transparency. A sensible trade-off between transparency and stability might be designing devices for which the moving mass is in the range of the human mass contribution.

From the stability boundaries, an easy-to-use method for determining the two parameters of physical stiffness and physical damping may be derived. As the sum of virtual and physical stiffness must be greater than zero, the physical stiffness that is present in a haptic system corresponds to the absolute value of the critical negative virtual stiffness at which the system is marginally stable. Hence, if the virtual stiffness is decreased (comprising negative stiffness factors) until the stability limit, its absolute value corresponds to the physical stiffness of the haptic system. The same holds for the damping, provided that the virtual stiffness is zero.

Further investigations analyzed a linear approximation of the stability boundaries around the point of origin that could be formulated as linear stability condition. It states that the instability introduced by the product of virtual stiffness and effective delay can be compensated by any kind of viscous damping, discrete- or continuous-time one. Although this linear approximation has a small relative error over a wide range compared to the precise stability boundaries, it cannot be used to design stable system parameter values in general because it is located partly outside of the stable region.

Nevertheless, this linear approximation is very informative with regard to the relation of the involved system parameters. It reveals that in the range in which this linear approximation holds, discrete-time damping has the same dissipative behavior as its continuous-time counterpart. The physical stiffness of the human arm has no effect on the linear condition.

The following two chapters investigate how the stable regions relate to passivity, and how optimal performance could be achieved.

Energy is one of the fundamental concepts in science and engineering practice, where it is common to view dynamical systems as energy-transformation devices.

Ortega et al. [88]

4

Passivity Analysis

The stability analysis depends highly on the system model of the human operator. Not only the diversity of human arm characteristics, but also the various possibilities of grasping haptic devices make it particularly difficult to determine a valid model of the human arm. This often leads to strong simplifications for analyzing stability. Also in the previous chapter a simple model of the human arm was used, while the variety of the human operator was taken into account by defining wide parameter ranges for the human model.

Another widely employed approach does not require a model for the human operator at all. It is assuming passivity for the haptic device, and utilizing the fact that a human can always interact in a stable manner with a passive device [33]. Also Colgate and Schenkel [24] utilized this fact for deriving their famous passivity condition for haptic rendering. With their condition, a virtual wall can be parameterized in a passive way such that energy can never be extracted from the haptic system.

In this chapter, a passivity analysis is introduced taking time delay into account. It is based on the general passivity condition from Colgate and Schenkel [24]. This analysis allows for drawing passivity boundaries in the same parameter plane used for the stability boundaries, and therefore makes possible to directly compare passive to stable parameter regions. The same haptic system will be considered as in the previous chapter, except for the human arm no assumptions need to be made and no model is employed. Hence, the combined system parameters from (3.2) become

$$m = m_D \quad b = b_D \quad k = 0. \quad (4.1)$$

This chapter mainly presents results from my recent article [48] and is structured as follows. Sect. 4.1 derives an analytical passivity condition for delayed virtual environments. This condition is transformed into its explicit form in Sect. 4.2, in order to

illustrate the passivity boundaries of the system. Sect. 4.3 relates these boundaries to the stability boundaries determined in the previous chapter, and answers the following questions:

- How do passive parameter regions relate to the stable ones (Sect. 4.3.1)?
- How much is passivity restricting the virtual wall stiffness compared to stability (Sect. 4.3.2)?
- Why is passivity conservative in terms of stability (Sect. 4.3.3)?

Finally, Sect. 4.4 discusses the main results and draws important conclusions with respect to passivity for haptic systems.

4.1 Passivity Condition for Virtual Walls affected by Time Delay

This section presents the passivity condition for virtual walls with time delay. A common continuous-time definition of passivity, which is based on mechanical energy using the conjugate power variables force F and velocity \dot{x} is [42]:

Definition 4.1. *A one-port network with initial energy storage $E(0)$ at time $t = 0$ is continuous-time passive if and only if*

$$\int_0^t F(\tau)\dot{x}(\tau)d\tau + E(0) \geq 0, \quad \forall t \geq 0, \quad (4.2)$$

for force $F \in \mathbb{R}$ and velocity $\dot{x} \in \mathbb{R}$.

In order to derive their passivity condition, Colgate and Schenkel [24] consider a slightly more restrictive statement for haptic devices,

$$\int_0^t F(\tau)\dot{x}(\tau)d\tau > 0, \quad \forall t > 0. \quad (4.3)$$

It says that the energy input to the haptic device must be positive for all times greater than zero. Based on this condition, they found the following passivity condition for a haptic device with physical damping b that displays a discrete-time linear shift-invariant¹ system $H_F(z)$,

$$b > \frac{T}{2} \frac{1}{1 - \cos \omega T} \Re\{(1 - e^{-j\omega T})H_F(e^{j\omega T})\}, \quad 0 \leq \omega \leq \omega_N \quad (4.4)$$

with imaginary unit j , and Nyquist frequency $\omega_N = \pi/T$. It can be shown that this condition also holds for virtual walls with a unilateral constraint [24].

¹Shift-invariance is the discrete-time equivalent of time-invariance [115].

This passivity condition can be applied on the delayed virtual environment presented in the previous chapter. The transfer function of this virtual environment, composed of a spring and a damper, and delayed by d sampling steps, reads

$$H_F(z) = \left(K + B \frac{z-1}{Tz} \right) \frac{1}{z^d}. \quad (4.5)$$

Given this transfer function, passivity condition (4.4) can be solved analytically for constant $d \geq 0$ using the equality for the exponential function for complex arguments $e^{a+jb} = e^a(\cos b + j \sin b)$, resulting in

$$b > \left((\cos(d\omega T) - \cos((d+1)\omega T))KT + (\cos(d\omega T) - 2\cos((d+1)\omega T) + \cos((d+2)\omega T))B \right) / (2 - 2\cos\omega T), \quad (4.6)$$

for $0 < \omega < \omega_N$, assuming $m > 0$ and $T > 0$. Note that this condition is independent of mass m . For $d = 0$, it results in $b > KT/2 - B \cos(\omega T)$, which can be easily summarized as

$$b > \frac{KT}{2} + |B|, \quad (4.7)$$

and which is the linear passivity condition for virtual walls without time delay, found by Colgate and Schenkel in [24].

4.2 Passivity Boundaries

In haptic simulations the parameters of the virtual environment usually can be adapted more easily than those of the haptic device. Thus, it is helpful to draw the passivity boundaries in a plane depending on K and B . The following paragraph solves the passivity condition (4.6) for these two parameters.

For a given damping b , delay d and frequency ω , the boundary of the passivity region (4.6) is a straight line $l(b, d, \omega)$ in the (K, B) -plane. To determine an explicit representation of the general passivity boundaries that are independent of ω , two of these lines $l(b, d, \omega)$ and $l(b, d, \omega + \epsilon)$ must be crossed, with ϵ being an arbitrarily small positive quantity. Thus, the explicit representation results in

$$\begin{pmatrix} K \\ B \end{pmatrix} = 2b \cdot \begin{pmatrix} \frac{d+1}{T} \frac{\sin((d+2)\omega T) - 2\sin((d+1)\omega T) + \sin(d \cdot \omega T)}{\sin(2(d+1)\omega T) - 2(d+1)\sin(\omega T)} \\ \frac{d \cdot \sin((d+1)\omega T) - (d+1)\sin(d \cdot \omega T)}{\sin(2(d+1)\omega T) - 2(d+1)\sin(\omega T)} \end{pmatrix}. \quad (4.8)$$

This equation reveals a linear dependency between the virtual wall parameters and the physical damping b , and additionally the sampling period T for K . Therefore, it is possible to draw the passivity boundaries in a (K, B) -plane normalized by b and T .

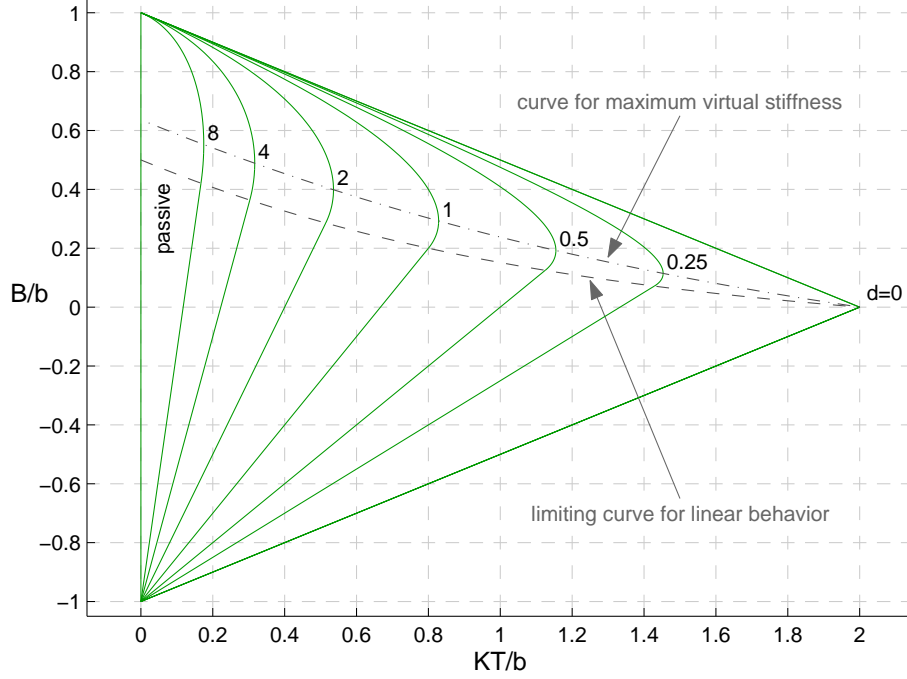


Figure 4.1: The passivity boundaries of a haptic device rendering a virtual wall for different delay factors $d \in \{0, 0.25, 0.5, 1, 2, 4, 8\}$. In the lower parts of these boundaries the relation between KT/b and B/b is linear.

Figure 4.1 visualizes these boundaries for different delay factors d . Note that this normalization, which originally was found by Colgate and Schenkel [24] for the passivity of undelay haptic systems, differs fundamentally to those of the stability analysis.

The two limiting points of the passivity boundaries are $(K, B) = (0, b)$ and $(K, B) = (0, -b)$, independent of time delay d . The upper point at $B = b$ describes the point with the maximum possible passive virtual damping. It is reached at a frequency $\omega|_{B_{\max}} = \pi / T(d + 1)$ for a given delay d . At that frequency passivity condition (4.6) converges to the linear condition $b > KT/2 + B$, also independent of delay d . This condition corresponds to the upper part of the passivity boundary (4.7) for $d = 0$.

The lower parts of the passivity boundaries in Fig. 4.1 are linear. They can be derived as limits of the explicit passivity condition (4.8) at $\omega \rightarrow 0$ as

$$\begin{pmatrix} K \\ B \end{pmatrix}_{\text{lin}} = \begin{pmatrix} \frac{b}{T} \frac{6(d+1)}{(2d+1)(2d+3)} \\ b \left(\frac{d}{2d+3} + 1 \right) \end{pmatrix} \cdot y + \begin{pmatrix} 0 \\ -b \end{pmatrix}, \quad y \in [0, 1], \quad (4.9)$$

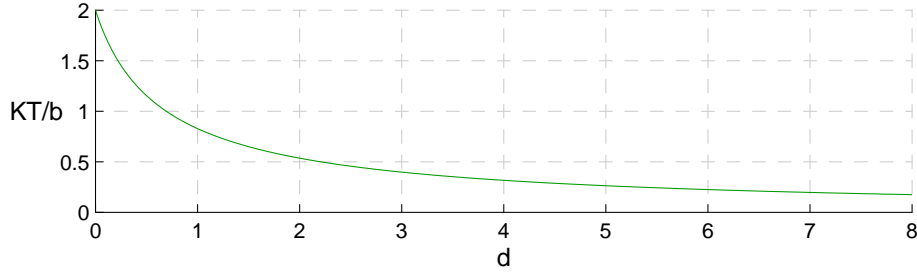


Figure 4.2: Influence of the delay factor d on the maximum passive stiffness K_{\max} in the normalized representation of Fig. 4.1.

which can be rewritten as

$$K < \frac{b + B}{(0.5 + d)T}, \quad \text{for } B \in \left[-1, \frac{d}{2d + 3}\right] b. \quad (4.10)$$

This condition corresponds exactly to the linear stability condition introduced in the previous chapter. It has been recently confirmed by another research group which was using an alternative analytical approach [79].

In haptic applications it is often interesting to know at which point the maximum virtual stiffness K can be reached. This point is the rightmost point on the passivity boundaries for given delay d in Fig. 4.1. In this point the coefficient of the virtual damping B vanishes in passivity condition (4.6), which holds true for the frequency $\omega|_{K_{\max}} = \pi / 2T(d + 1)$. Thus, the (K, B) value pairs for maximum possible passive virtual stiffness K_{\max} results as

$$\begin{pmatrix} K \\ B \end{pmatrix}_{K_{\max}} = b \cdot \begin{pmatrix} \frac{2}{T} \frac{1 - \cos\left(\frac{1}{2} \frac{\pi}{d+1}\right)}{\cos\left(\frac{1}{2} \frac{\pi d}{d+1}\right)} \\ \frac{\sin\left(\frac{1}{2} \frac{\pi d}{d+1}\right) - \frac{d}{d+1}}{\sin\left(\frac{1}{2} \frac{\pi}{d+1}\right)} \end{pmatrix}. \quad (4.11)$$

which is plotted as dash-dotted curve in Fig. 4.1. The influence of time delay d on K_{\max} is illustrated in Fig. 4.2. Already for a delay of only one sampling step, i.e., $d = 1$, the maximum stiffness reduces to approximately 41% of its undelayed value, and for $d = 2$ less than 27% of the stiffness of the undelayed case can be reached.

4.3 Comparison of Passivity to Stability

Above sections derived passivity boundaries for the considered haptic system. This section compares these curves to the stability boundaries of the previous chapter. Moreover, it relates the maximal virtual stiffnesses that can be achieved passively and stably. Finally, it analyzes stability for great values of physical stiffness, to build the bridge between stability and passivity.

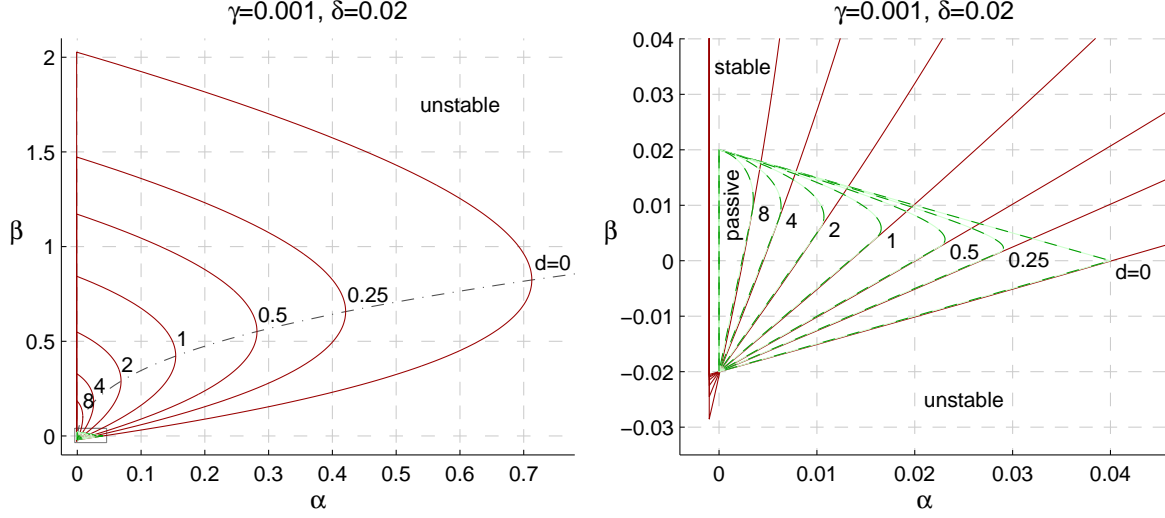


Figure 4.3: The passivity boundaries (dashed green curves) and the stability boundaries (solid red curves) for $\gamma = 0.001$ and $\delta = 0.02$ in the same (α, β) -plane for different delay factors $d \in \{0, 0.25, 0.5, 1, 2, 4, 8\}$. The passive regions are inside the stable regions for a given delay. The right plot is a close-up view around the origin of the left plot.

4.3.1 Relation between Passivity and Stability Boundaries

When applying the normalization rules for the dimensionless parameters of Table 3.1, and assuming $m/T > 0$ the explicit representation of the passivity boundaries (4.8) becomes

$$\begin{pmatrix} \alpha \\ \beta \end{pmatrix} = \delta \cdot \begin{pmatrix} 2(d+1) \frac{\sin((d+2)\hat{\omega}) - 2\sin((d+1)\hat{\omega}) + \sin(d\hat{\omega})}{\sin(2(d+1)\hat{\omega}) - 2(d+1)\sin(\hat{\omega})} \\ 2 \frac{d \sin((d+1)\hat{\omega}) - (d+1)\sin(d\hat{\omega})}{\sin(2(d+1)\hat{\omega}) - 2(d+1)\sin(\hat{\omega})} \end{pmatrix}. \quad (4.12)$$

for $\hat{\omega} = \omega T$ and $0 < \hat{\omega} < \pi$. Similarly to the stability analysis of the previous chapter, the parameter sampling period T drops out also for passivity. This normalized equation defines the normalized passivity boundaries, which are proportionally scaled by the physical damping δ . For given δ and d , these boundaries can be plotted in the same (α, β) -plane as the stability boundaries. Figure 4.3 shows both kinds of boundaries for $\gamma = 0.001$, $\delta = 0.02$, and $d \in \{0, 0.25, 0.5, 1, 2, 4, 8\}$ at two different scales. The left plot shows the overall picture, which illustrates that the dimensions of the passive regions are much smaller than those of the stable ones.

To present the passive regions more clearly, the right plot in Fig. 4.3 shows a close-up view around the origin. This figure reveals that the passive region is a subset of the corresponding stable region, which is not only true for the given set of parameters, $\gamma = 0.001$, $\delta = 0.02$, and $d \geq 0$, but is a generally valid statement. This result supports the fact that the passivity condition is conservative in terms of stability [24].

The size of the passive regions is directly proportional to the physical damping δ , whereas the stable regions change much less with changing δ (see the previous section). In the shown case for $\delta = 0.02$ the passive regions are maximal for the considered parameter range. Thus, for smaller values of δ the relative difference in size between the passive and the stable region becomes even larger.

4.3.2 Maximum Passive and Stable Stiffness

A fundamental requirement for a haptic system is that it is able to display a wide range of stable stiffness values. For soft contacts, the virtual stiffness can be set to small values without causing stability problems. Yet, when increasing virtual stiffness, stability becomes an issue and leads to the question, what maximal stiffness can be realized before the system becomes unstable. The following lines show how the maximum passive and stable stiffness change with increasing time delay, and compare the resulting two curves.

The maximum stable stiffness is given by the rightmost point on the stability boundary. When delay is changing, this point is moving with the boundary such that a path with maximal stable stiffness results. In Fig. 4.3, this path is plotted as a dash-dotted line, in analogy to the path for maximal passive stiffness, which was presented above in Fig. 4.1.

Figure 4.4 illustrates the difference between the maximum passive and stable stiffness dependent on the delay factor d . The first plot (Fig. 4.4(a)) shows directly the curves for these stiffness values. The maximum stable stiffness is clearly higher than the passive stiffness.

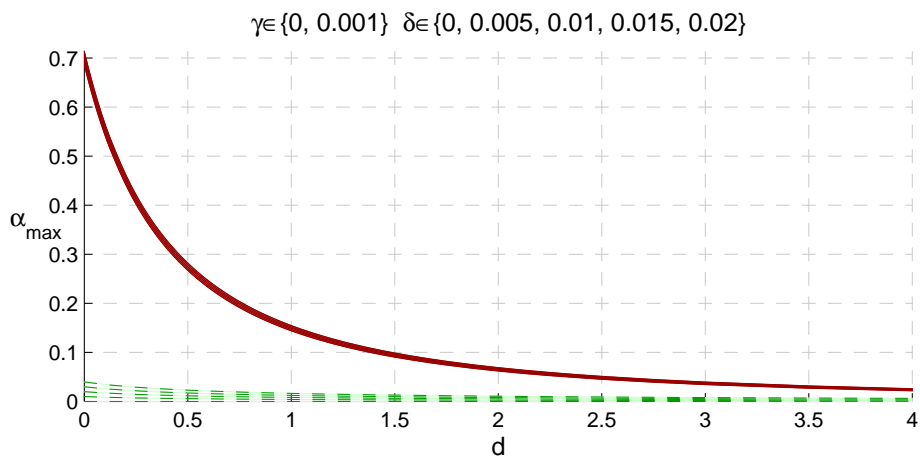
The lower two plots (Fig. 4.4(b) and 4.4(c)) illustrate the relation η of the maximum passive to the maximum stable virtual stiffness for two different scales of the delay factor d . They show that for increasing delay the relation η becomes greater until the maximum passive and stable stiffnesses are the same at $\eta = 1$. This means that up to this point, the maximum stable stiffness depends higher on time delay than its maximum passive counterpart.

For $d = 0$, the maximum stable virtual stiffness is more than 17.8 times higher than achievable by passivity ($\eta_{d=0} < 0.0562$). If the delay increases to $d = 1$, this ratio decreases to values greater than 9.3 ($\eta_{d=1} < 0.1074$).

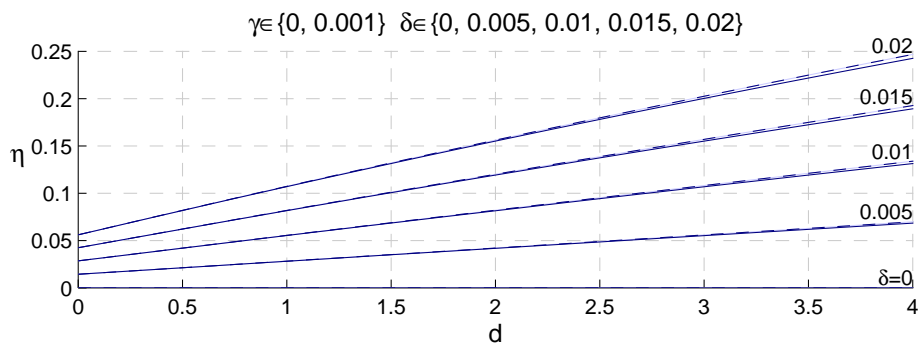
4.3.3 Passivity and Robust Stability

In this subsection a connection between stable and passive regions is found. In contrast to previous assumptions, where a limited parameter range for the physical stiffness γ was considered, motivated by the stiffness that a human arm can apply, much greater values for γ are permitted. The physical stiffness influences the oscillation frequency

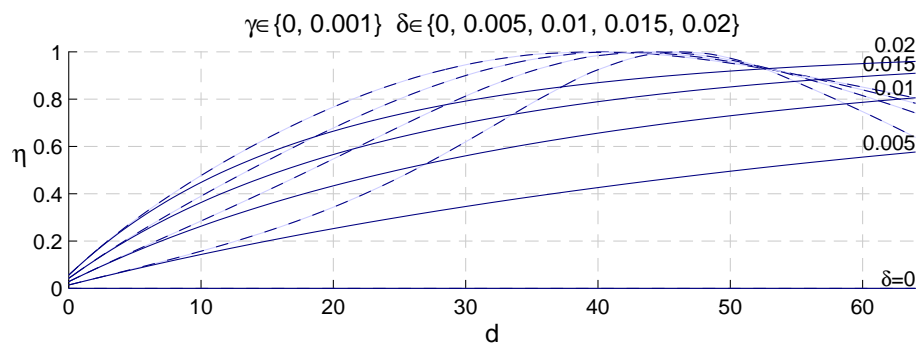
$$\omega = \sqrt{\frac{k}{m} - \frac{b^2}{4m^2}}, \quad \text{for } k > \frac{b^2}{4m} \quad (4.13)$$



(a) maximum virtual stiffness for passivity (dashed green curves) and stability (solid red curves)



(b) relation of maximum virtual stiffness for passivity and stability for $\gamma = 0$ (solid) and $\gamma = 0.001$ (dashed)



(c) relation of maximum virtual stiffness for passivity and stability for $\gamma = 0$ (solid) and $\gamma = 0.001$ (dashed)

Figure 4.4: The maximum virtual stiffness α for passivity and stability, and their ratio η .

of the physical mass-spring-damper system given by the haptic device and the human operator. Substituting the physical by the normalized parameters yields

$$\omega = \frac{\sqrt{\gamma - \delta^2/4}}{T}. \quad (4.14)$$

Since the stability analysis in this article is performed in the discrete-time domain, the oscillation of the mass cannot be observed correctly, if it exceeds the Nyquist frequency $\omega_N = \pi/T$. Therefore, this section investigates the stability of the haptic system for frequencies up to the Nyquist frequency, i.e.

$$\gamma - \delta^2/4 \leq \pi^2. \quad (4.15)$$

With this condition and with the possible parameter range for the physical damping $\delta \in [0, 0.02]$, the limit for the physical stiffness results as $\gamma \leq [\pi^2, \pi^2 + 0.0001]$. With previous assumption of a sampling frequency of at least 1 kHz, this limit is nearly 10,000 times greater than the maximum stiffness of a human arm defined in (3.17). Such high stiffness causes the stability boundaries to completely change their shape and size.

Example 4.1. *To reach Nyquist frequency for an exemplary haptic device with parameters similar to the PHANToM haptic device [16], $m = 0.1$ kg and $T = 0.001$ s, a physical stiffness of*

$$k = \pi^2 m/T^2 + b^2/4m \approx 987,000 \text{ N/m} \quad (4.16)$$

would be necessary, without considering mass of the human arm. Due to the square of the sampling period T in the denominator of the first summand, this stiffness value is only marginally influenced by the physical damping b . \square

Figure 4.5 shows the stability boundaries for 41 evenly distributed values of γ between 0 and its maximum value $\pi^2 + \delta^2/4$, at which the Nyquist frequency is reached. This figure contains a row with three plots for each delay factor $d \in \{0, 0.5, 1, 2, 4, 8\}$. In each of these rows, the first plot on the left shows the overall shape of the stability boundaries for $\delta = 0.02$. Since the influence of the physical damping in its valid parameter range $\delta \in [0, 0.02]$ is hardly visible in this scale, the overall shape the stability boundaries for $\delta = 0$ is not shown explicitly.

The second ($\delta = 0.02$) and the third ($\delta = 0$) plots in the middle and on the right, respectively, show close-up views around the origin. These plots reveal that there is an intersecting stable region for $\delta > 0$, which vanishes for $\delta = 0$ in the point of origin. Inside this intersecting region, the haptic system is robustly stable against the physical stiffness γ . In other words, a physical spring can never destabilize a haptic system, which is rendering a virtual wall with parameter values inside this intersection, independent of the spring stiffness.

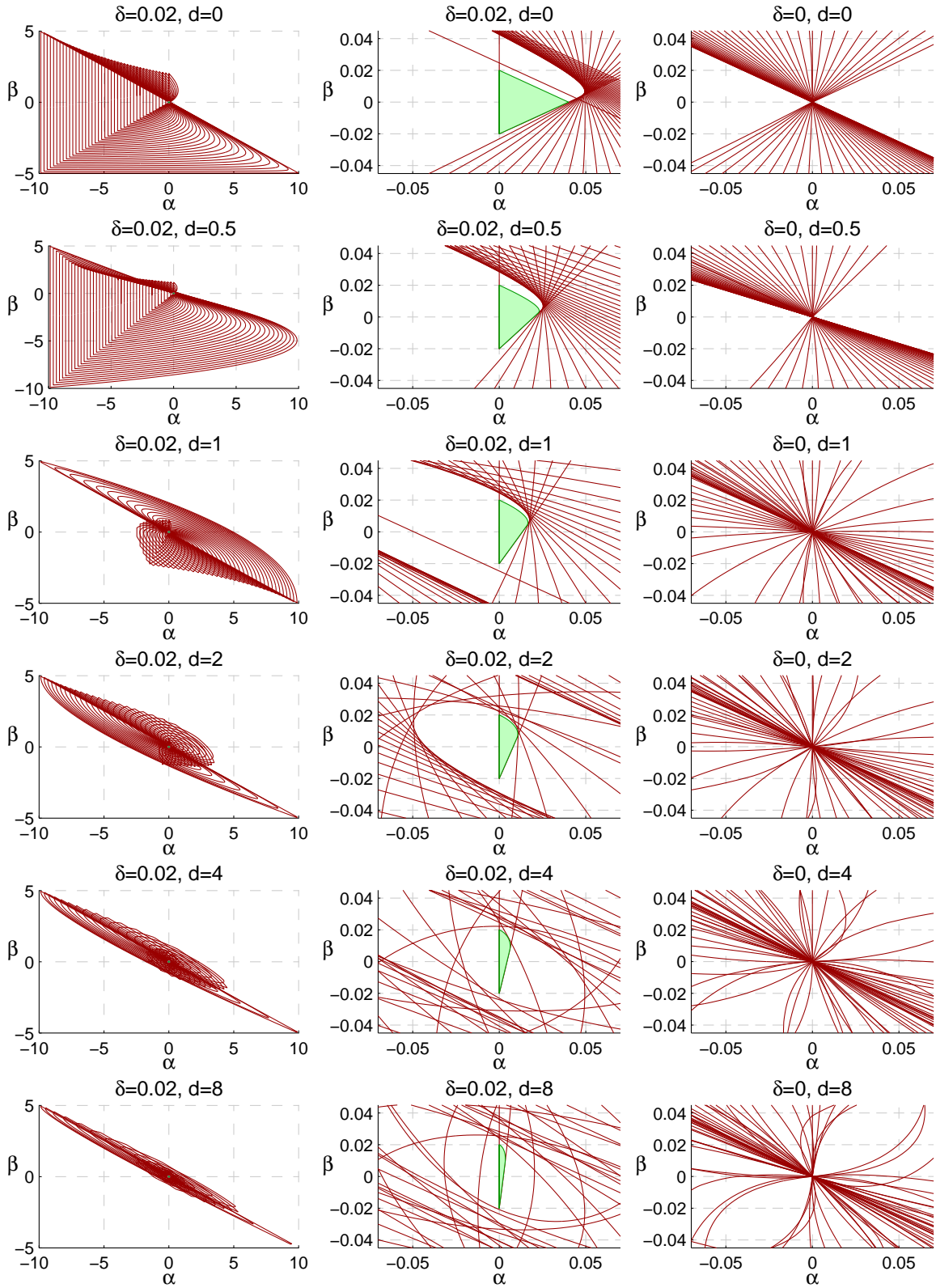


Figure 4.5: The stability boundaries $\delta = 0.02$ and for parameter values of γ such that the system is reaching Nyquist frequency ($0 \leq \gamma \leq \pi^2 + \delta^2/4$). Close-up views are shown in the center and right plots for $\delta = 0.02$ and respectively $\delta = 0$. The passive region is part of the robust stable region.

Due to the definition of passivity, stating that energy can never be extracted from a system, the passive region must be part of the robustly stable region. To confirm this relation, the second plot also shows the passive region as green shaded area. It can be seen that the passive region is located completely inside the robustly stable region independent of time delay and physical damping. Similar to the passive region, also the robustly stable region shrinks with increasing delay, and grows with increasing physical damping.

For $\delta = 0$, the whole stable region is limit stable at the Nyquist frequency $\gamma = \pi^2$, as the system has a pole at $z = -1$ independent of time delay d . For positive physical damping $\delta > 0$, this pole moves inside the unit circle.

Remark 4.1. *Colgate and Schenkel used different dimensionless parameters in [24] (e.g. $\tau \hat{=} 1/\delta$). Their results for — what they call — uncoupled stability correspond to the stable regions for $\gamma = 0$, $\delta = 0$ and $d = 0$ of the present thesis. Yet, the resulting boundaries for their spring stability, which is denoted in this thesis as robust stability, are different. This difference becomes obvious when comparing their curves for $\tau = 1$ to the robustly stable regions for $\delta = 1$ (see [56]), for which their spring stable regions are clearly larger than the robustly stable ones. The reasons for this mismatch are a matter of speculation because Colgate and Schenkel do not specify the transfer function they used for calculating their stability curves.*

4.4 Discussion

The present chapter derived the passivity boundaries for the considered haptic system. The analytical formulation of these boundaries unveils basic relations between the involved physical parameters and the passive regions. These relations allow for drawing the passivity boundaries in a normalized dimensionless parameter plane different to that of stability. The passive region is proportionally scaling with physical damping, whereas the dynamic mass and the physical stiffness have no influence on passivity. The lower parts of the passivity boundaries are straight lines. These linear parts coincide with the linear approximation of the stability boundaries presented in the previous chapter. This is all the more remarkable, since that linear stability condition is partly located outside of the stable region at higher virtual damping and stiffness factors.

It turns out that for realistic parameter values, the passive regions are small sub-regions of the stable regions. However, not only the size of the regions differ, but also the influence of each system parameter is substantially different for passivity than for stability. In detail, time delay affects stability stronger than passivity. A delay of one sampling period decreases the maximum stable virtual stiffness to approximately 22% of the undelayed counterpart, while this ratio is 41% for passivity.

While physical stiffness does not influence the passivity boundaries, it marginally affects stability inside its admissible parameter range. If the stiffness is increased far beyond its admissible range, however, its influence on stability becomes considerable and the stable regions drastically change their appearance. It turns out that inside

a certain subregion of the stable region, the haptic system is stable for any physical stiffness. This robustly stable region completely contains the passive region, although both regions have quite similar shapes. This comparison of stability to passivity leads to a clear explanation for why passivity is conservative for haptic systems in terms of stability: Passivity considers a wide range of physical stiffness values, up to a stiffness that causes the system oscillating in frequencies close to the Nyquist frequency. Such high stiffness values are up to 10,000 times greater than the maximally reachable stiffness of human arms.

The comparison of stability to passivity also shows that the passive regions are independent from the dynamic mass m , whereas the stable regions are linearly scaling with it. A descriptive explanation for this difference may be given by considering the oscillation frequency. The mass influences the dynamics of the system, and hence its oscillation frequency. As the passivity condition holds for any virtual environment, and therefore for any arbitrary oscillation frequency, it is independent of the mass. On the other hand, stability highly depends on the mass because it considers a certain set of parameter values resulting in a certain oscillation frequency.

To summarize, passivity, which is often employed to achieve stable haptic systems, has a main drawback for being used in the context of haptic rendering: Passivity is drastically conservative with respect to stability. In addition, as the passive regions are linearly scaling with physical damping, passivity requires for high physical viscous damping to render stiff passive walls. In practice, however, it is challenging to achieve high physical damping as it usually involves large and heavy hardware with relatively slow dynamics [39]. Therefore, using the passivity approach of time-invariant systems is only of limited suitability for designing stable haptic systems. The next chapter investigates various design criteria for optimizing haptic system performance.

The goal of control law design for haptic displays is to provide a safe and stable user interface while maximizing the operator's sense of kinesthetic immersion in a virtual environment.

Adams and Hannaford [8]

5

Control Design

An extensive stability analysis for haptic systems was presented in Chapter 3. This analysis unveiled fundamental parameter dependencies of stability and derived stability boundaries expressed in a normalized parameter plane. For parameter pairs located on the boundaries, limit stable oscillations result. Inside the regions defined by the stability boundaries, the haptic system is absolutely stable. However, stability alone is not sufficient for most real haptic applications. Rather, it is desirable for haptic systems to provide an optimal behavior when rendering forces from a virtual environment.

But what does *optimal* mean with regard to haptic systems? For the human user, an optimal haptic system would generate haptic feedback that creates the perfect illusion of an interaction with the real world. It would be able to recreate arbitrary force patterns, from contactless movements of the user's hand, over sliding along textured surfaces, to contacts with extremely rigid materials. This chapter analyzes the theoretical limitations in optimally controlling the considered linear system by investigating various optimization criteria.

There is only very limited literature on optimal control in the field of haptics (see also Chapter 2). A prominent example is the work of Colgate and Brown [21], who suggested to consider as a performance measure of haptic systems the size of the stable and passive regions, the so-called *Z-width*. The influence of the system parameters on this size was already comprehensively investigated in the previous two chapters. Although the Z-width is valuable to qualify the possible dynamic range of impedances of a haptic system, it cannot assess the actual dynamic performance of the system. Hence, motivated by classical optimal control theory [34, 85], three basic objectives for an optimal haptic system behavior are postulated:

1. *minimize settling time*, such that oscillations to which the human skin is very sensitive decline quickly,
2. *minimize overshoot*, to minimize wall penetration and hence support the realistic impression of stiff virtual walls, and
3. *increase energy dissipation*, to increase robustness against disturbances and to deal with both above-mentioned objectives simultaneously.

The present chapter introduces optimal regions, paths, and points inside the stable regions that yield in optimal system behavior regarding these objectives. It is based on my previous work [50] and [54], and enhances this approach with respect to impulse based optimization criteria and the influence of delay on the optimal points. All results are given in normalized parameters and can be transformed into their non-normalized counterparts by the rules specified in Table 3.1, e.g., for the virtual stiffness and damping of an optimal point, it holds

$$\begin{aligned} K_{\text{opt}} &= \alpha_{\text{opt}} \cdot m/T^2 \\ B_{\text{opt}} &= \beta_{\text{opt}} \cdot m/T. \end{aligned} \tag{5.1}$$

Due to this parameter normalization, the results hold for arbitrary mass m and sampling time T . The resulting numerical values of the optimal points are listed in Appendix C.

Sect. 5.1 investigates pole-based optimization criteria, focusing on minimal settling time and on maximal damping to minimize overshoot. In Sect. 5.2, criteria based on the system response are systematically analyzed to optimize for settling time, overshoot, and fast energy dissipation. Sect. 5.3 compares these results to optimal continuous-time spring-damper systems and discusses the validity of continuous-time control design for discrete-time systems. The influence of time delay on the optimal points and their costs are investigated in Sect. 5.4. Finally, Sect. 5.5 concludes this chapter.

5.1 Pole-based Design

A standard approach in optimal control is placing the poles of the system transfer function inside specific regions in the plane of the complex parameter [6]. With this approach, the two system properties of settling time T_{settle} and system damping ζ can be tuned easily. To optimize for settling time, all poles must be placed inside concentric circles with minimum radius $r = |z|_{\text{max}}$ [5]. Similarly, to adjust the system damping, all poles must be placed inside minimal concentric logarithmic spirals [74]. Figure 5.1 illustrates these two different pole regions.

Two basic design objectives postulated in the introduction of this chapter are to minimize settling time and overshoot. The former means for the pole design to minimize the radius r of the concentric circle in the parameter plane of the complex variable z .

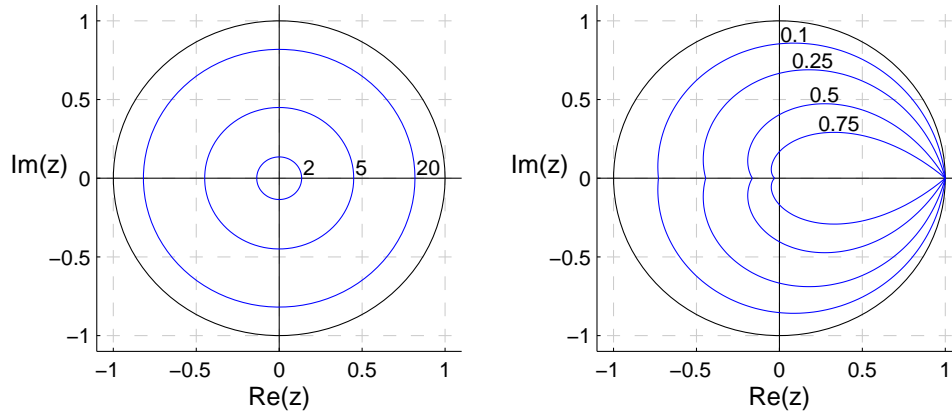


Figure 5.1: Regions for pole-based design criteria are defined by circles around the point of origin (left), and logarithmic spirals (right). The values represent the settling time in number of sampling steps T_{settle}/T (left), and the system damping ζ (right) for the respective pole regions.

The latter objective is achieved by maximizing the system damping ratio ζ , i.e., minimizing the area defined by the logarithmic spirals. Thus, the following cost functions for the two pole-based design criteria are introduced for settling time and damping as

$$C_r := r \quad (5.2)$$

$$C_\zeta := -\zeta. \quad (5.3)$$

This section investigates the two optimization criteria O_r and O_ζ that aim at minimizing the costs C_r and C_ζ of the considered closed-loop transfer function (3.9).

5.1.1 Minimum Settling Time

The settling time of a control system describes the duration of a system response until the steady-state deflection falls and stays below a certain percentage of its initial value (also called the *settling accuracy* [103]). A common practice is to use 2% as percentage threshold value. For this value, the settling time becomes approximately four times the time constant of the slowest (largest) eigenvalue [122], i.e.,

$$T_{\text{settle}} \approx -\frac{4T}{\ln r}, \quad \text{with } r = |z|_{\max}. \quad (5.4)$$

The following lines investigate how the pole-based costs C_r for the settling time behave inside the stable region of the normalized virtual parameters α and β (see Chapter 3). To this end, the stable region is gridded¹ and for each grid point the

¹All grids in this chapter have a resolution of 251 equally distributed grid points for each of the two axes, α and β , inside the bounding box of the stable region.

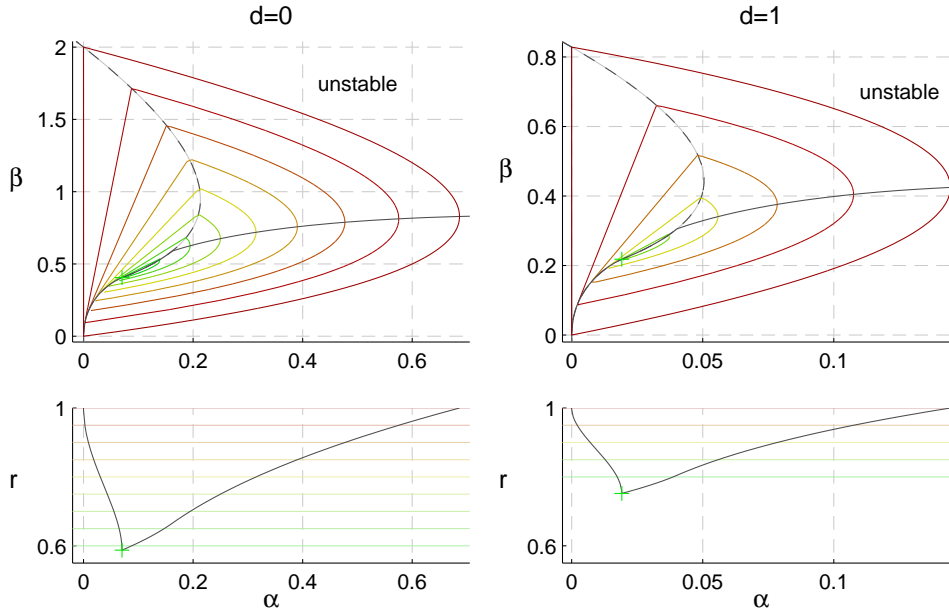


Figure 5.2: The optimal curves for the minimum settling time criterion O_r for $d = 0$ (left) and $d = 1$ (right). Contour lines in the upper subfigures illustrate how the costs are changing inside the stable region. The lower subfigures show the radius r along the optimal curves.

costs C_r are calculated using the closed-loop transfer function (3.9). This procedure results in a three-dimensional cost map that is visualized for practical purpose by contour lines of constant costs in the upper two plots of Fig. 5.2 exemplarily for physical stiffness $\gamma = 0$, physical damping $\delta = 0$, and delay factor $d \in \{0, 1\}$ (the picture on the front page of this thesis shows this map as three-dimensional surface for $d = 0$). Between two contour lines, the radius r and therefore also the costs C_r differ by 0.05. The cost distribution map has an absolute minimum value, which is marked by a green plus in Fig. 5.2.

For each virtual stiffness α inside the stable region, there is a corresponding optimal damping value β , resulting in the black solid curve in Fig. 5.2.² And, vice versa, for each virtual damping value β , there is an optimal virtual stiffness α , resulting in the dashed curve. Note, the two optimal curves are identical for a certain range starting at the point of origin until they separate into two different curves. The lower subfigures show the front view on the cost maps and hence illustrate how the costs C_r change when moving along the optimal curve for given α values (the solid curve). The optimum point on this curve corresponds to the absolute optimum point inside the stable region, which is marked again by a green plus.

The Tables C.1–C.3 in Appendix C of this thesis contain the numerical values of

²Similar to the algorithm for the stability boundaries Sect. 3.4, the thresholds for determining the optimal curves were $10^{-8}/(d + 0.5)^2$ for α and $10^{-8}/(d + 0.5)$ for β .

the optimal points for $d \in \{0, 1, 2\}$, $\gamma \in \{0, 0.001\}$ and $\delta \in \{0, 0.02\}$. They also include the numerical values of the rightmost points of the stable regions, i.e., the (α, β) value pairs for which the maximum stable stiffness α_{\max} can be achieved. Note, that the optimal curve, which starts at $(\alpha, \beta) = (-\gamma, -\delta)$, passes through this point.

The costs in the optimal point marked by the green plus are drastically influenced by delay. A delay of one sampling step $d = 1$ increases the minimally achievable radius r from 0.587 to 0.752. For $d = 2$ the radius further increases to $r = 0.825$. In contrast, the influence of physical stiffness γ and damping δ on the optimal point is small, which matches previous observations for the stability boundaries. Note that Salcudean and Vlaar [99] determined for the case of $d = 1$ the same contour lines as that shown in the upper right plot of Fig. 5.2.

5.1.2 Maximum Damping

The system damping is a qualitative measure for the oscillation behavior of a system. In the discrete-time domain the damping ratio ζ is represented by minimal concentric spirals that comprise all poles (see Fig. 5.1 right), where smaller spirals exhibit higher damping. The damping ratio of a complex discrete-time pole z_p results by inserting the conversion formula from continuous- to discrete-time domain $s_p = \ln(z_p)/T$ into the continuous-time damping formula $\zeta_p = -\Re\{s_p\}/|s_p|$ [34], as

$$\zeta_p = -\Re\{\ln z_p\}/|\ln z_p|. \quad (5.5)$$

The overall system damping ζ is constituted by the pole (or pole pair) with minimum damping ratio

$$\zeta = \min\{\zeta_1, \dots, \zeta_n\}, \quad (5.6)$$

where n is the number of poles. Similar to the previous section, the cost distribution for the system damping is shown in the upper two plots of Fig. 5.3 for $d \in \{0, 1\}$, $\gamma = 0$ and $\delta = 0$. Again, for each stiffness α inside the stable region, a damping factor β can be determined at that the system damping ζ becomes maximum. The result is a path in the (α, β) -plane shown as black solid curve. The lower subfigures show the system damping ζ along this curve. In comparison, the dashed curve is the path of optimal stiffness α for given damping β values. For delays $d \geq 1$, this curve coincides with the left stability boundary.

For $d = 0$, there is a subregion inside the stable region, for which the damping ratio is $\zeta = 1$ and hence the characteristic polynomial $p(z)$ has only real zeros. In other words, inside this subregion the haptic system does not oscillate. For larger delays, this subregion vanishes completely.

While the system damping ζ and the pole-based approximation of the settling time T_{settle} depend only on the poles of the closed-loop transfer function, the following section introduces optimization criteria that take into account the response behavior of the system.

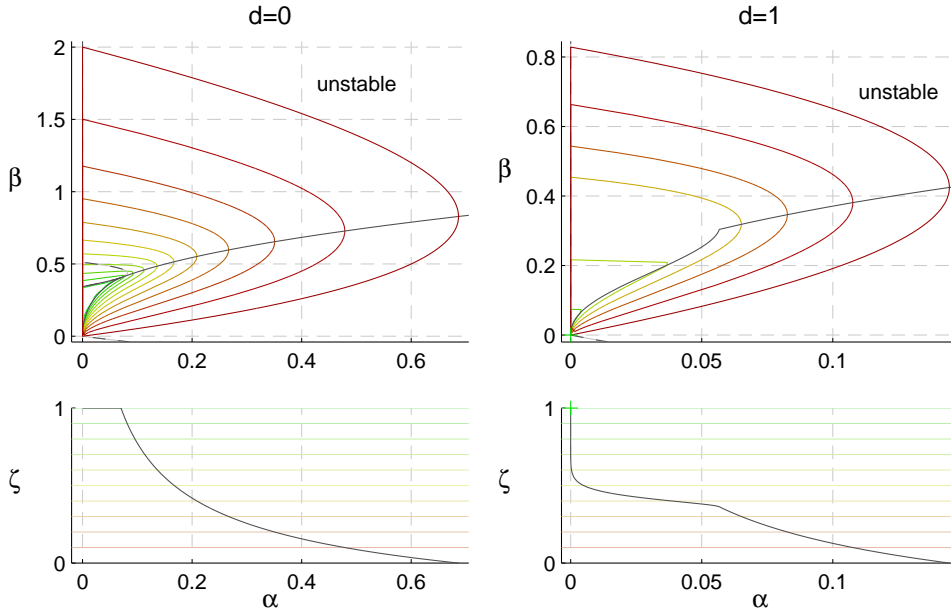


Figure 5.3: Optimal curves and contour lines for the maximum damping criterion O_ζ in analogy to Fig. 5.2.

5.2 Response-based Design

Above optimization criteria aim at placing the system poles of the closed-loop transfer function into specific regions in the complex parameter plane, while the numerator of the transfer function was not taken into account. As the dynamic behavior of a system depends on its whole transfer function, these optimization criteria may not result in optimal parameter sets with respect to the design objectives stated in the chapter introduction. This section discusses various optimization criteria that are based on the transient responses of the considered system.

Depending on the input signal, the response of a dynamical system may change completely. Two input types, the unit step function $u(t)$ and the Dirac impulse³ $\mathfrak{d}(t)$, are most commonly used in control theory to determine the characteristic behavior of a dynamical system. They are both exciting the whole frequency range from minus infinity to plus infinity [65]. In the case of the Dirac impulse, all frequencies are excited with the same amplitude, i.e., the Fourier transform of the Dirac impulse function is $\mathcal{F}(\mathfrak{d}(t)) = 1$. In comparison, the spectrum of the step function is strictly monotonic decreasing with increasing frequencies and has a weighted Dirac peak at $\omega = 0$, i.e., $\mathcal{F}(u(t)) = \pi\mathfrak{d}(\omega) + \frac{1}{j\omega}$. The responses of the system to these two input functions are called the step and the impulse response, $x^{\text{step}}(t)$ and $x^{\text{impulse}}(t)$.

For the investigated haptic system (see Sect. 3.1), there is a physical meaning of each of these two responses that can be expressed by specific initial conditions if the

³The usual symbol for the Dirac impulse δ is already reserved in this thesis for continuous-time damping. Hence, to avoid confusion, the symbol $\mathfrak{d}(t)$ is used for the Dirac impulse instead.

delay and the effect of time-discretization is neglected. To find these meanings, first consider the total energy that can be stored by the system. The investigated system can store energy only in form of kinetic energy in the motion of mass m , and of potential energy in the deviation of the two springs k and K . Thus, the total system energy is given as the sum

$$\begin{aligned} E(t) &= \frac{1}{2} (K + k) (x(t) - x_\infty)^2 + \frac{1}{2} m \dot{x}^2(t) \\ &= \underbrace{\frac{T^2}{2m} (\alpha + \gamma) (\chi(t) - \chi_\infty)^2}_{E_{\text{pot}}(t)} + \underbrace{\frac{T^4}{2m} \dot{\chi}^2(t)}_{E_{\text{kin}}(t)} \end{aligned} \quad (5.7)$$

where $x_\infty = \lim_{t \rightarrow \infty} x(t)$ is the steady-state position. The second line of (5.7) consists of normalized parameters including the scaled position $\chi = x \cdot m/T^2$ (see Sect. 3.2).

The step response of the investigated haptic system describes the movements $x^{\text{step}}(t)$ of the mass m caused by a unit step of the input force $F(t) = F_0 \cdot u(t)$ with $F_0 = 1\text{N}$. This input step introduces energy E_0^{step} into the system and pushes the final position in case of stability to $x_\infty = x(0) + F_0/(K + k)$ (which can be verified using the end value theorem for time-discrete systems [34]). As the system is in its steady-state before the step response takes effect, the mass m is not moving, and the kinetic energy is zero $E_{\text{kin}}(0) = 0$. The initial energy can be expressed purely by the potential energy stored in the two springs.

$$E_0^{\text{step}} = E_{\text{pot}}(0) = \frac{1}{2} (K + k) (x(0) - x_\infty)^2 = \frac{1}{2} \frac{F_0^2}{K + k}. \quad (5.8)$$

Therefore, for the considered haptic system, the step response is equivalent to the case in which the initial velocity is zero $\dot{x}(0) = 0$, and the steady-state position deviates from the current position by $x_\infty - x(0) = F_0/(K + k)$, with $F_0 = 1\text{N}$ for the unit step. In other words, the step response corresponds to a situation in which the haptic device is in steady-state contact with a virtual wall, and then a sudden change of the input force F or of the sum of stiffnesses $K + k$ occurs.

Similarly, also for the impulse response $x^{\text{impulse}}(t)$ a physical meaning exists. The force input in form of a Dirac impulse $F(t) = F_0 \cdot \delta(t)$ causes the mass m to move with velocity $\dot{x}(0 + \epsilon) = p_0/m$ directly after the Dirac takes effect, with momentum $p_0 = F_0 \cdot 1\text{s}$ and ϵ being an arbitrarily small positive quantity in time. In case of stability, the final position equals to the initial steady-state position before the Dirac accelerated the mass $x_\infty = x(0)$. Therefore, the initial energy introduced by the input Dirac impulse can be expressed purely by the kinetic energy of the moving mass directly after the Dirac impulse takes effect,

$$E_0^{\text{impulse}} = E_{\text{kin}}(0 + \epsilon) = \frac{1}{2} m \dot{x}^2(0 + \epsilon) = \frac{p_0^2}{2m}. \quad (5.9)$$

The physically equivalent meaning of the impulse response for $t \geq \epsilon$ corresponds precisely to a haptic device that is colliding with initial velocity $\dot{x}_0 = p_0/m$ against a virtual wall. Based on the impulse and the step response, this section investigates various optimization criteria, comprising minimum settling time O_{settle} , minimum overshoot O_{ov} and maximum energy dissipation O_{Ex} .

5.2.1 Minimum Settling Time

The settling time has already been investigated in Sect. 5.1.1 focusing on the location of the system poles. However, this pole-based design is only an approximation of the real system behavior. The following lines investigate the actual settling time that is based on the step response of the haptic system, and compare it to its pole-based approximation. In accordance to the pole-based design, a 2% position threshold is considered for the response-based settling time T_{settle} , and the cost function is defined as

$$C_{\text{settle}} := T_{\text{settle}}/T. \quad (5.10)$$

Since the 2% threshold is a relative limit, the settling time is the same whether the position x or the scaled position $\chi = x \cdot m/T^2$ (see Sect. 3.2) is considered.

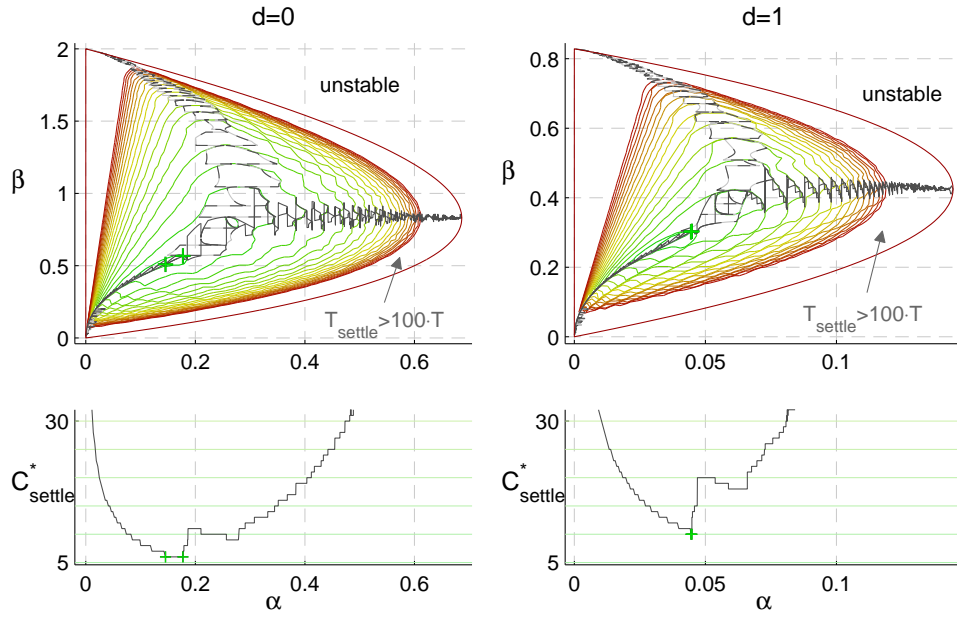
The settling time of the considered haptic system in Fig. 3.1 is determined by the continuous-time position during a step response $x^{\text{step}}(t)$. However, in real haptic systems, the position is measured only at the sampling instants. This means that the costs that can be observed are discrete-time costs $C_{\text{settle}}^* := T_{\text{settle}}^*/T$ that can only take whole non-negative numbers \mathbb{N}_0 .

The discrete-time settling time T_{settle}^* obviously differs from its accurate continuous-time counterpart T_{settle} . Two cases can be distinguished. Firstly, if the physical system settles between two sampling instants, the observed discrete-time settling corresponds to the next integer multiple of the sampling period T , i.e., $T_{\text{settle}}^* = \lceil T_{\text{settle}}/T \rceil T$. Secondly, if the last local extremum of the continuous-time step response that crosses the 2% threshold band falls between two sampling instants, its peak value cannot be correctly detected by the discrete-time analysis. In this case, the observed discrete-time settling time may be drastically shorter than the actual one, $T_{\text{settle}}^* < T_{\text{settle}}$. Consequently, for each parameter pair inside the stable region, it holds in terms of settling time costs that

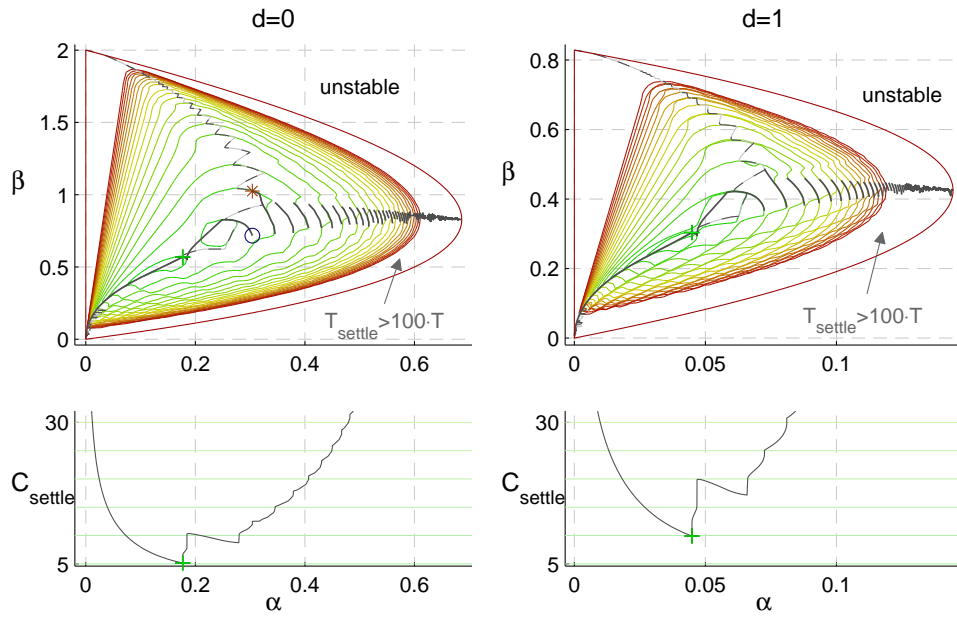
$$C_{\text{settle}}^* \leq \lceil C_{\text{settle}} \rceil. \quad (5.11)$$

This difference is also reflected in the cost maps in Fig. 5.4. The upper subfigure 5.4(a) shows the settling costs for the discrete-time response C_{settle}^* , and the lower one 5.4(b) those for the continuous-time response C_{settle} respectively. The behavior of costs inside the stable region is illustrated again as contour lines, where between two lines, the settling time changes by five sampling periods T in both cases. With the contour lines, also the optimal curves differ between the discrete- and the continuous-time domain.

As the costs for the **discrete-time** signal can only take whole non-negative numbers \mathbb{N}_0 , the optimal lines for the discrete-time case are in fact optimal areas. The



(a) Discrete-time costs C_{settle}^*



(b) Continuous-time costs C_{settle}

Figure 5.4: Cost maps with contour lines and optimal curves for the settling time criterion O_{settle} for $d \in \{0, 1\}$, $\gamma = 0$ and $\delta = 0$. The green pluses indicate the optimal points, whereas the red star and the blue circle in the lower left plot mark the location of the first discontinuity of the optimal curve. The step responses for these points are shown in Fig. 5.5 and Fig. 5.6.

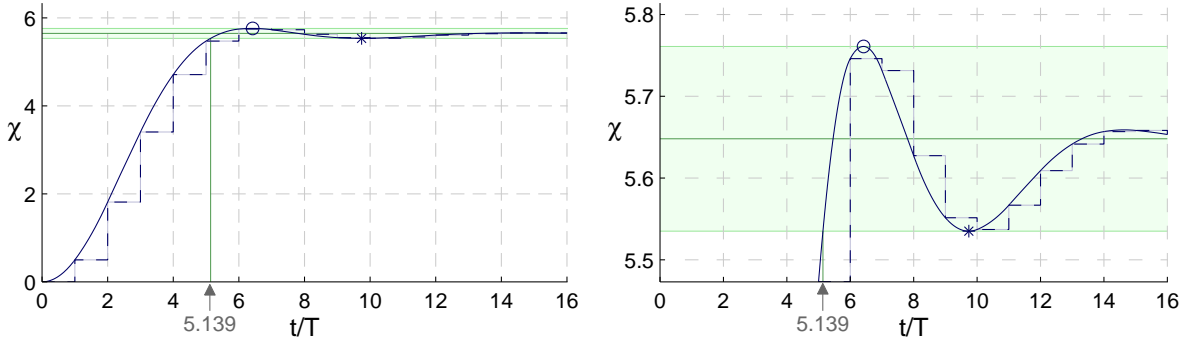


Figure 5.5: The optimal step response with respect to the 2% settling time criterion O_{settle} for $d = 0$ at $\alpha = 0.17705$ and $\beta = 0.56865$. The right plot shows a close-up view around final steady-state position $\chi_{\infty} = 5.648 \text{ ms}^2/\text{kg}$. The points at which the response touches the 2% threshold band are marked by a circle and a star.

limiting curves of these optimal areas are also shown in Fig. 5.4(a). Similarly, the optimal point is not a point in the discrete-time case but an optimal region (the start and end point of these regions are marked by two green pluses). The settling time inside that region is constantly $T_{\text{settle, opt}}^* = 6T$ for $d = 0$, and $T_{\text{settle, opt}}^* = 10T$ for $d = 1$.

The **continuous-time** response describes the actual movements of the haptic device. The settling time costs for this response take real non-negative numbers $\mathbb{R}_{\geq 0}$, as the real system may also settle between two sampling steps. Instead of a region, this continuous-time analysis results in an optimal point that is marked by a green plus. The optimal settling time in this point is $T_{\text{settle, opt}} = 5.139T$ for $d = 0$, and $T_{\text{settle, opt}} = 9.909T$ for $d = 1$, and thus below the values determined by the discrete-time signal. The Tables C.1–C.3 in Appendix C of this thesis contain the numerical values of the corresponding optimal points for $d \in \{0, 1, 2\}$.

The step response in this optimal point for $d = 0$ is shown in the left plot of Fig. 5.5. It also shows the discrete-time position $\chi^{*,\text{step}}$ as dashed line in order to clearly illustrate that, at the sampling instants, the step response of the discrete-time transfer function (3.9) precisely matches those of the continuous-time model. After $T_{\text{settle, opt}} = 5.139T$, the continuous-time position χ stays inside the 2% threshold band. The right plot shows a close-up view around the final steady-state position $x_{\infty} = F_0/(K + k)$, respectively $\chi_{\infty} = F_0/(\alpha + \gamma)$ with $F_0 = 1\text{N}$. This plot reveals that the optimal step response touches the boundary of the 2% threshold band twice after entering it at $T_{\text{settle, opt}}$. First, it touches the upper boundary at its global maximum and then, at a local minimum, the lower one.

In other words, in order to achieve the fastest settling time, the step response has to make use of the whole admissible threshold band. Therefore, if another threshold value is taken into account, another optimal point results which is located significantly beside the above optimum. For example, a 5% threshold value results in an optimal point with an approximately 30% higher stiffness, whereas a 1% threshold yields an approximately 15% lower stiffness (see Appendix C). With the optimal point, also the

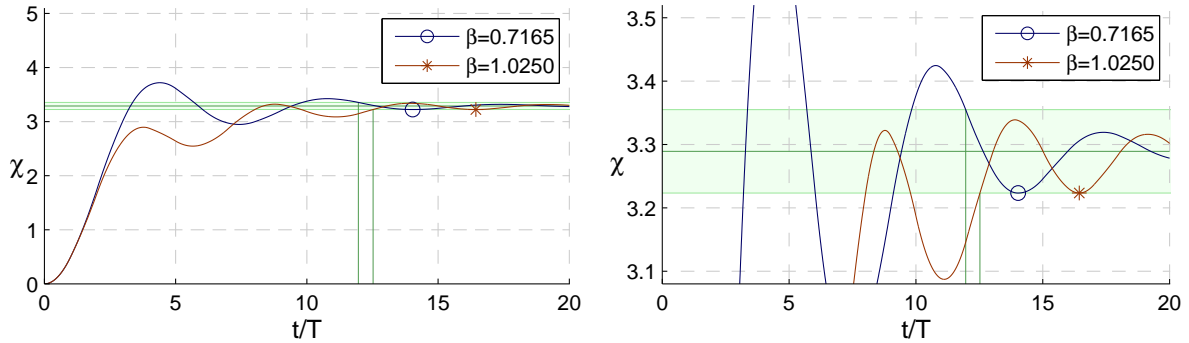


Figure 5.6: Step responses for both sides of the first discontinuity of the optimal curve at $\alpha = 0.30403$ for $d = 0$. The right plot shows a close-up view around final steady-state position $\chi_\infty = 3.289 \text{ ms}^2/\text{kg}$. The touching points with the borders of the 2% threshold band are marked by a blue circle and a red star.

complete cost map in Fig. 5.4 changes with the modified threshold value.

It is interesting to note that the optimal curve for given α values (the black solid curve) of the continuous-time analysis in 5.4(b) becomes discontinuous behind the optimal point, i.e., it has a sawtooth-like shape. But what is the source of these jumps in the optimal curve? Discontinuities in the settling time are already known to occur in linear systems, if a slight modification of the system parameters causes a relative extremum of the transient response to cross the considered threshold band [103, 85]. The same effect is also responsible for the discontinuities of the optimal curve. Figure 5.6 shows the step responses before and after such a jump exemplarily at the first jump at $\alpha = 0.30403$ for $d = 0$. The step response just in front of the jump touches the 2% threshold band at its second local minimum (marked by a blue circle). For a slightly higher virtual stiffness α , this threshold band is already crossed, and cannot be prevented by adapting the damping value β .

Behind the jump, the optimal controller aims at finding an optimal damping value β that shifts this crossing point as much as possible to an earlier point in time. This optimum condition is reached if the next or a later local extremum touches the threshold band (in this case the third local minimum marked by a red star). It turns out that for each point on this optimum curve the step response touches the threshold band at least once after entering it at T_{settle} . However, this only holds true for parts of the optimal curve for given β values (the black dashed curve).

In order to compare the pole-based criterion for minimizing the settling time O_r to its counterpart based on the step response O_{settle} , Fig. 5.7 shows the optimal curves of both criteria in the same parameter planes in the upper plots for $d = 0$ and $d = 1$. The costs of both criteria are compared in the lower plots. To this end, the costs of the pole-based criterion were transformed into settling time using approximation (5.4). The most obvious difference between the two optimal curves is that the response-based curve is discontinuous, whereas the pole-based curve is not.

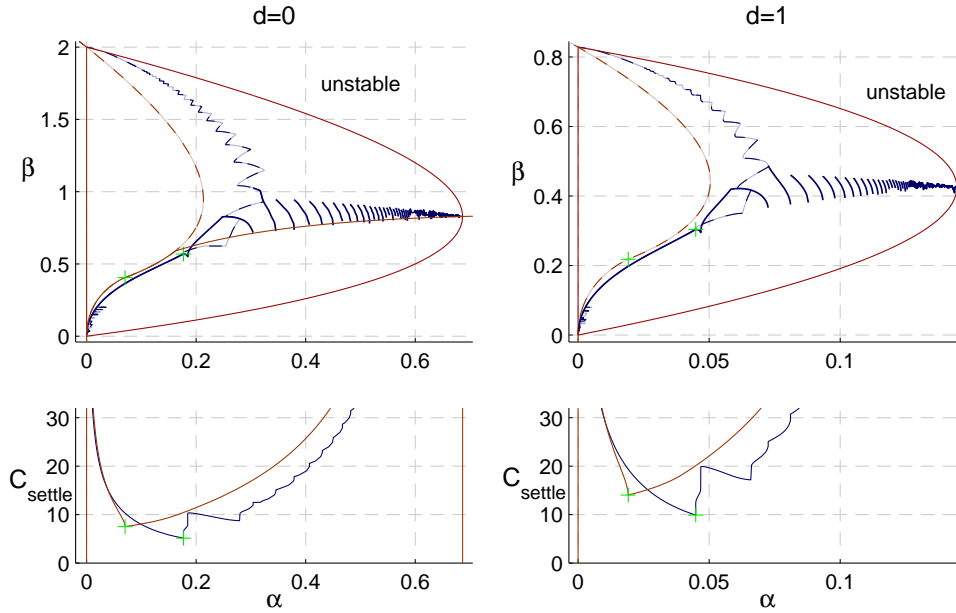


Figure 5.7: Comparison of the optimal curves and cost between the pole-based (red curves) and response-based (blue curves) settling time criterion O_r and O_{settle} respectively.

But also the optimal points for the two criteria differ significantly. In detail, the pole-based criterion for $d = 0$ has a virtual stiffness α , which is only around 40% of the actually required stiffness determined by O_{settle} (depending on the parameters γ and δ this number varies between 37% and 42%, see Table C.1). Similarly, the virtual damping β is about 70% of the actual optimal value from O_{settle} . For larger delays, the effect is similar but the influence of the two parameters γ and δ becomes greater (see Tables C.2–C.3).

The practical difference between the optima of the two criteria O_r and O_{settle} becomes evident when their actual settling times are compared. A haptic system that is optimally tuned according to the pole-based criterion O_r has an actual settling time that is more than twice as long as the minimally achievable settling time (e.g., for $d = 0$, $\gamma = 0$, and $\delta = 0$ this difference is $13.7T$ vs. $5.1T$, and $25.8T$ vs. $9.9T$ for $d = 1$).

5.2.2 Minimum Overshoot

Another fundamental control design objective is minimizing the overshoot. The overshoot is defined by the position error between the steady-state and the maximum position of the step response. The cost function is defined as the relative overshoot

$$C_{\text{ov}} := \frac{\max(x(t)) - x_{\infty}}{x_{\infty}} = \frac{\max(\chi(t)) - \chi_{\infty}}{\chi_{\infty}}. \quad (5.12)$$

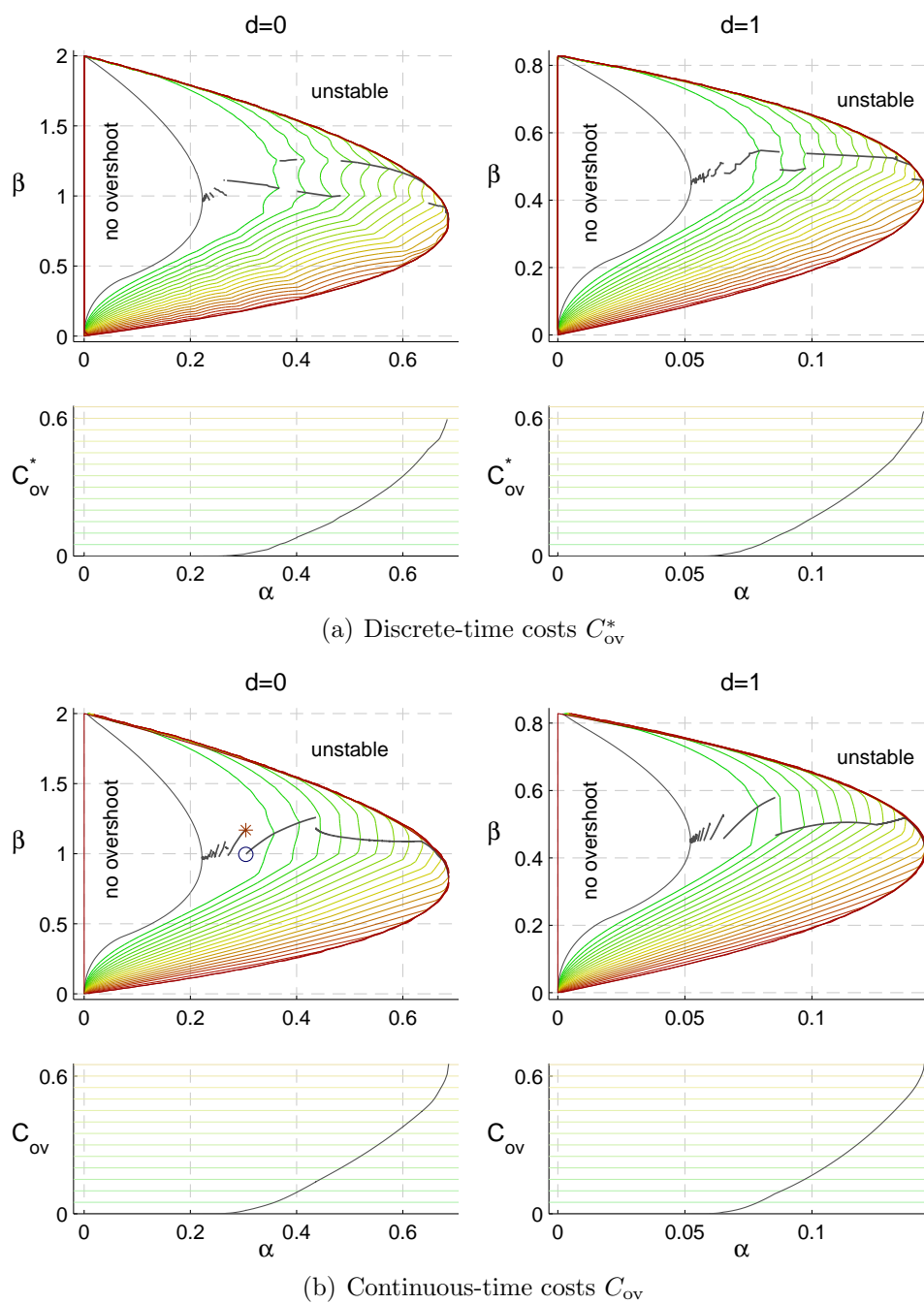


Figure 5.8: Cost maps with contour lines and optimal curves for the overshoot criterion O_{ov} for $d \in \{0, 1\}$, $\gamma = 0$ and $\delta = 0$. The red star and the blue circle in the lower left plot mark the location of the largest discontinuity of the optimal curve. The step responses for these points are shown in Fig. 5.9.

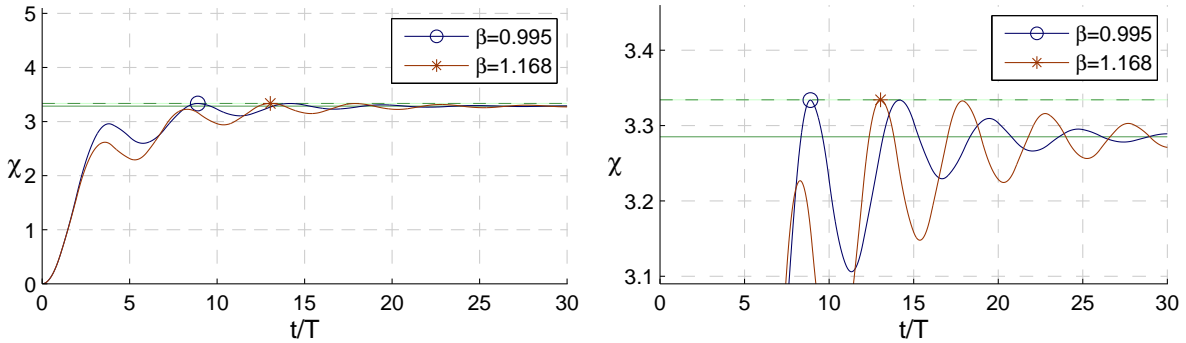


Figure 5.9: Step responses for both sides of the largest discontinuity of the optimal curve of O_{ov} for $d = 0$ at $\alpha = 0.3044$. The right plot shows a close-up view around final steady-state position $\chi_\infty = 3.285 \text{ ms}^2/\text{kg}$. The points at which the responses reach their maxima are marked by a circle and a star.

Figure 5.8 shows the cost maps and the optimal curves for overshoot criterion O_{ov} for $d = 0$ and $d = 1$. Similar to the settling time criterion O_{settle} the cost maps and optimal curves depend on whether the sampled discrete-time position x^* (see Fig. 5.8(a)) or the actual position x (see Fig. 5.8(b)) is considered. The overshoot of the discrete-time position is always less or equal to the actual overshoot $C_{ov}^* \leq C_{ov}$ for each point inside the stable region, although this difference is hardly visible in the cost maps. Despite of this, this difference has a clear effect on the optimal curve.

Figure 5.8 also reveals that in a subregion of the stable region the step response has no overshoot⁴. Outside of that subregion the resulting optimal curve is discontinuous. The numerical values for the point with no overshoot and maximum virtual stiffness α (i.e., the rightmost point of the subregion with no overshoot) are listed in the Tables C.1–C.3 in Appendix C. It is interesting to note that the boundary of the region with no overshoot has a quite similar shape as the optimal curve for given β from the optimization criterion O_r , although the latter is actually located completely inside the region with no overshoot.

In order to investigate the origin of the discontinuities of the optimal curves, Fig. 5.9 exemplarily shows the step responses before and behind the largest jump for the continuous-time case at $\alpha = 0.3044$. On both sides, the responses have the same relative overshoot of $C_{ov} = 1.48\%$ illustrated as dashed green horizontal line, although different local maxima define the overshoot. For $\beta = 0.995$, the second and third local maximum of the step response touch the dashed green line, whereas for $\beta = 1.168$ only the third one does. In fact, step responses with two global maxima occur over large parts of the optimal curve, but not on the whole curve.

⁴Due to numerical errors, the performed simulations only verified an overshoot of less than $C_{ov} \leq 10^{-12}$ inside the region without overshoot. As this value is usually smaller than the sensor resolution of real haptic systems, the error is of no practical relevance.

5.2.3 Minimal System Energy

The above optimization criteria are under the most basic and fundamental control design methods. Their analysis provides fundamental insights in the relation of the model parameters and the system behavior. However, their optimal solutions do not guarantee a good overall system design, as they consider only one single aspect each [109]. For example, a decrease in the settling time often leads to a larger overshoot.

In order to resolve this conflict between the various optimization criteria, the literature suggests another group of criteria that take into account the error of the transient response and the time when this error occurs [40]. As the considered haptic system has the advantageous property that the energy $E(t)$ can be approximated at any time, this section introduces a related set of optimization criteria. These criteria are also based on the transient response but aiming at minimizing the time integral of the system energy during a transient response. Minimizing this integral of system energy means that an initial energy $E(0)$ should be dissipated as fast as possible. In order to analytically formulate this design goal, a cost function may be defined as the time-integral of the system energy,

$$C_{E0} := \frac{1}{T \cdot E(0)} \int_0^\infty E(\tau) d\tau. \quad (5.13)$$

This cost function is a quantitative measure for the performance of the system. To obtain cost values that are independent of the two system parameters m and T , the integral is normalized by the initial energy $E(0)$ and the sampling period T , resulting in a dimensionless performance measure. Motivated by time scaling of standard optimization criteria [109], a more general definition of the cost function may be introduced as

$$C_{Ew} := \frac{1}{T^{w+1} \cdot E(0)} \int_0^\infty E(\tau) \tau^w d\tau, \quad (5.14)$$

with the weighting exponent $w \in \mathbb{R}$. The higher the exponent w , the more severely late energy is penalized, resulting in optima with faster energy dissipation.

This section investigates three common cases for the exponent, i.e., $w \in \{0, 1, 2\}$. With the definition of the energy (5.7), which uses the squares of position x and velocity \dot{x} , these cost functions may be considered as energy-based extension of the following three standard performance indices [109]:

- integral of the square of the error (ISE) for $w = 0$,
- integral of time multiplied by the squared error (ITSE) for $w = 1$, and
- integral of squared time multiplied by the squared error (ISTSE) for $w = 2$.

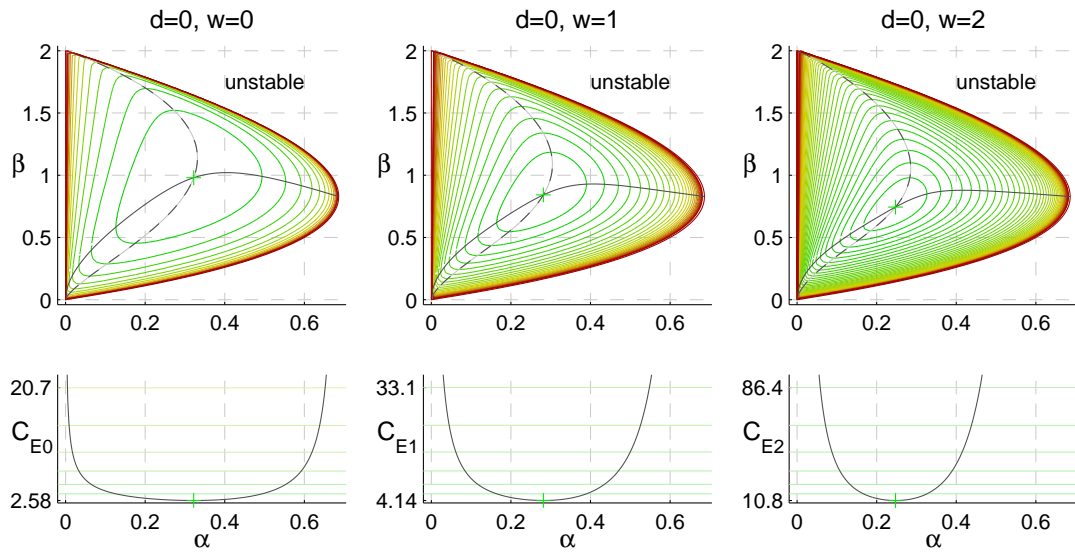
The original definitions of these three cost functions only penalize the squared position error, while definition (5.14) also takes into account the squared velocity. In terms of energy, the former functions only focus on the potential energy, while the considered cost function (5.14) takes into account the total energy, i.e., the sum of potential and kinetic energy.

The cost maps for the three optimization criteria O_{Ew} that aim at minimizing the costs C_{Ew} inside the stable parameter regions can be determined with the same gridding method as used in the previous sections. Depending on the kind of input signal, different cost maps result. Figure 5.10 shows the cost maps for the step response (top) and the impulse response (bottom) for $d = 0$. In these maps the system energy $E(t)$ was approximated as the sum of potential and kinetic energy according to (5.7). The cost distribution inside the stable region is illustrated by contour lines, while a transition over two lines corresponds to a doubling of costs. In accordance to the previous sections, these plots also show the two optimal curves, the one for given α as solid curve, and for given β as dashed curve.

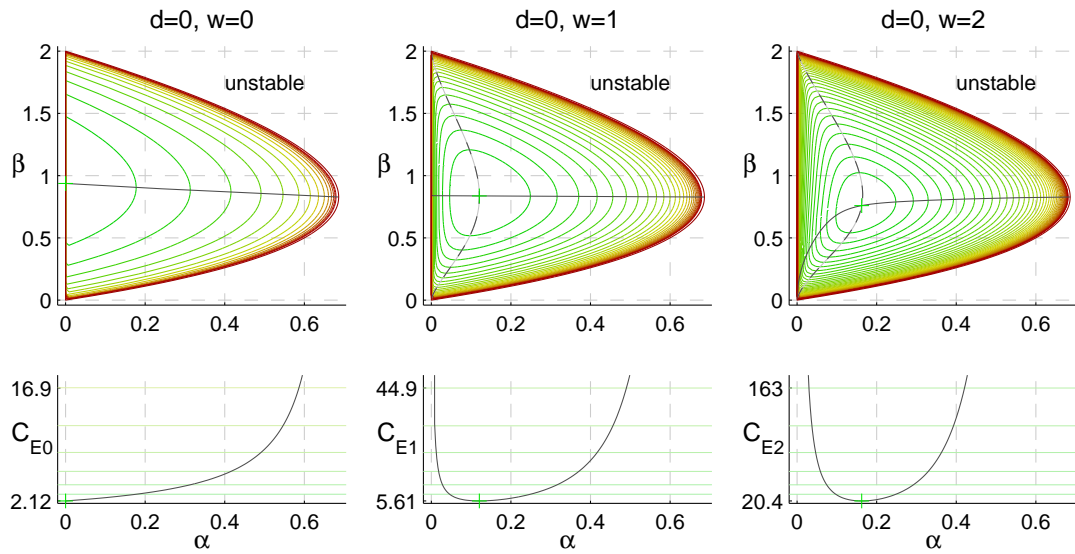
In comparison to the two response-based criteria O_{settle} and O_{ov} , all optimal curves of the energy-based criteria O_{Ew} are continuous, i.e., they do not jump. Note that for O_{E1}^{impulse} , the optimal curve for given α nearly takes the form of a horizontal line; it ranges only between $\beta = [0.828, 0.839]$. In other words, regardless of the stiffness α , the optimal value for virtual damping that minimizes the cost function C_{E1} for the impulse response can be chosen as $\beta \approx 0.83$. Similar but less pronounced, this effect can also be observed for larger delays, i.e., for $d = 1$ the optimal curve varies between $\beta = [0.408, 0.425]$, and for $d = 2$ between $\beta = [0.270, 0.292]$. For the impulse-based criterion O_{E0}^{impulse} , the optimal curve for given β coincides with the left vertical stability boundary $\alpha = -\gamma$, independent of time delay d . This means that on this optimal curve the total stiffness $\alpha + \gamma$ and also the potential energy $E_{\text{pot}}(t)$ are zero. For greater weighting exponents w , this optimal curve is shifted to the right towards higher stiffnesses α .

For each of the considered energy criteria, there is an optimal point inside the stable region marked by a green plus. It coincides with the intersection point of the two optimal curves. The location of these points clearly depends on the cost function as well as on the input signal type. The optimal points of the step response criteria O_{Ew}^{step} have higher stiffnesses α_{opt} than those of the impulse response criteria O_{Ew}^{impulse} . However, their damping values β_{opt} are nearly unaffected by the input signal type, i.e., the step response criteria O_{Ew}^{step} result in very similar damping values compared to the impulse response criteria O_{Ew}^{impulse} . According to the Tables C.1–C.3 in Appendix C, the difference is around 5% for O_{E0}^{step} , 3% for O_{E1}^{step} , and 2% for O_{E2}^{step} . Therefore, also the weighting exponent w has a similar effect on the optimal damping values β_{opt} for both input types. A greater weighting exponent w causes the optimum point to move towards lower damping factors β_{opt} . In comparison, the optimal stiffnesses α_{opt} for the two criteria O_{Ew}^{step} and O_{Ew}^{impulse} are shifted in opposite direction for increasing weighting exponent w .

The shape of the step and impulse responses in the optimal points are shown in Fig. 5.11(a). It can be observed that a greater weighting exponent w results in optimal points with faster settling behavior, which supports above statement that a greater exponent w leads to faster energy dissipation. In addition, for the case of the step response criteria O_{Ew}^{step} , a greater exponent w results in a lower overshoot, but with



(a) Energy criteria based on the step response O_{Ew}^{step}



(b) Energy criteria based on the impulse response O_{Ew}^{impulse}

Figure 5.10: Cost maps with contour lines and optimal curves for the three energy-based criteria O_{Ew} for the step (top) and impulse response (bottom) for $d = 0$, $\gamma = 0$ and $\delta = 0$. The transient responses in the optimal points are shown in Fig. 5.11.

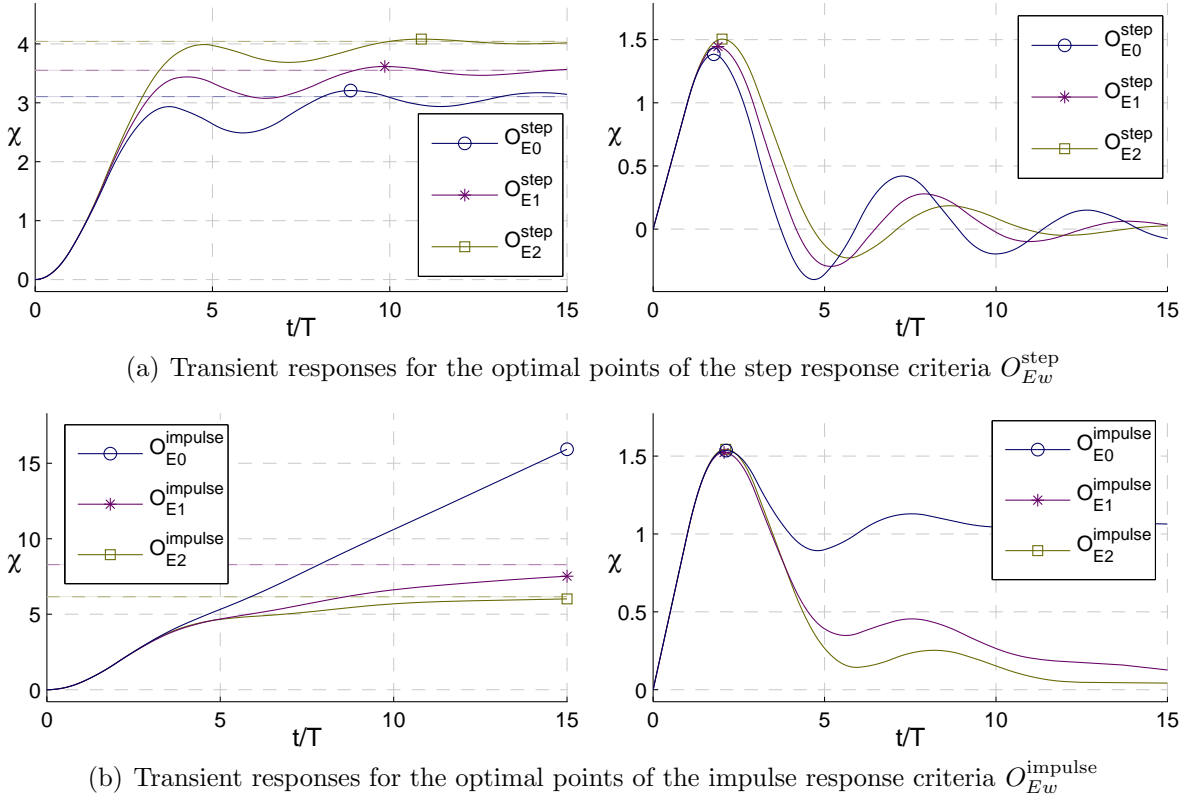


Figure 5.11: Step (left) and impulse responses (right) for the optimal points of Fig. 5.10.

the cost of a lower virtual stiffness α . Interestingly, the step response for the optimal point of O_{E0}^{impulse} is not settling asymptotically stably because this point is located directly on the stability boundary with a total stiffness of $\alpha + \gamma = 0$. The reason that the optimal point of the impulse-based criterion O_{E0}^{impulse} may be located on this stability boundary is twofold. Firstly, the potential energy on the boundary $\alpha + \gamma = 0$ is always zero $E_{\text{pot}}(t) = 0$. Secondly, the input Dirac impulse $\mathfrak{d}(t)$ becomes zero for $t > 0$ and thus the system damping alone is able to completely dissipate the initial system energy $E(0) = E_{\text{kin}}(0)$.

Note that the three cost functions C_{Ew} are based on the continuous-time position signal $\chi(t)$. For the sake of brevity, the cost maps that result for the discrete-time position χ^* are not included in this thesis. They would lead to optima with optimal stiffness factors that are slightly more than 3% higher than the actual optima. However, for higher delays this discrepancy becomes much smaller, such that for $d = 1$ the difference is already less than 1%.

5.3 Relation to Continuous-Time Design Criteria

Up to here, various optimization criteria have been investigated, which all provide valuable information on the properties of the haptic system. In order to find analytical approximations for these optimal curves and to clearly illustrate the detrimental effect of time-discretization and delay, this section investigates a continuous-time second-order system and employs well-known design criteria for critical and optimal system damping.

The analysis of mass-spring-damper systems is part of numerous textbooks on basic control theory, e.g., [1, 75, 107]. Its transfer function is of second order, which is the simplest case for obtaining an oscillating system,

$$H_x(s) = 1/(ms^2 + bs + k) = c\omega_0^2/(s^2 + 2\zeta\omega_0s + \omega_0^2), \quad (5.15)$$

with the damping ratio ζ , the undamped natural angular frequency ω_0 , and the proportional gain c being

$$\zeta = \frac{b}{2\sqrt{km}} \quad \omega_0 = \sqrt{\frac{k}{m}} \quad c = \frac{1}{k}. \quad (5.16)$$

The system is critically damped if $\zeta_{\text{crit}} = 1$, and optimally damped with respect to the amplitude optimum $|H(j\omega)| = 1$ if $\zeta_{\text{opt}} = 1/\sqrt{2}$. If the effect of time discretization and delay is neglected, then the discrete-time spring and damper behave like their continuous-time counterparts. Hence, the continuous-time rules for critical and optimal damping can be easily adapted to the considered system and expressed by normalized parameters, i.e., the system is

$$\begin{aligned} \text{critically damped for } \beta + \delta &= 2\sqrt{\alpha + \gamma} \\ \text{optimally damped for } \beta + \delta &= \sqrt{2(\alpha + \gamma)}. \end{aligned} \quad (5.17)$$

Figure 5.12 visualizes these two conditions as dashed curves and overlays them with the optimal curves of the response-based criteria in three different subfigures, each for $d = 0$ (left) and $d = 1$ (right). In detail, the first subfigure compares these conditions with the optimal curves with respect to minimum overshoot O_{ov} and settling time O_{settle} , the second with those of the step response energy criteria O_{Ew}^{step} , and the third with those of the impulse response energy criteria O_{Ew}^{impulse} .

In the first subfigure 5.12(a), the curve for critical damping (red dashed curve) passes the region of no overshoot and nearly crosses the rightmost point of that region (blue plus). Although the critical damping curve represents the limiting curve with respect to overshoot for a continuous-time second-order system, this is not the case for the considered hybrid system as there are also points without overshoot below that curve. For greater stiffness values α outside of that region, it crosses the optimal curve with minimum overshoot O_{ov} several times. The curve of optimal damping (green

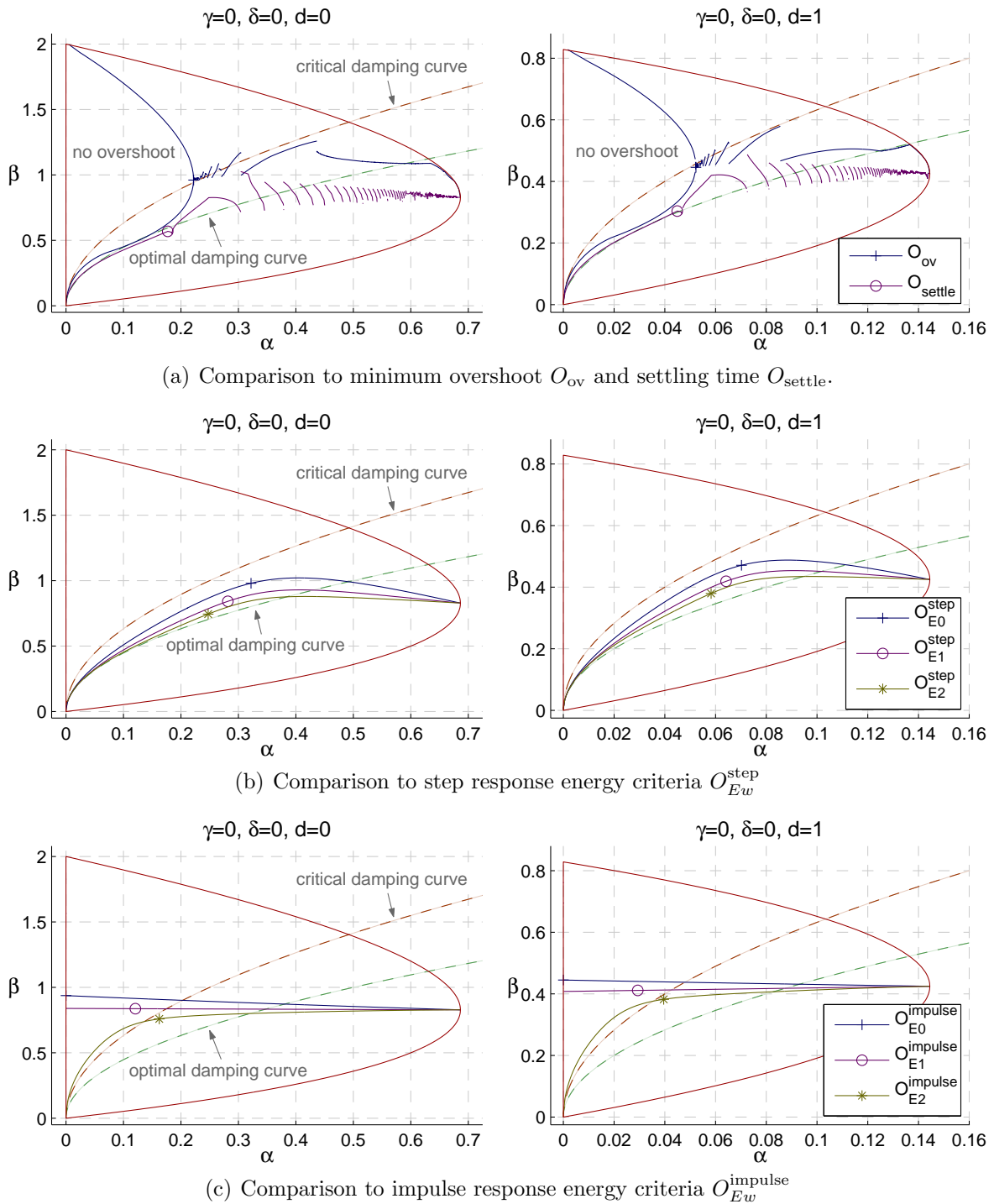


Figure 5.12: Comparison between continuous-time curves for critical and optimal damping as well as the optimal curves of the investigated response-based criteria for $d = 0$ (left) and $d = 1$ (right).

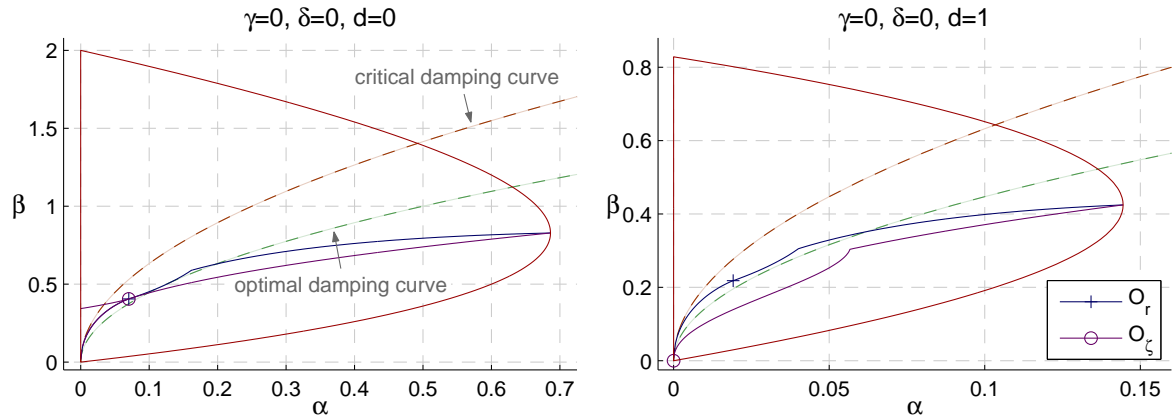


Figure 5.13: Comparison between continuous-time curves for critical and optimal damping and the optimal curves of the two investigated pole-based criteria O_r and O_ζ for $d = 0$ (left) and $d = 1$ (right).

dashed curve) roughly follows the optimal curve with minimum settling time O_{settle} until the optimum point (purple circle). For greater stiffness values α , i.e., on the right hand side of this optimum point, it crosses the optimal curve with minimum settling time O_{settle} several times.

The second subfigure 5.12(b) reveals that the optimal curves of the step response energy criteria O_{Ew}^{step} are located between the two continuous-time conditions, until they cross the optimal damping curve (green dashed curve) far behind the optimal points. For an increasing weighting exponent w , the optimal curves are approaching the optimal damping curve in front of the optimal points. The last subfigure 5.12(c) shows no clear correlation between the two continuous-time conditions and the impulse response energy criteria O_{Ew}^{impulse} . For the sake of completeness, Fig. 5.13 illustrates the curves of the pole-based criteria. This figure shows no clear correlation between the optimal curves and the two continuous-time conditions as well.

To sum up, the **critical damping curve** does not represent the limiting curve with regard to overshoot for the considered haptic system. However, it can be used to avoid overshoot in haptic systems until it crosses the boundary of the region without overshoot, i.e., for $\alpha < 0.22$ ($d = 0$) respectively $\alpha < 0.05$ ($d = 1$). Outside that region and inside the stable region, the critical damping curve may be used as rough approximation for minimizing the overshoot, although with increasing stiffness α it quickly separates from the precise optimal curve of criterion O_{settle} . The **optimal damping curve** can be used as rough approximation for achieving fast settling behavior and fast energy dissipation for the step response as input. The optimal point of each criterion may be taken as a limit until which the approximation can be practically used.

Finally, Fig. 5.14 summarizes all the optimal points of the investigated optimization criteria in one single plot per delay factor. For comparison purposes, it also shows as red plus sign the optimal point that results if the Ziegler-Nichols tuning method [124] based on the critical gain is applied to the considered haptic system (the values are

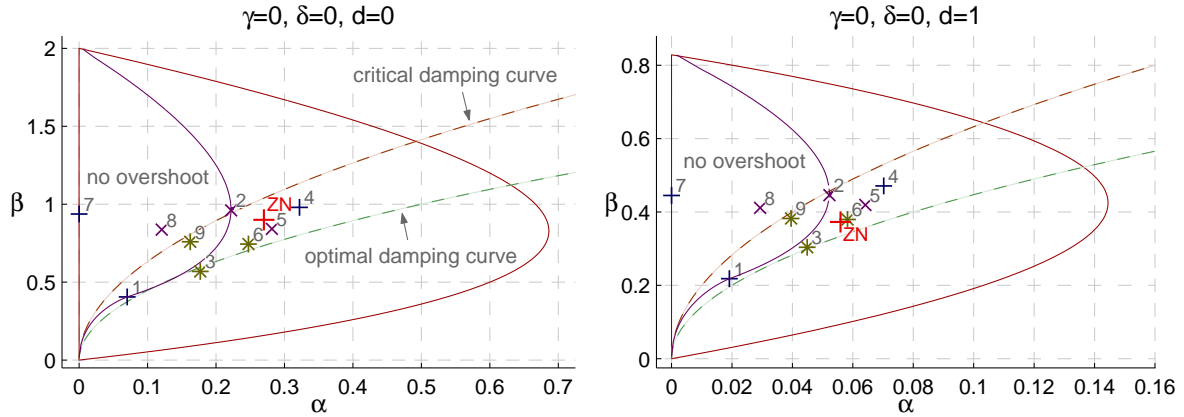


Figure 5.14: Comparison of the optimum points of all investigated optimization criteria (1: O_r , 2: O_{ov} , 3: O_{settle} , 4-6: O_{Ew}^{step} , 7-9: $O_{Ew}^{impulse}$). The red plus sign labeled with ZN shows the Ziegler-Nichols optimum for PI-controllers based on the critical gain.

listed in Appendix C). In this case, the velocity is taken as control variable. It appears that for $d = 0$, this optimum is close to those of the energy criterion O_{E1}^{step} and for $d \geq 1$, close to the optimum of O_{E2}^{step} . Or, to put it another way, depending on the time delay, the Ziegler-Nichols tuning method may be used to optimize haptic systems with regard to one of these two criteria.

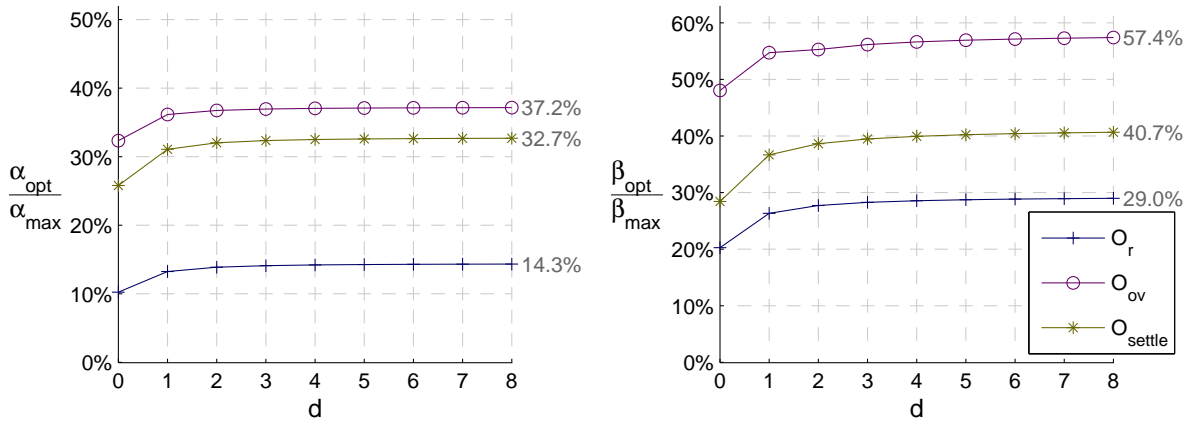
5.4 Influence of Delay

In order to understand how time delay affects the optimal performance of a haptic system, this section investigates the influence of time delay on the location of the optimal points and their costs.

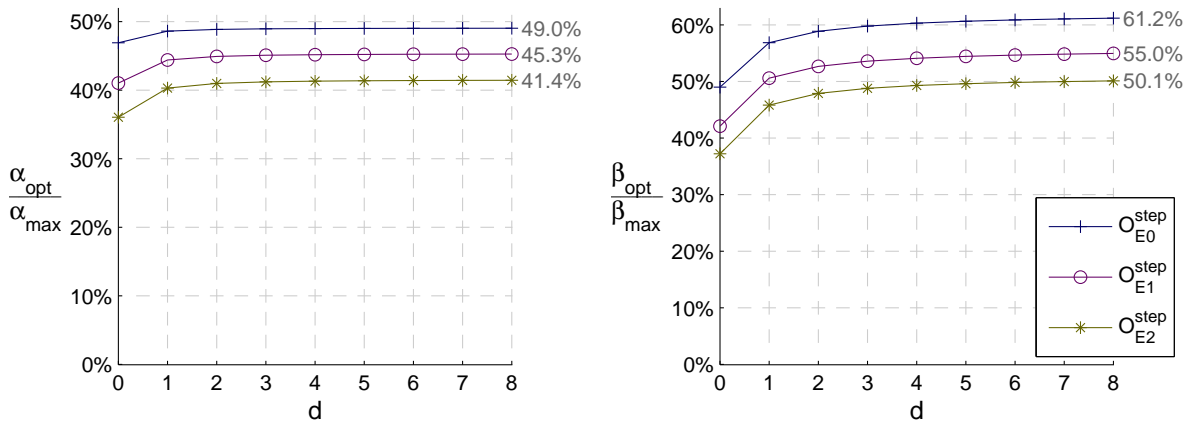
5.4.1 Influence of Delay on the Optimal Parameters

The optimal parameter pairs of the virtual wall are highly affected by delay. As they are always located inside the stable region, they move with increasing delay towards the point of origin in a similar way to the maximum stable stiffness α_{max} and damping β_{max} in Fig. 3.9. To clearly illustrate the difference to these maximum stable values, Fig. 5.15 shows the ratio between optimal and maximal stiffness and damping for each investigated design criterion and for integer delay factors up to $d = 8$. Note, the system damping criterion O_ζ is not considered in this section because its optimum point is not affected by delay and coincides for all delays $d > 0$ with the point of origin.

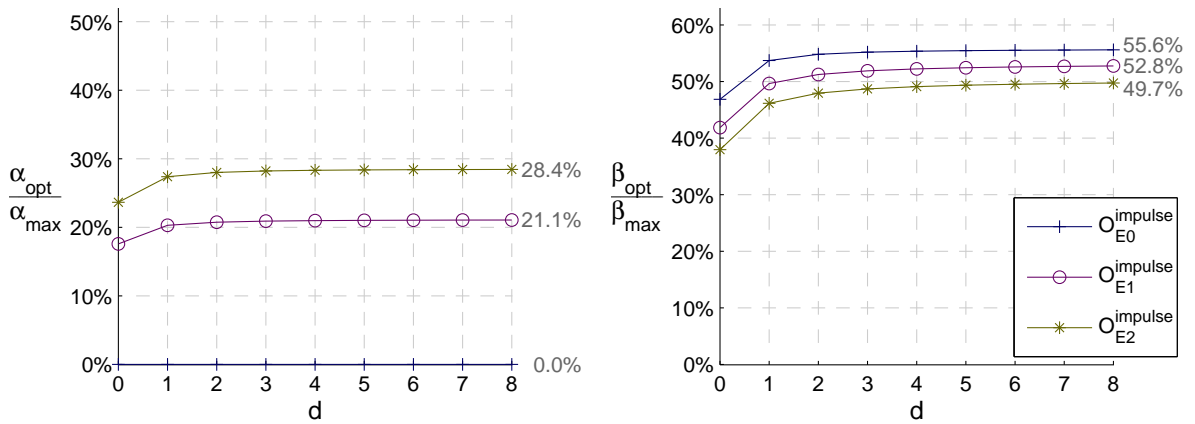
The left plots of this figure show the stiffness ratios $\alpha_{opt}/\alpha_{max}$, while the right plots show the ones of the damping β_{opt}/β_{max} . For each criterion, the ratio seems to converge for increasing delays d towards a constant number (the numerical value of each ratio for $d = 8$ is shown to the right of the curves). The reason for this is the dynamics of the haptic system that becomes slower as the stable region shrinks for larger delays,



(a) Optimization criteria for minimizing the settling time and the overshoot



(b) Energy criteria based on the step response



(c) Energy criteria based on the impulse response

Figure 5.15: Influence of delay d on the ratio between optimal and maximal stiffness (left) and damping (right) for $\gamma = 0$ and $\delta = 0$.

and hence the effect of time-discretization becomes similar to an additional constant delay [34]. It is apparent that the parameter ratios over all criteria never become greater than 49% for the stiffness, respectively 61% for the damping. In other words, to achieve optimal performance, parameter values beyond these ratios should be avoided. Although they exhibit greater numerical virtual stiffness or damping, they worsen the system performance with regard to all considered optimization criteria.

5.4.2 Influence of Delay on the Optimal Costs

After discussing the influence of delay on the location of the optimal points, it is revealing to investigate how delay affects the optimal performance of the system, i.e., the cost in the optimal points. This influence on the optimal costs is shown in the left plots of Fig. 5.16 for $d \in \{0, 1, \dots, 8\}$. The first subfigure investigates the optimization criteria for minimal settling time and overshoot, while the other two show the curves of the energy-based criteria. Therefore, the costs of the pole-based optimization criterion O_r were transformed into settling time using approximation (5.4). The costs of both settling time criteria O_{settle} and O_r seem to increase linearly with delay, yet with a different slope.

The costs of the energy criteria differ vastly depending on the weighting exponent $w \in \{0, 1, 2\}$. In order to directly compare their curves in the same plot, they are normalized by the respective maximal costs, which are for the considered set of delay factors the costs at $d = 8$, i.e.,

$$\eta := \frac{C_{Ew, \text{opt}}(d)}{C_{Ew, \text{opt}}(8)}. \quad (5.18)$$

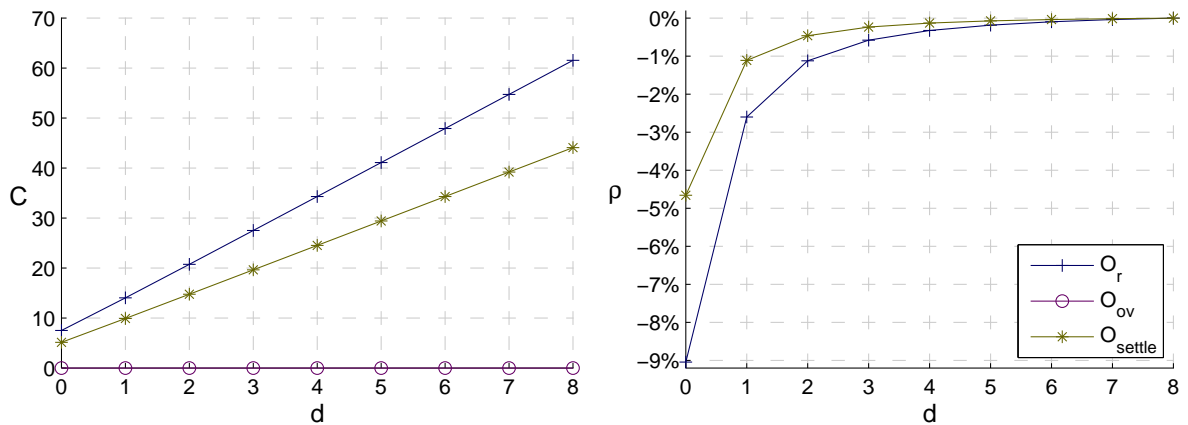
Interestingly, the curves of the impulse- and step-response based energy criteria appear to be almost identical (left plots of Fig. 5.16(b) and 5.16(c)), although the location of their optimal points and their costs are completely different.

For all criteria, the optimal costs seem to follow simple polynomial equations. In particular, similar to the settling time, the optimal costs of the two energy criteria O_{E0}^{step} and O_{E0}^{impulse} seem to increase linearly with delay d . For greater weighting exponents w of the energy criteria, the cost curves take the shape of a parabola (for $w = 1$) and a cubic function (for $w = 2$). To investigate how accurately the costs follow these curves, they are compared to a general polynomial cost approximation function,

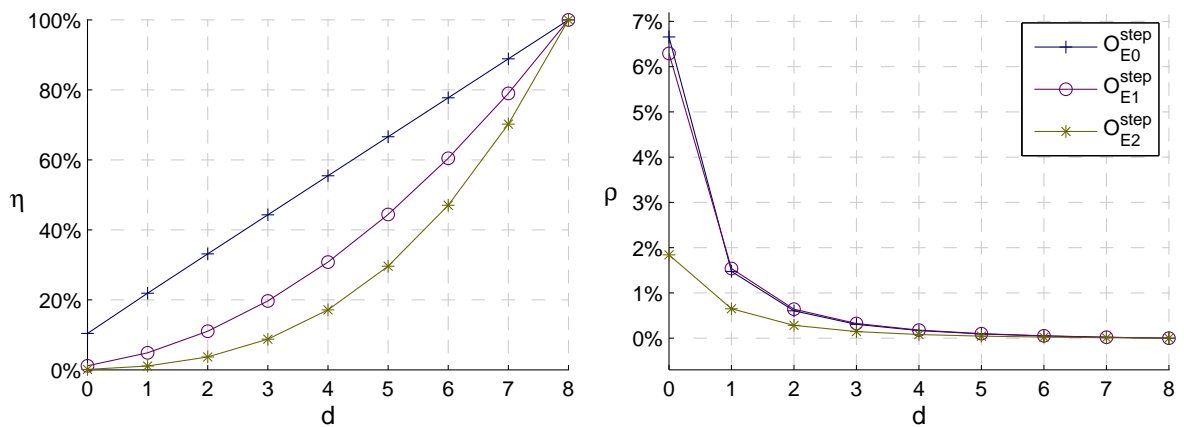
$$\tilde{C}_w(d) := (d + 1)^{w+1} \cdot \tilde{C}_w(0), \quad (5.19)$$

with the scaling factor $\tilde{C}_w(0)$.

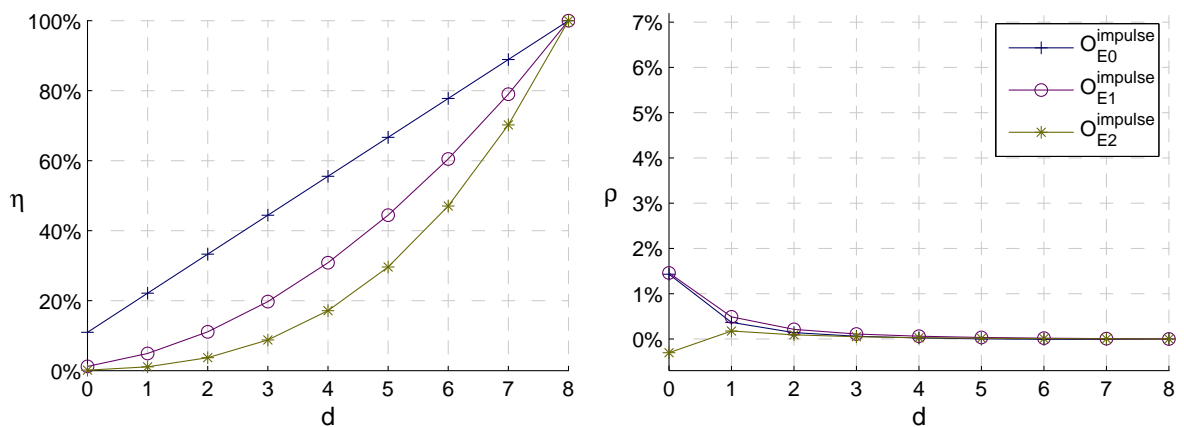
Table 5.1(a) lists the numerical values of the scaling factors $\tilde{C}_w(0)$ of all energy criteria, which have been determined using the respective optimal points at a delay of $d = 8$. It also shows the scaling values for the two settling time criteria O_{settle} and O_r in the column of $w = 0$, as their costs exhibit an approximately linear dependency on delay. The optimal overshoot C_{ov} and system damping C_ζ are both independent of



(a) Optimization criteria for minimizing the settling time and the overshoot



(b) Energy criteria based on the step response



(c) Energy criteria based on the impulse response

Figure 5.16: Influence of delay d on the costs in the optimal points for $\gamma = 0$ and $\delta = 0$ (left), and the relative error ρ of the polynomial cost approximation function (5.19) with respect to these costs (right).

Table 5.1: Scaling factors $\tilde{C}_w(0)$ of the cost approximation function (5.19).

(a) Values resulting for the continuous-time position x resp. χ				(b) Values resulting for the discrete-time position x^* resp. χ^*			
crit. w	$\tilde{C}_w(0)$			crit. w	$\tilde{C}_w^*(0)$		
	0	1	2		0	1	2
O_r	6.84	—	—	O_r	—	—	—
O_{settle}	4.90	—	—	O_{settle}	5.0	—	—
O_{Ew}^{step}	2.75	4.40	11.00	O_{Ew}^{step}	2.81	4.47	11.30
O_{Ew}^{impulse}	2.15	5.69	20.30	O_{Ew}^{impulse}	2.16	5.80	20.71

delay (i.e., $\min(C_{\text{ov}}) = 0$ and $\min(C_{\zeta}) = -1$) and thus not considered here. Note, all values in Table 5.1(a) appear not to change significantly for delays greater than $d = 8$. In particular, it can be checked that between $d = 8$ and $d = 10$, the relative difference is less than 0.02%, i.e., the values only change behind the fractional digits shown in Table 5.1. For the sake of completeness, Table 5.1(b) shows the scaling factors $\tilde{C}_{Ew}^*(0)$ that result for $d = 8$ for the discrete-time position x^* or χ^* . For large delays, they converge towards the values for the continuous-time position in Table 5.1(a). However, their accuracy is lower as these scaling factors are stronger influenced by time delay. Their relative difference between $d = 8$ and $d = 10$ is up to 0.5%.

The right plots in Fig. 5.16 show the relative error between this polynomial equation and the optimal costs

$$\rho := \frac{\tilde{C}_w(d) - C_{\text{opt}}(d)}{C_{\text{opt}}(d)}. \quad (5.20)$$

As the scaling factors $\tilde{C}_w(0)$ were determined at a delay of $d = 8$, the error ρ in Fig. 5.16 vanishes at that delay factor. With decreasing delay, the absolute value of the relative error $|\rho|$ increases until it reaches its maximum at $d = 0$. For all criteria, it stays below $|\rho| < 1.2\%$ for $d \geq 2$. For $d = 1$, the error is limited by $|\rho| \leq 2.6\%$, while for the undelayed case $d = 0$ it reaches 9.1% (for the criterion O_r). This means that the polynomial approximation (5.19) is suited especially for delays of at least one sampling period to predict the optimal performance that a haptic system is theoretically able to achieve.

It is important to recall that the settling time criteria depend on the threshold band width, which was considered to have a width of 2% of the initial steady-state deflection for above analysis. For example, for the criterion O_{settle} , a wider 5% threshold band decreases the factor of the approximation function to $\tilde{C}_w(0) \approx 3.77$, while for a smaller 1% threshold it becomes $\tilde{C}_w(0) \approx 5.81$. Finally, it is interesting to note that the cost approximation function (5.19) becomes zero at $d = -1$. Hence, it may be concluded that in terms of optimal costs, the effect of discrete-time sampling corresponds to a delay of one whole sampling period T .

5.5 Discussion

Stability is a prerequisite for haptic rendering in which computed forces are displayed to a human operator. However, stability alone is not enough to generate effective and convincing haptic feedback. This chapter extensively discussed various design criteria for optimizing the dynamic behavior of the haptic system. These criteria are structured into pole- and response-based optimization criteria. For the response-based optimization criteria, the step and the impulse response were investigated. Both kinds of responses have each a physically equivalent meaning for haptic systems. The impulse response corresponds to a situation in which a haptic device is colliding with an initial velocity against a virtual wall. In comparison, the step response corresponds to a situation in which the haptic device is in steady-state contact with a virtual wall and then a sudden change of input force or stiffness occurs.

An important outcome of the performed analyses is that the stable regions are not flat with respect to all considered cost functions of the design criteria. Rather, for each cost function, the stable region takes a different shape with different optimal curves and with different optimal points that minimize the respective costs. Due to the dimensionless definition of all cost functions and to the normalization of all involved parameters, these results hold for arbitrary masses and sampling rates and hence for all (haptic) systems for which the investigated model can be applied. In addition to these results, this analysis reveals profound insights in the behavior of a haptic system.

1. There is an optimal virtual stiffness with its corresponding damping value for each optimization criterion. Thus, the virtual wall parameters cannot be chosen arbitrarily inside the stable region without highly affecting system behavior. Rather, they have to be carefully tuned by weighing the system behavior and the desired stiffness that, for example, is demanded by a virtual reality simulation.
2. There is a drastic mismatch of pole-based and response-based optimal solutions for minimizing settling time. The optimal parameters denoted by the pole-based approach cause the transient responses to take more than twice as long to settle as the actual minimal settling time. Hence, pole-based criteria appear to be of only limited value when aiming at optimizing the transient behavior of a haptic system.
3. Inside the stable region there is a subregion in which the step response has no overshoot. This subregion covers the whole stable parameter range of virtual damping while roughly only one third of that of the virtual stiffness.
4. The continuous-time design rule for critical system damping ($\zeta_{\text{crit}} = 1$) does not specify the limit with respect to overshoot for discrete-time spring-damper systems. Rather, the resulting curve of critical damping passes through the region with no overshoot and leaves it close to its rightmost point, i.e., the point with maximum virtual stiffness and no overshoot.

5. The continuous-time design rule for optimal system damping ($\zeta_{\text{opt}} = 1/\sqrt{2}$) may be used as rough approximation for achieving optimal step responses with respect to the settling time and the energy dissipation criterion O_{E2}^{step} . However, this only holds true for parameters smaller than the optimal ones.
6. The Ziegler-Nichols tuning rule for PI controllers may be used to determine close to optimal parameters with respect to the step response energy criteria O_{E1}^{step} for $d = 0$, and O_{E2}^{step} for $d \geq 1$. For optimizing the haptic system in terms of other criteria, the Ziegler-Nichols method is not suited.
7. With increasing time delay, the ratio of optimal to maximal virtual stiffness and damping converges to fixed values (Fig. 5.15). This means that then the relative dependency on delay is similar for the optimal and the maximal parameters. The reason for this is that for larger delays the dynamics of the haptic system becomes slower as the stable region shrinks, and hence the effect of time-discretization becomes similar to an additional constant delay [34].
8. The influence of delay on the optimal cost of each considered optimization criterion can be approximated by the polynomial function (5.19). As for some optimization criteria this relation is even linear, it may be formulated as simple rule of thumb. For instance, the rule for the settling time (with a 2% tolerance band) reads according to the respective value in Table 5.1:
Each sampling period of additional time delay causes the optimal settling time to increase by approximately five sampling periods.
9. According to (5.19), the effect of discrete-time sampling corresponds to a delay of one whole sampling period in terms of optimal cost. In comparison, with respect to stability the effect corresponds to only half a sampling period delay (see linear stability condition in Sect. 3.5). Hence, in order to enable a desired performance, the total time period of the sum of all delays plus one whole sampling period is the decisive limiting factor. For example, for the settling time criterion (with a 2% tolerance band), this time period must be less than approximately 20% of the targeted optimal settling time.
10. The optimal performance of a haptic system does not depend on the total dynamic mass m . The mass only linearly scales the optimal values of virtual stiffness and damping. In other words, two haptic devices with different masses but same sampling frequency and delay can theoretically achieve the same optimum costs with regard to all considered cost functions.

The influence of the human arm on the optimal points has not been discussed so far. However, it can be easily checked that it is very similar to its influence on the stability boundaries. The major effect is constituted by the human mass contribution. Due to the normalization rules, the optimal points scale linearly with the total dynamic mass (see also Chapter 3) while their costs remain unaffected.

In comparison, the human stiffness and damping have only marginal influence on the optimal points within their admissible parameter ranges, as shown in Appendix C. However, their relative influence quickly grows for larger delays as the optimal parameters quickly decrease with increasing delay. Interestingly, the optimal costs of all investigated criteria become smaller with increasing physical (continuous-time) stiffness and damping. Hence, if physical stiffness and damping are present, then the polynomial cost approximation function (5.19) may be taken as a worst case estimate for the optimal costs. This insight also supports other control approaches that introduce additional physical damping to improve the system performance of haptic devices, e.g., [39, 78].

Finally, it is revealing to apply the passivity condition of the previous chapter on these optimal points. It can be easily checked that nearly all of them — except the pole-based criterion for minimizing the system damping O_ζ — clearly violate passivity. This finding does not only emphasize the fact that passivity is conservative for stable control of haptic systems, but rather suggests a detrimental property that passivity prevents haptic systems from being controlled in an optimal way. The next chapter will experimentally evaluate the optimal curves and points and discuss the limitations of this approach for real systems.

Experiments are essential in control technology research. A method that has been developed by means of realistic experiments has a larger potential to work in reality compared to methods that have not.

Moberg et al. [82]

6

Experiments

The theoretical approach developed in the previous chapters investigates stability, passivity and optimal control of haptic systems. This chapter presents experiments to support the validity of the theoretical approach but also to reveal the limitations with respect to real systems. Two different devices with widely differing properties are used as experimental platforms: a Novint Falcon and a DLR light-weight robot (LWR). The Falcon is a low-cost desktop device with three active DoF, whereas the LWR has a comparatively much larger workspace and provides all six spatial DoF to the human operator.

This chapter experimentally assesses the theoretical approach on the basis of the transient response-based criteria introduced in the previous chapter. It complements my previous experimental research [31], [37], [49] and [50] by drawing for the first time experimental cost maps inside the stable regions. First, Sect. 6.1 presents the experiments with the Novint Falcon. Then, the experimental study with the LWR is detailed in Sect. 6.2. Finally, the impact of the experiments is discussed in Sect. 6.3.

6.1 Experiments with the Novint Falcon

This section presents the experiments conducted on the Novint Falcon haptic device (see Fig. 6.1). The Falcon is a low-cost desktop device intended for the consumer market [77]. It has a parallel kinematics with three active DoF and is commanded via USB at a sampling rate of 1 kHz. The experiments with the Falcon aim at revealing the influence of the human operator and of modifications in the mounting base on the performance of the haptic system. To this end, stability boundaries and cost distribution maps are experimentally determined for one DoF and compared to the theoretical results.

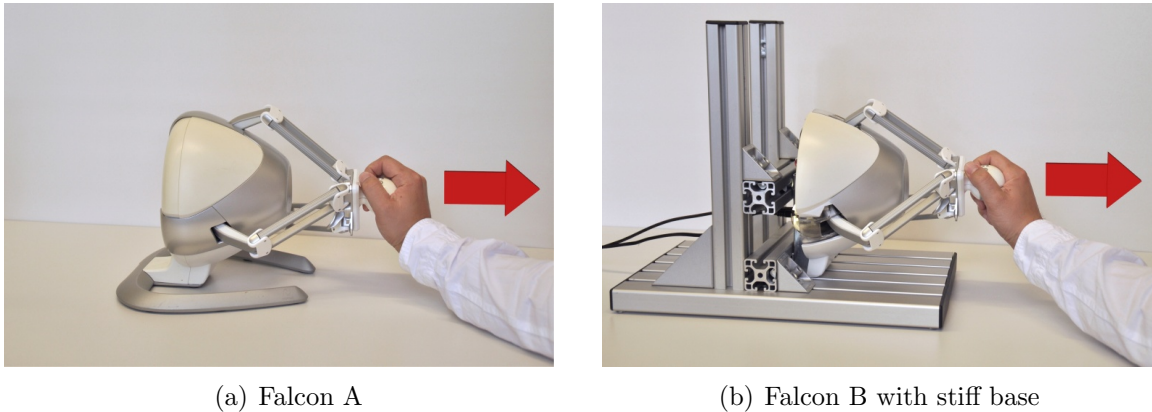


Figure 6.1: The experimental setup with the Novint Falcon. The red arrows show the direction of the input force. On the left photo, a human operator holds the handle of a standard Falcon while on the right one, the base of the Falcon is replaced by a stiff structure.

6.1.1 Experimental Setup and Procedure

A series of seven experiments was conducted as listed in Table 6.1. The first three experiments run on different hardware configurations without a human operator involved. Experiment one and two were conducted on two different Falcon devices (Falcon A and B). For the third experiment, the original base of the second device (Falcon B) was removed and replaced by a more rigid structure built of industrial aluminum profiles (see right photo of Fig. 6.1). This experiment reveals how slight modifications in the hardware influence the experimental results. It is motivated by the findings of Ciáurriz et al. [20], who identified structural elasticity of a haptic device to be the source of vibration modes that may compromise stability. The other four experiments investigate the effect of a human operator. In experiments 4 and 5, the operator held with comfortable grip strength the handle of Falcon A and that of Falcon B with the stiff base, respectively. Similarly, experiments 6 and 7 were conducted on these two devices with high grip strength.

For all seven experiments, a discrete-time spring-damper system with modifiable parameters K and B was acting in the longitudinal direction of the input force as indicated by the red arrows in Fig. 6.1. For each tested parameter pair (K, B) , the device was excited by an input force step of $F_0 = 8\text{ N}$ and the step response was recorded. From these responses, the costs for each investigated criterion were computed offline after the experiments were finished. To obtain the stability boundary, the maximum stable stiffness gains were determined for a predefined set of damping factors. For each damping value B , the stiffness K was increased by a specified step size until the device became unstable. In order to refine the critical stiffness gain and to obtain more precise stability boundaries, the step size of K was decreased to 20% of the original value in a second iteration.

Table 6.1: Numbering of the seven Falcon experiments conducted on three different hardware configurations.

human grip	Falcon A	Falcon B	Falcon B stiff
no operator	1	2	3
comfortable grip	4	–	5
firm grip	6	–	7

For the first three experiments without human operator, the set of damping factors was $B \in \{0, 4, 8, \dots, 184\}$ Ns/m and the initial step size for the stiffness K was 200 N/m. With these values, each course of experiment took around 15 minutes and comprised between 2, 135 and 2, 258 step responses, each for a different parameter pair. To speed up the experiments for the human operator, a coarser resolution was chosen for experiments 4-7. The set of damping factors was $B \in \{0, 10, 20, \dots, 180\}$ Ns/m, and the initial step size for the stiffness was $K = 400$ N/m. Thus, each course of experiment took around four minutes, and comprised between 597 and 682 step responses.

Due to its nonlinear device kinematics [77], the dynamical behavior of the Falcon depends on the position of the handle in its workspace. To obtain similar conditions during each course of experiment, the initial position before each step response was set to

$$x_0 = x_\infty - F_0/K. \quad (6.1)$$

Thus, the steady-state position x_∞ of the spring-damper system was always at the same position in the center of the workspace at $x_\infty = 0.12$ m.

In the other two directions perpendicular to the excited direction of movement, linear virtual springs with stiffness 30 N/m were pushing the handle towards the center of the workspace. Tuning these orthogonal stiffness factors is a tradeoff between accuracy around the desired position in the workspace center and influence on the experimental results. No additional virtual damping was added in these two perpendicular directions because the spring itself was already stable due to intrinsic damping of the device. Moreover, such virtual damping appeared to also affect the excited direction of movement.

6.1.2 System Parameter Estimation

The theoretical stability boundaries and costs depend primarily on the dynamic mass, the time delay and the physical damping involved in the haptic system. In order to compare the experimental to the theoretical results, these three parameters must be estimated first. In comparison, as shown in the previous chapters, the physical stiffness of the human operator has only minor effect on the stability boundaries and the cost distribution inside the stable regions. Hence, this parameter is neglected in the following investigations.

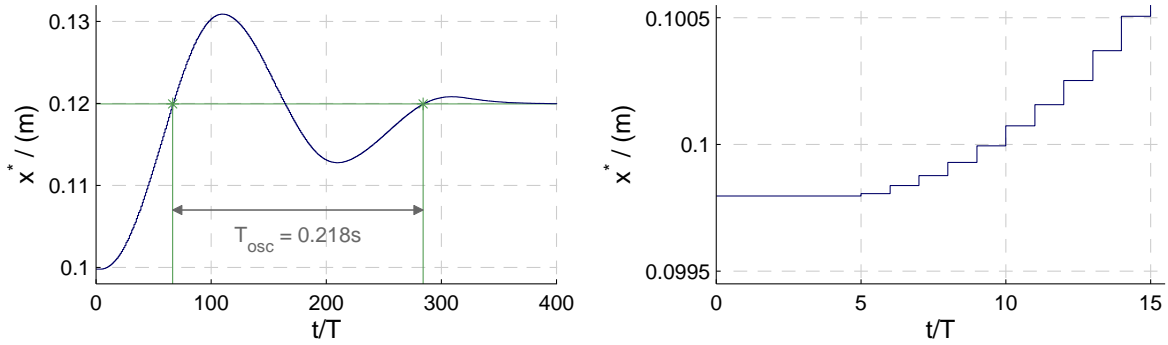


Figure 6.2: The step response for $K = 400 \text{ N/m}$ and $B = 4 \text{ Ns/m}$. The oscillation period is roughly $T_{\text{osc}} = 0.218 \text{ s}$. The right plot shows a close-up view around the starting point. The first position change occurs at $t_{\text{obs}} = 5 \text{ ms}$.

The closed-loop **time delay** t_d highly affects the theoretical stability boundaries and costs (see the previous chapters). Knowing the amount of delay is also required to correctly calculate the experimental costs as the time delay causes a shift between the commanded force and the measured position. The delay can be estimated directly from the step response. If there is no time delay, the first position change of this response can be observed one sampling step after the initial input step takes effect. This is due to the discrete-time property of the virtual environment that detects position changes only at the sampling instants. Hence, the observed total delay factor $d_{\text{obs}} = t_{\text{obs}}/T$, i.e., the number of time periods until the first change of the discrete-time position signal x^* occurs, is the next greater integer multiple of the closed-loop delay factor $d = t_d/T$,

$$d_{\text{obs}} = \lfloor d + 1 \rfloor. \quad (6.2)$$

In other words, the actual closed-loop delay t_d is up to one sampling period smaller than t_{obs} ,

$$t_{\text{obs}} - T \leq t_d < t_{\text{obs}}. \quad (6.3)$$

Figure 6.2 shows exemplarily a measured step response of a Falcon device for $K = 400 \text{ N/m}$ and $B = 4 \text{ Ns/m}$ without a human operator touching the device. The first position change in this step response appears at $t_{\text{obs}} = 5 \text{ ms}$. However, as the Falcon was commanded by a non-realtime computer via USB, the observed delay t_{obs} actually jittered between 4 ms and 6 ms, indicating a closed-loop delay that jittered in the range of $3 \text{ ms} \leq t_d < 6 \text{ ms}$. These results seem to be plausible as also other Falcon users reported delays of up to $t_d = 5 \text{ ms}$ [77].

The continuous-time **viscous damping** b contributes to stability and hence increases the size of the theoretical stable regions and decreases the theoretical optimal costs of all considered optimization criteria (see previous chapters). The viscous damping may be easily estimated using stability condition $b > -B$, which results from the linear stability condition (3.25) when setting the virtual stiffness to $K = 0$. Practically speaking, this condition says that the physical damping b corresponds to the minimal (negative) virtual damping B at which the haptic system is just stable. With this

Table 6.2: Dynamic mass and physical damping of the experiments.

human grip	dynamic mass m		viscous damping b	
	Falcon A&B ^a	Falcon A	Falcon A	Falcon B
no operator	0.58 kg	4 Ns/m	4 Ns/m	2 Ns/m
comfortable grip	0.65 kg	9 Ns/m	9 Ns/m	7 Ns/m
firm grip	1.00 kg	34 Ns/m	34 Ns/m	32 Ns/m

^aThe difference in the inertia of the two Falcon devices was only 0.03 kg and is neglected. Instead, the average inertial values are listed here.

method, a damping of $b = 4 \text{ Ns/m}$ was determined for Falcon A, and $b = 2 \text{ Ns/m}$ for Falcon B. The human arm introduces additional damping, depending on the grip strength. The numerical values obtained are listed in Table 6.2.

The **dynamic mass** m has an effect on the theoretical and on the experimental results. It linearly scales the theoretical stable regions, but it does not affect the theoretical optimal costs. The value of the dynamic mass is also needed in the experimental evaluation to calculate the costs of the energy criteria, as the mass is a parameter of the kinetic energy (see Chapter 5 for the definition of the cost functions).

The mass can be determined in different ways. A pragmatic approach was followed by Martin and Hillier [77], who disassembled a Falcon device and weighed the mass of its structural parts. They obtained values of 0.41 kg for the dynamic mass of the structural parts. In addition, they performed experiments to determine the inertial effects of the motor and obtained a rotational inertia of $1 \cdot 10^{-5} \text{ kg}\cdot\text{m}^2$ per motor and a lever arm of 0.0074 m, corresponding to an inertia of 0.18 kg in the considered direction of movement. For the conducted experiments, the total inertia is approximately the sum of both contributions, which is around 0.95 kg. Unfortunately, no precision of above values was specified in [77].

To check for validity of these values, another approach based on the conservation of linear momentum is applied. This law may be written as

$$m = \int_{t_1}^{t_2} F(\tau) d\tau / (\dot{x}(t_2) - \dot{x}(t_1)). \quad (6.4)$$

With this relation, the inertial masses not only for the Falcon device, but also for the other experiments with the different human grips resulted as listed in Table 6.2. An average delay of $t_d = 5 \text{ ms}$ between the commanded force and the measured position was taken into account. Moreover, only the first 15 ms of each step response were considered, as in that short time the device did not reach high velocities, and thus saturation effects could be neglected. In fact, if longer or later time periods were considered, the determined values of the mass become extremely irregular depending on the velocities reached.

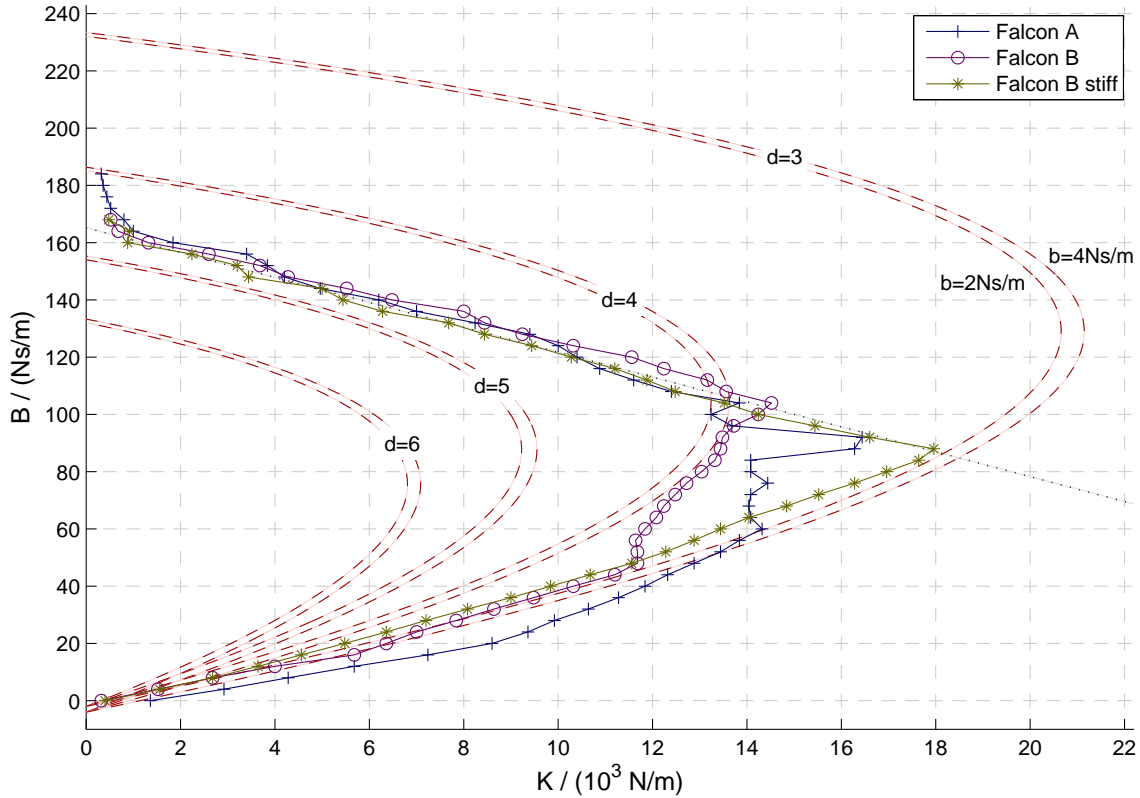


Figure 6.3: Experimental stability boundaries for the first three experiments without a human operator involved (solid). The corresponding theoretical boundaries (dashed) are drawn for $m = 0.58$ kg, $d \in \{3, 4, 5, 6\}$, $k = 0$ N/m, and $b \in \{2, 4\}$ Ns/m.

Comparing the two methods, it appears that their resulting values differ significantly. The real mass is clearly greater than the one determined by the above method (0.95 kg vs. 0.58 kg). The reason is that the acting force does not precisely correspond to the force commanded to the haptic device. It is affected by the actuator dynamics and the device internal motor controllers.

For the further experimental analysis, the masses in Table 6.2 determined by the approach based on the conservation of linear momentum are considered due to two reasons. Firstly, these values are based on the measured and commanded signals that are visible to the controller and that are used for the cost analysis. Secondly, this method yields also values for the dynamic masses of the experiments with a human operator involved.

6.1.3 Stability Boundaries

This section investigates the experimental stability boundaries for all conducted experiments with the Falcon. Figure 6.3 shows the results of the three experiments without human operator involved. It also shows as red dashed curves the theoretical

stability boundaries for the parameter values determined above, i.e., for $m = 0.58$ kg, $d \in \{3, 4, 5, 6\}$, $k = 0$ N/m, and $b \in \{2, 4\}$ Ns/m.

The differences between the three experimental boundaries are quite small. Firstly, the structural modification in the base of Falcon B causes the right part of the stable region (for $K > 11$ kN/m) to grow towards higher stiffness gains, resulting in a triangular-like region with a maximum stable stiffness of roughly $K = 18$ kN/m at a damping of $B = 94$ Ns/m. The rest of the stability boundary remains quite unaffected by stiffening the base. Secondly, the greater physical damping $b = 4$ Ns/m of Falcon A has as effect that the lower part of its stability boundary (for $B < 50$ Ns/m) is located slightly below the two curves of Falcon B, whereas no clear difference is visible in the upper part (for $B > 100$ Ns/m).

Interestingly, this upper part of the boundaries exhibit a quite linear course for all three experiments, which can be roughly approximated by the linear condition (shown as black dotted line in Fig. 6.3)

$$K \leq 38,000 \text{ N/m} - 230 \text{ s}^{-1} \cdot B. \quad (6.5)$$

The literature provides two explanations for the occurrence of such a linear bound: vibration modes of the haptic device [32, 20] and the nonlinear effect of encoder resolution [4, 33]. A deeper investigation of this issue, however, would go beyond the scope of this thesis.

The shown theoretical boundaries clearly differ in size depending primarily on the delay factor d , but also on the physical damping b . The largest theoretical stable region is the one for $d = 3$ and $b = 4$ Ns/m. Compared to the experimental regions, this stable region is clearly larger, and nearly completely contains all three experimental regions – only for Falcon A there are stable parameter pairs located outside of this region (for $B < 50$ Ns/m). On the other side, the theoretical regions for large delays of $d \geq 5$ are so small that they are contained within the experimental regions. Only the theoretical stability boundary for $d = 4$ is crossing the experimental curves. This observation is in line with the results from Dang et al. [27], who found that stability of a system with variable time delay is not constituted by the longest delay observed. Their stability boundaries are rather located somewhere in between the theoretical curves for the shortest and longest delay. In the vicinity of the origin, however, the course of the experimental boundaries rather follow the theoretical boundaries for a delay of $d = 3$. Hence, for small gains that involve relatively slow dynamical movements, the boundaries seems to depend on the smallest delay observed.

Figure 6.4 shows the experimental stability boundaries for the experiments in which the human operator is holding the handle of the Falcon. It appears that the stable regions grow towards higher virtual stiffness with increasing human grip strength. However, this impact is mainly visible in the lower parts of the stable region, i.e., for $B < 70$ Ns/m. In comparison, the upper parts (for $B > 90$ Ns/m) of the experimental curves are only slightly shifted by the human, which holds especially true for the experiment with the Falcon B with the stiff base (Fig. 6.4(b)). Thus, the linear con-

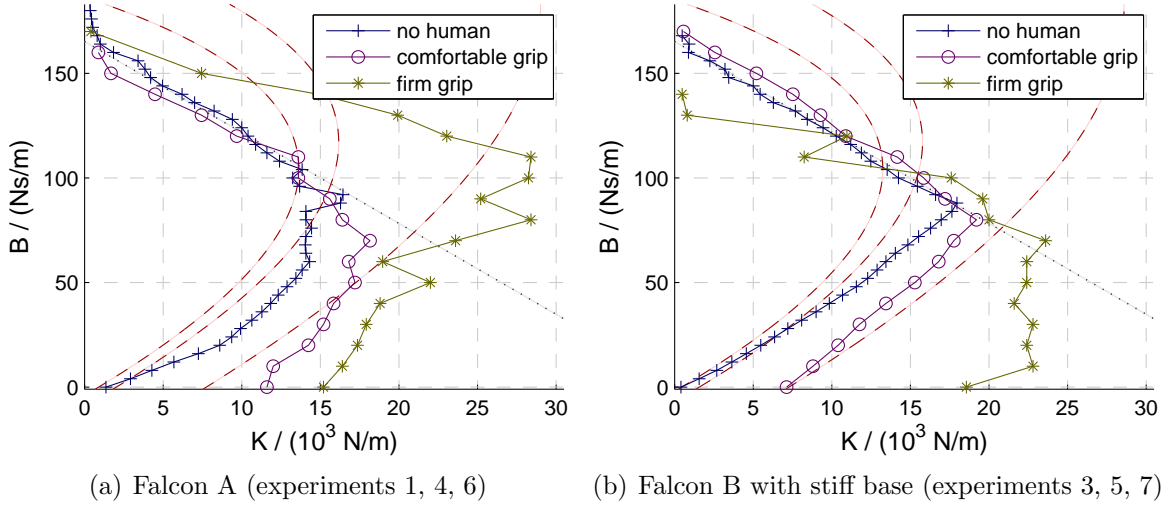


Figure 6.4: The influence of a human operator on the experimental (solid) and theoretical (dashed) stability boundaries for $d = 4$.

dition (6.5), which is shown as black dotted line, can also be used for the experiments with the human operator as rough approximation of this upper stability boundary.

The theoretical boundaries for the parameter values of Table 6.2 are plotted in Fig. 6.4, too. For the sake of clarity, only the curves for a delay of $d = 4$ are exemplarily shown. Similar to the experimental results, the theoretical stable regions grow with a stronger human grip as the two parameters mass and physical damping are increasing, which both contribute to stability. Although both, the experimental and theoretical curves, exhibit the same tendency with increasing grip strength, the location and shape of the curves differ clearly. While the experimental curves without human operator could be predicted to some extent by their theoretical boundaries, this is not the case for the experimental results with a human operator involved. Thus, the following investigations on optimal control design have their focus on the experiments without human operator, while the effect of the human operator is discussed only on three exemplary criteria.

6.1.4 Cost Maps for Optimal Control Design

The previous chapter introduced various optimization criteria to assess the transient behavior of haptic systems inside the stable region. The criteria based on the step-response are applied in this section on the experimental responses in order to obtain cost maps inside the stable regions and to compare them to the theoretical results. For the sake of brevity, only the first two experiments are comprehensively investigated representatively for all conducted experiments. As the difference between Falcon A and B is small, the theoretical results only consider the parameters of the former (i.e., $m = 0.58$ kg and $b = 4$ Ns/m).

In accordance to the previous subsection, the theoretical cost maps are shown for a delay of $d = 4$. As only the discrete-time position signal x^* is available in the experiments, also for the theoretical results, the discrete-time costs C^* are considered. However, the difference to the continuous-time counterparts is marginal, as the time delay is relatively high.

It is important to note that the response-based criteria as defined in the previous chapter consider as input signal the force $F(t)$ that is applied on the continuous-time mass-spring-damper system (see also Fig. 3.3), and not the commanded force. This means for the experimental analysis that the phase shift between commanded force and measured position must be corrected if the costs should be determined according to their definitions. Hence, the first d sampling periods of each recorded transient responses are omitted. During this short period of time, the measured position signal keeps constant, as the device is in rest before each transient response.

Settling Time and Overshoot

Two of the most common optimization criteria are minimizing the settling time and the overshoot. Figure 6.5 shows the resulting cost maps beside the respective theoretical ones. Similar to the form of presentation used in the previous chapter, this figure illustrates the cost distribution by contour lines. A transition over two lines corresponds to a doubling of costs or, in the case of the overshoot, a change of 10 percentage points, respectively. The optimum points are indicated by a blue plus sign. For the sake of clarity, in Fig. 6.5(b), the experimental step responses that exhibit no overshoot are marked by black dots.

The front views on the cost maps are shown below each contour diagram. These plots show as black solid curves the minimal costs for given virtual stiffness K in a linear scale. In addition, they show as green dots the actual costs that occurred for each step response of a course of experiment. To allow for easy comparability between the theoretical and experimental results, all axes of a criterion cover the same value ranges. The minimum cost value of the respective cost map is shown by the lower number on each vertical cost axis.

Although there is a clear difference in the shape of the theoretical and experimental stability boundaries, the cost distributions inside the stable regions appear to match considerably well. In particular, with respect to the overshoot in Fig. 6.5(b), there is a subregion inside the stable region in which the haptic system does not overshoot. This subregion was predicted by the theoretical investigations in the previous chapter and matches reasonably well in size and shape, i.e., the experimental maximum stiffness without overshoot is $K = 6800 \text{ N/m}$ (for experiment 1 and 2) whereas the theoretical analyses resulted in a stiffness of $K = 5109 \text{ N/m}$. Similarly, the minimum settling time differs only slightly, with a theoretical minimum duration of 24 sampling periods T compared to an actual minimum duration of $20 T$ for experiment 1 and $23 T$ for experiment 2, respectively. The numerical values of the optimum points are listed in Table D.1 in Appendix D.1.

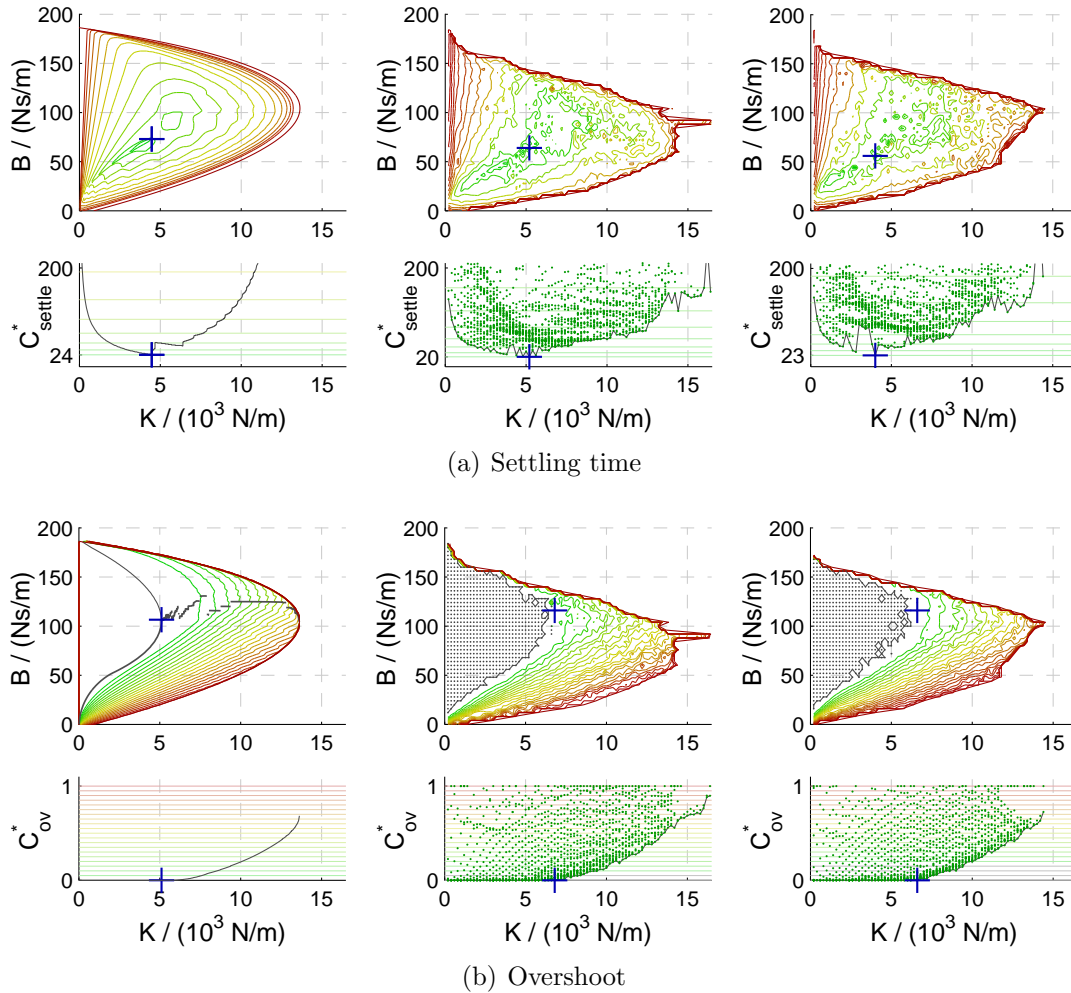


Figure 6.5: Cost maps with contour lines and optimal curves for settling time and overshoot assuming a delay of $d = 4$. The theoretical cost maps (for $m = 0.58$ kg, $k = 0$ N/m, and $b = 4$ Ns/m) are on the left, the experimental ones of Falcon A (experiment 1) in the middle, and those of Falcon B (experiment 2) on the right. The optimal points are marked by blue plus signs. The lower subfigures are the front view on the cost map and hence show the minimal costs for given stiffness K . Their vertical axes indicate the values of the respective optimal costs.

System Energy

Figure 6.6 shows the cost maps of the same experiments (experiment 1 and 2) for the three energy criteria based on the step response O_{Ew}^{step} . Similar to the settling time and the overshoot, these cost figures also reveal a reasonably well match between theory and experiments. The contour lines apparently show a considerable similarity in size and shape. However, there is a clear difference in the optimal cost values, i.e., the experimental costs are up to 43% smaller than the theoretical ones (for criterion O_{E2}^{step} in experiment 1). This difference may originate on the one side from simplifying model assumptions. For instance, jitter and velocity filtering is not taken into account by the theoretical investigation.

On the other side, uncertainties in the estimated device parameters affect both types of results, the theoretical and experimental ones (in comparison, the measured overshoot is independent of these estimations, the settling time is only biased by errors in the estimated delay). For instance, assuming a shorter delay causes the experimental cost to rise because then an earlier starting point in time is considered for the energy integral. In contrast, the theoretical optimal cost would become clearly smaller as higher optimal stiffness and damping factors result (see the previous chapter). In general, with a greater weighting exponent w , the optimal cost values become very sensitive to parameter uncertainties, particularly for O_{E2}^{step} , where the integrand depends on the squared simulation time. Considering that, the theoretical results predict the experimental optimal costs remarkably well.

Also the locations of the optimal points (blue plus signs) in the (K, B) -plane differ between theory and experiments particularly for a weighting exponent of $w = 0$. The main reason is that the optimum points of the first criterion O_{E0}^{step} are extremely susceptible to measurement noise, which is due to the very flat cost distribution around the optimum point. This can clearly be seen by the size of the area surrounded by the inner contour line. The greater the weighting exponent w is chosen, the smaller becomes the inner contour area, and the less susceptible becomes the experimental optimum point. Table D.2 in the Appendix D.1 shows the numerical cost values and the location of the optimum points.

Influence of Human Operator

Figure 6.7 illustrates the effect of the human operator on the cost maps exemplarily for the settling time, the overshoot, and the energy criterion O_{E2}^{step} for the two experiments with the firm grip (experiments 6 and 7). The left plots show the theoretical cost distribution for $m = 1.0$ kg, $b = 34$ Ns/m, and $d = 4$, while the middle and the right plots show the experimental results. The human stiffness k is neglected as it affects only slightly the theoretical costs.¹

¹An increase of the physical continuous-time stiffness to its maximum value found in Chapter 3, i.e., $k = 1000$ N/m for the considered system, would reduce the optimal theoretical costs in Fig. 6.7 by less than 4%.

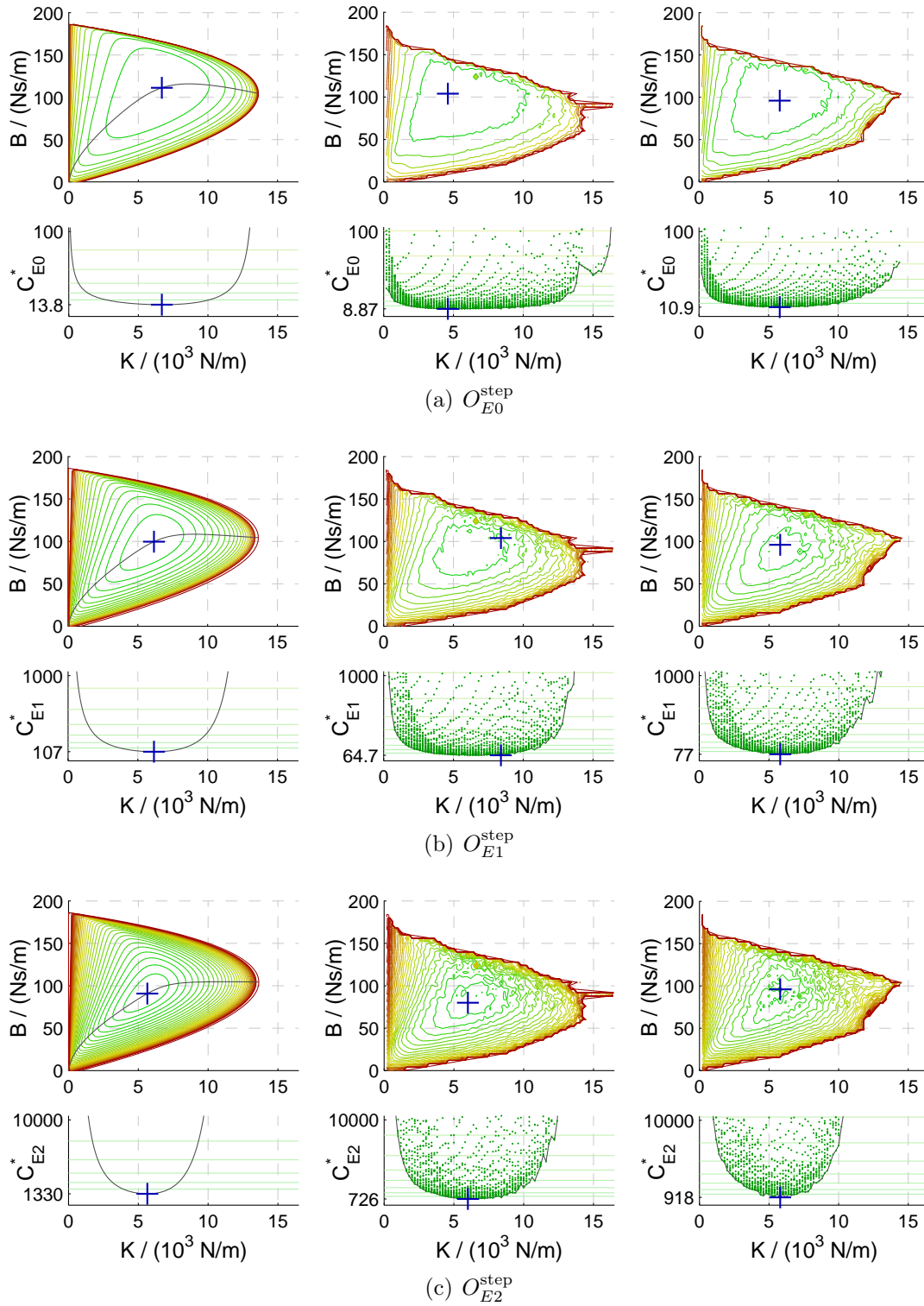
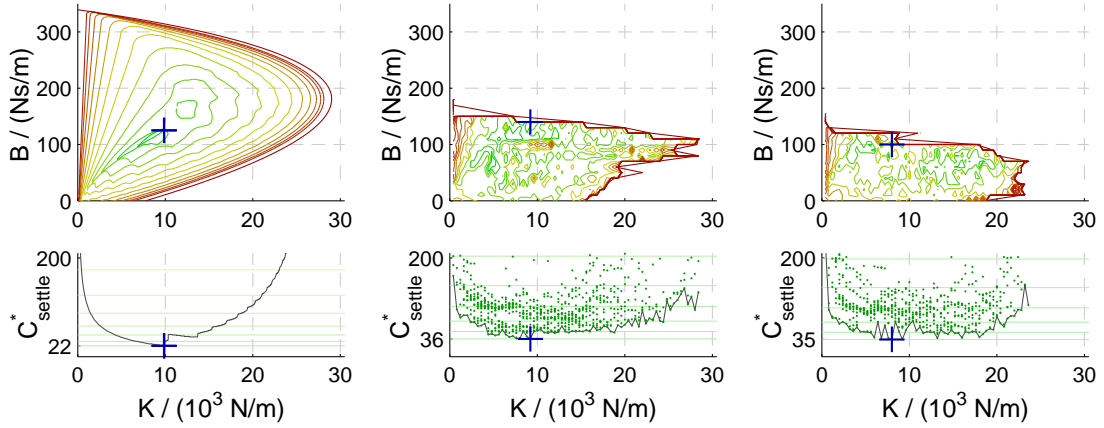
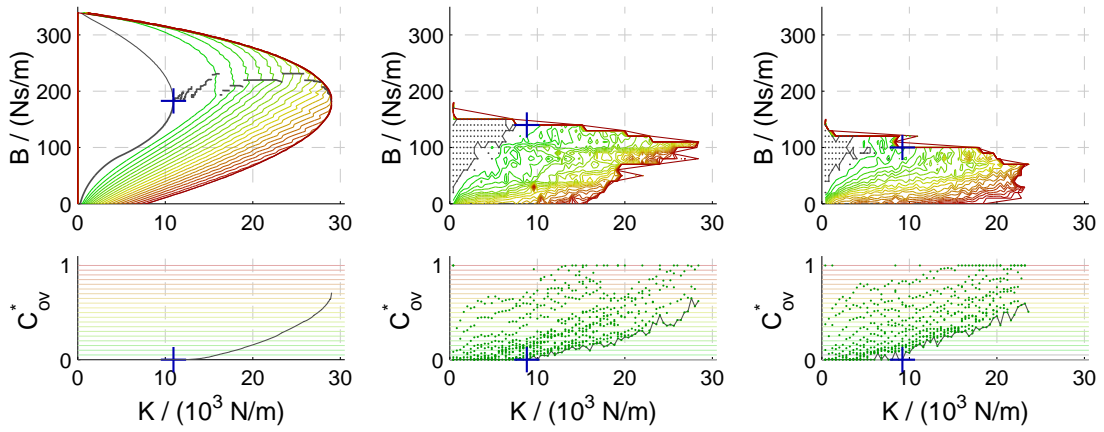


Figure 6.6: Cost maps with contour lines and optimal curves for the three energy criteria based on the step response O_{Ew}^{step} in analogy to Fig. 6.5: theoretical plots (left), experiment 1 (middle), experiment 2 (right).



(a) Settling time



(b) Overshoot

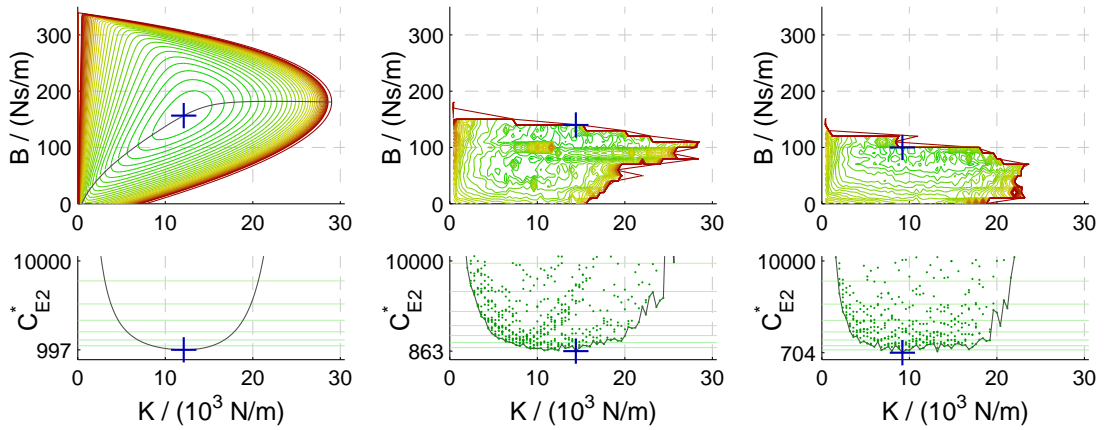
(c) O_{E2}^{step}

Figure 6.7: Cost maps for a firm human grip (i.e., $m = 1.0\text{kg}$, $k = 0\text{N/m}$, $b = 34\text{Ns/m}$, and $d = 4$) for the settling time, the overshoot, and the energy criterion O_{E2}^{step} : theoretical plots (left), experiment 6 (middle), experiment 7 (right).

For the experimental plots, the stable regions are limited by the linear condition (6.5) found above. Interestingly, compared to the theoretical cost maps, the cost distribution of the experimental plots are not a compressed version of the theoretical cost maps, but rather appear to be cut off by the linear condition. In other words, when approaching the linear condition, the costs are not gradually increasing, but keep small. This is also the reason why the optimum points are quite close to this upper stability border instead of being somewhere in the center of the stable region as it is the case for the theoretical results. On the other hand, this close proximity to the stability boundaries implies a steep gradient of costs in the direct vicinity of this border. Hence, if aiming at optimizing the system performance, these optimal points need to be treated with caution. A small variation in the system may cause a huge drop in the performance or may even lead to instabilities.

The optimal costs in these optimal points clearly differ from the theoretical ones. In the case of the energy criterion O_{E2}^{step} , the experiments show lower optimal costs compared to theory. However, the situation is different for the settling time, where the real haptic system takes more than 50% longer to settle than predicted by the theoretical analysis. A possible explanation is that the settling time is very susceptible to vibrations and offset forces induced by the human operator. In fact, the experimental cost distribution maps in Fig. 6.7 appear to be considerably noisier compared to the experiments without a human operator.

6.2 Experiments with the Light-Weight Robot

The second set of experiments was conducted on the bimanual haptic interaction device HUG (see the introductory chapter and [51, 58]). HUG is equipped with two DLR/KUKA Light-Weight Robots (LWR) of the same type with similar dynamic behavior. These robot arms have a serial kinematics and can be operated in torque and position control mode at an update rate of 1 kHz [46]. They are controlled via sercos interface by a real-time computer, which means that jitter and package loss are negligible.

In comparison to the Falcon, the LWRs have a larger workspace that is similar to that of a human arm. Moreover, there is an important difference to traditional haptic devices with respect to their drives. While haptic devices are usually mechanically backdrivable, this is not the case for the LWRs. Instead, the LWR joints are equipped with torque sensors that allow for torque controlled operation mode with a controlled backdrivability. The respective controllers run on the joints' control electronics at a sampling rate of 3 kHz.

6.2.1 Experimental Setup and Procedure

The primary goal of the experiments with the LWR is to investigate to what extent the theoretical analysis of this thesis can be used to predict the behavior of such complex robotic systems. Moreover, the experiments aim at revealing the influence of additional

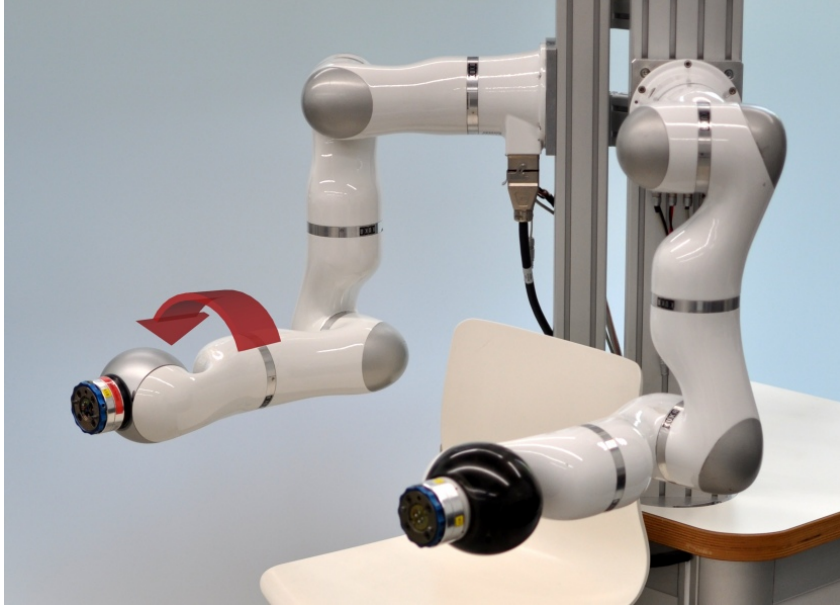


Figure 6.8: The experimental setup with the Light-Weight Robots of the bimanual haptic interaction device HUG. The red round arrow indicates the direction of the rotational movements in the experiments.

time delay, which was artificially introduced. To this end, stability boundaries and cost maps were experimentally determined without human operator for different artificial time delays ranging from 0 to 6 ms.

The experiments were conducted on the fifth joint of the left robot in Fig. 6.8 as indicated by the red round arrow. Choosing this joint is a tradeoff, as the joints with higher inertia (the ones that are closer to the base) excite stronger vibrations in the robot pedestal, whereas the joints with lower inertia are more susceptible to unconsidered effects such as static friction. All the other joints were turned off during the experiments, i.e., their internal brakes were activated.

The experimental procedure was the same as for the Falcon. For each tested parameter pair of virtual stiffness K_{rot} and damping B_{rot} , the active joint was excited by an input torque step of $\tau_0 = 15 \text{ Nm}$ and the step responses were recorded. From these responses, the cost maps were computed offline after the experiments were finished and then compared to the theoretical results. The steady-state position of the joint was chosen to be always at the same position in the center of the joint's motion range, i.e., at a joint angle of $\Theta_\infty = 0$. The set of damping factors was $B_{\text{rot}} \in \{0, 1, 2, \dots, 40\} \text{ Nms/rad}$ and the initial step size for the stiffness K_{rot} was 200 Nm/rad . With these values, the course of experiment without artificial time delay comprised 1,025 step responses and took around six minutes. For the experiments with additional delay, fewer step responses were recorded as smaller stable regions resulted.

6.2.2 System Parameter Estimation

In order to compare the experimental to the theoretical results, the three parameters of inherent time delay t_d , angular mass I , and physical damping b_{rot} were estimated first. To determine these parameters, the same method was used as for the Falcon. The closed-loop delay without artificial delay was found to be constant at $t_d = 2 \text{ ms}$.² In comparison to the Falcon, no jitter occurred for the LWR. The physical damping b_{rot} was less than 0.1 Nms/rad (the damping is cancelled by the joint controller) and hence is neglected in the following evaluation.

The rotational inertia was determined to be $I = 0.19 \text{ kg}\cdot\text{m}^2$. The value of the inertia is used to determine the theoretical and experimental results. However, although it scales the theoretical stable regions, the inertia has no effect on the theoretical optimal costs (see the previous chapter). For the experimental results, this parameter value only influences the costs of the energy criteria as it scales contribution of the kinetic energy. The experimental stability boundaries and the other criteria are independent of the determined value of the moment of inertia. Note that, similar to the Falcon, this value for the inertia results from the commanded torque and the measured position signals and hence takes into account the influence of the joint controller. The real moment of inertia of this robot joint is only around 3% of this value. The deviation of the determined inertia is mainly caused by the joint controller.

6.2.3 Stability Boundaries

Figure 6.9 shows the theoretical (left) and experimental (right) stability boundaries for an artificial delay of up to 6 ms, respectively a total closed-loop delay of $t_d = 8 \text{ ms}$. Both kinds of stable regions shrink with increasing artificial delay. A clear difference appears between the theoretical and the experimental stability curves. The experimental curves are substantially smaller than the theoretical ones. This holds especially true for the height of the experimental regions, which is between one third and one half of the theoretical regions' height.

Consequently, the theoretical analysis is poorly suited to predict the shape of the LWR's stability boundaries. The following investigations examine if this also holds for the costs inside the stable regions.

6.2.4 Cost Maps for Optimal Control Design

In analogy to the experimental evaluation with the Falcon, this section investigates the cost maps of the LWR and compares them to the theoretical results. Figure 6.10 and 6.11 show the theoretical and experimental cost maps for the experiment without additional delay. The shown theoretical plots assume a delay of $d = 2$, a rotational inertia of $I = 0.19 \text{ kg}\cdot\text{m}^2$, and no continuous-time stiffness and damping, i.e., $k_{\text{rot}} =$

²In comparison to previous experiments [50], the total closed-loop delay could be reduced from 4 ms to 2 ms by profound modifications in the software framework.

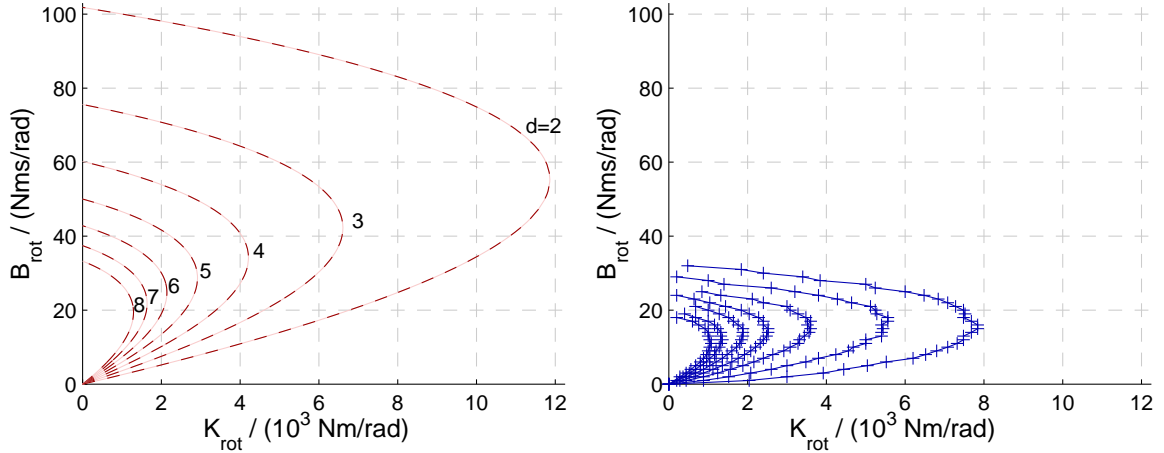
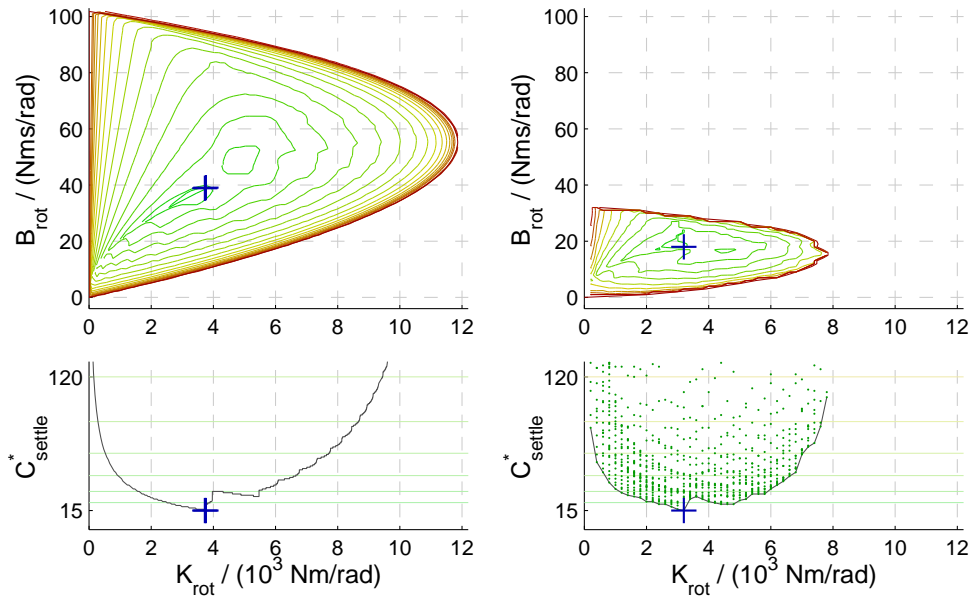


Figure 6.9: The influence of time delay on the theoretical (left) and on the experimental (right) stability boundaries. In the experiments, an artificial delay of up to 6 ms was introduced and increased at steps of 1 ms. The theoretical curves (for $I = 0.19 \text{ kg} \cdot \text{m}^2$, $k_{\text{rot}} = 0 \text{ Nm/rad}$, and $b_{\text{rot}} = 0 \text{ Nms/rad}$) are shown for delay factors of $d \in \{2, 3, 4, 5, 6, 7, 8\}$ corresponding to a total delay t_d between 2 ms and 8 ms. The plots show that with additional delay, both the experimental and the theoretical stable regions shrink.

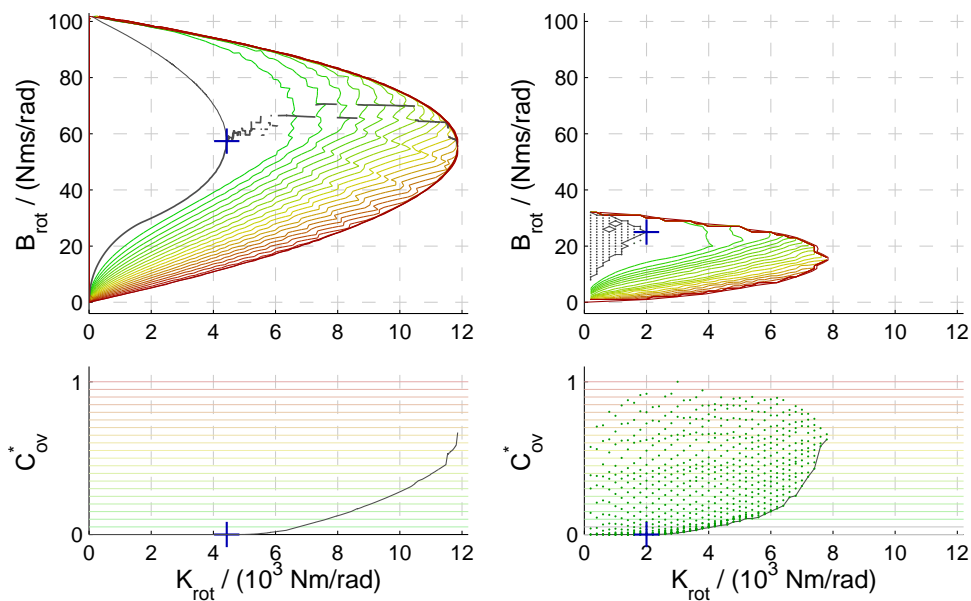
0 Nm/rad and $b_{\text{rot}} = 0 \text{ Nms/rad}$. Similar to the form of presentation used above, these figures illustrate the cost distribution by contour lines. The distance between three lines corresponds to a doubling of costs, or in the case of the overshoot, a change of 10 percentage points, respectively. For the overshoot criterion in Fig. 6.10(b), subregions without overshoot occur inside the stable regions, which are illustrated by a black surrounding curve.

The optimal points of the cost maps are marked by blue plus signs. Their cost values can be read from the subfigures below each cost map (their precise locations are listed in Appendix D.2). For the location of the optimal points, there is an obvious mismatch between theory and experiments. For instance, the relative error of the optimum stiffness is up to 130% in case of the overshoot criterion O_{ov} (see Fig. 6.10(b)).

For the optimal costs, however, the difference is comparably small between theory and robot. The optimum settling time even matches the theoretical results with a duration of 15 sampling periods. For the three energy criteria, the robot has a lower optimal performance (i.e., higher optimal costs) than predicted by theory. The relative error of the optimum costs is 21% for O_{E0}^{step} , 35% for O_{E1}^{step} , and 38% for O_{E2}^{step} . Its optimal points for the energy criteria are located very close to the upper part of the stability boundary. It seems as if the stability boundary prevents the robot joint from reaching its actual optimal operating points.



(a) Settling time



(b) Overshoot

Figure 6.10: Cost maps with contour lines and optimal curves for settling time and overshoot assuming a delay of $d = 2$. The theoretical cost maps (for $I = 0.19 \text{ kg} \cdot \text{m}^2$, $k_{\text{rot}} = 0 \text{ Nm/rad}$, and $b_{\text{rot}} = 0 \text{ Nms/rad}$) are on the left, and those of the LWR on the right. The optimal points are marked by blue plus signs. The lower subfigures are the front view on the cost map and hence show the minimal costs for given stiffness K_{rot} . Their vertical axes indicate the values of the respective optimal costs.

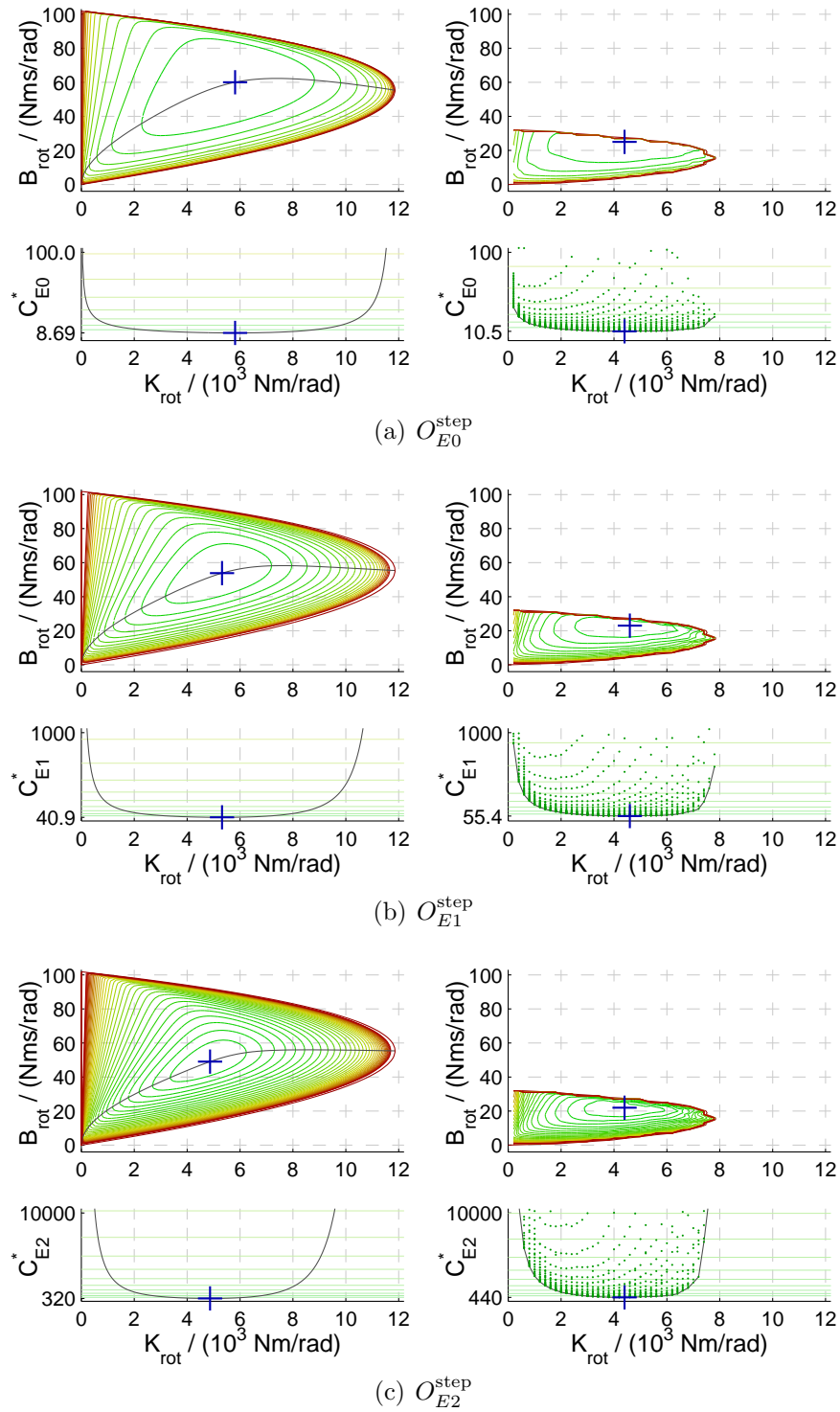


Figure 6.11: Cost maps with contour lines and optimal curves for the three energy criteria based on the step response O_{Ew}^{step} in analogy to Fig. 6.10: theoretical plots (left), experiment plots of the LWR (right).

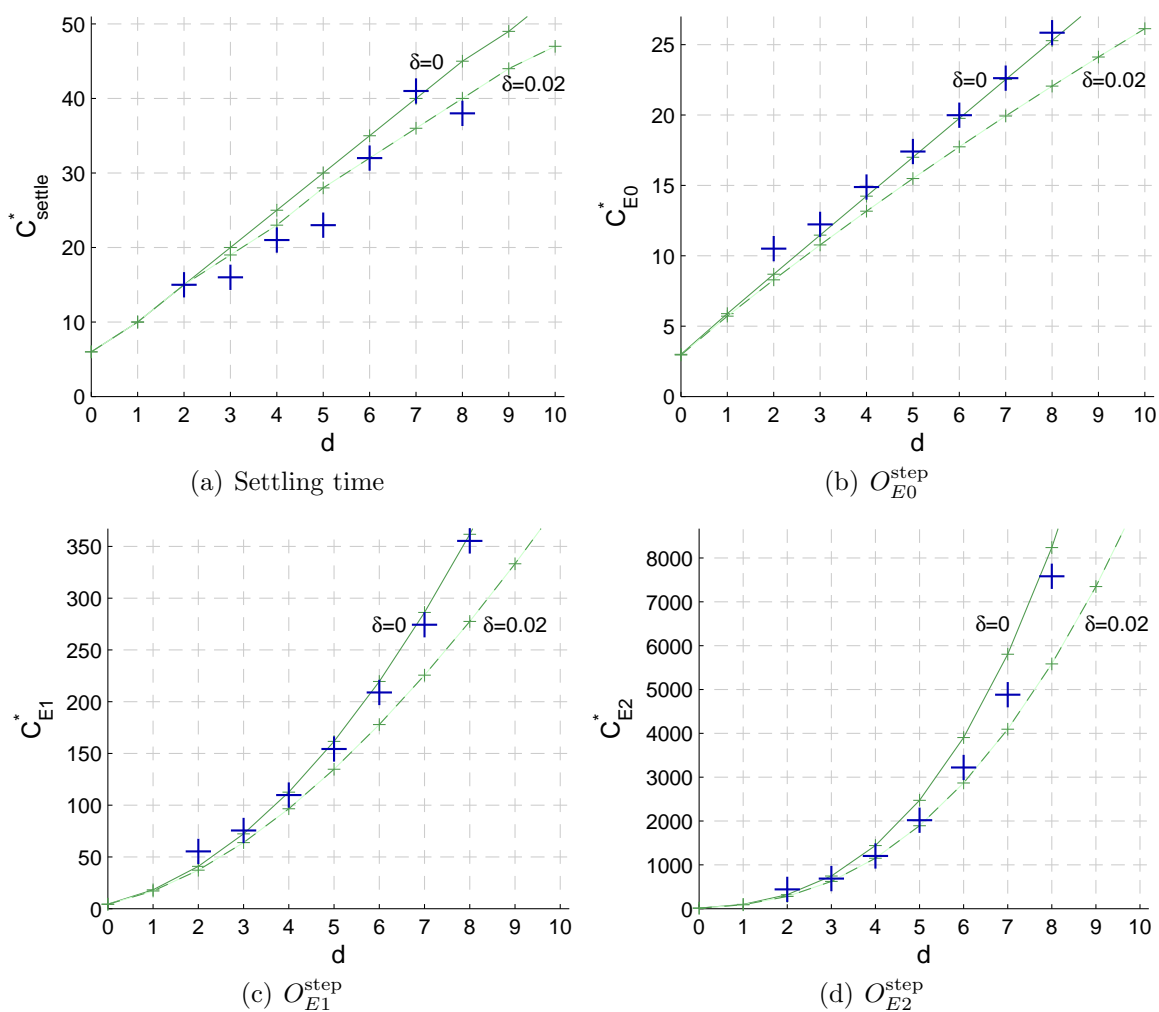


Figure 6.12: The experimental versus the theoretical optimal costs over time delay for the settling time criterion and the three energy criteria. The optimal costs of the experiments are marked by blue plus signs for the robot. The green solid curves represent the course of the theoretical optimal costs. The green dashed curves show the theoretical costs for a physical damping $\delta = 0.02$ ($b_{\text{rot}} = 3.8 \text{ Nms/rad}$).

6.2.5 Influence of Delay on the Optimal Costs

Figure 6.12 shows the influence of delay on the optimal costs for the settling time and the three energy criteria. The blue plus signs are the actual optimal costs that occurred during the experiments. The green solid lines represent the theoretical course of the optimal costs. The green dashed lines show the optimal costs for a physical damping of $\delta = 0.02$ (or $b_{\text{rot}} = 3.8 \text{ Nms/rad}$), which is the upper limit of the parameter range identified in Chapter 3.

It can be clearly seen that the settling time is prone to measurement noise and external disturbances (Fig. 6.12(a)). A small position deviation may cause a huge error in the detected settling time if it leads to a change of the last local extremum of the transient response that crosses the threshold band. In comparison, the energy-based costs exhibit a much smoother course. Irrespective of this, for all four criteria, the experimental optimal costs follow the theoretical predictions remarkably well (see Appendix D.2 for the numerical values). With increasing delay and hence slower dynamical movements, the unmodeled properties of the LWR appear to have less effect on the performance. Or, in other words, for small delays, the optimal performance of the LWR is additionally affected by factors other than delay and discrete-time sampling.

6.3 Discussion

This chapter assessed the practical relevance of the theoretical analysis. To this end, an experimental evaluation with two different devices, a Novint Falcon and a LWR, was conducted. In this evaluation, for the first time the theoretical and experimental cost maps were compared, and the influence of hardware configurations, human operator, and time delay on these costs was analyzed.

Both devices differ with regard to various aspects from the model that was assumed in the theoretical analysis. While the Falcon is a low-cost desktop device with some unfavorable properties including varying time delay (jitter), vibration modes, sensor quantization, and nonlinearities, the LWR differs from the model due to its actively controlled backdrivability and its joint controllers. The aim of the experiments was to evaluate how well the devices follow the predicted behavior of the theoretical analysis despite these differences.

The experiments with the Falcon and without human operator show a relatively good match with the theoretical results. The difference between the three hardware configurations of the Falcon is small, even if the base of the Falcon is exchanged by a stiff base. The experimental stability boundaries exhibit a linear upper bound that was not predicted by theory.

The cost distributions between the theoretical and the experimental results appear to match even better than for the stability boundaries. Also the region without overshoot, which was found in the theoretical analysis, occurs in the experiments. For all considered criteria, the experimentally determined optimal costs for the Falcon are somewhat lower than the theoretical ones. This deviation is not surprising considering the parameter uncertainties and the differences between the real Falcon and the used model. On the other hand, the influence of the higher physical damping of the Falcon A compared to Falcon B follows the theoretical predictions and results in lower optimal costs.

The weighting exponent w of the energy criteria has a clear influence on the susceptibility of the optimum points. The greater the weighting exponent, the more sensitive become the optimal costs with regard to parameter uncertainties, but also the more precise become the locations of the optimum points, and vice versa.

The stability curves of the experiments with a human operator clearly differ from the theoretical curves. Compared to theory, the range of stable damping gains is much smaller. The linear bound that appeared in the experiments without operator also appears in these experiments and cuts off the stable region. Due to this bound, the determined optimum points lie in the direct vicinity of the stability border and result in higher costs than theoretically feasible. These points need to be treated with caution if employed on the haptic device, as small variations in the system may cause a huge drop in the performance or even lead to unstable behavior.

In the experiments with the LWR without additional delay, the difference between theory and experiments is greater compared to the experiments with the Falcon. Firstly, the size of the experimental stable regions is clearly smaller than the theoretical regions. And secondly, for the energy criteria, the experimental optimal costs are greater than in theory, i.e., the optimal performance of the LWR is worse than predicted. The optimum points of the energy criteria are located close to the stability boundaries, which is similar to situations with human operator holding the Falcon where the performance is extremely sensitive to small system variations.

If an artificial delay is introduced to the LWR, then the experimental and the theoretical regions shrink in a similar way and their optimal costs converge. In particular, the relative error of the theoretical predictions reduces with increasing delay. Already for an additional delay of one sampling period the theoretical costs can be reasonably used to predict the real robot's behavior. On the other hand, for small delays, other factors than delay and discrete-time sampling outweighs the influence on the optimal performance.

The inertia was determined based on the parameter signals that are visible to the virtual environment. This apparent inertia is significantly higher than the actual inertia of the robot as it is strongly influenced by the joint controller. However, only with this value, a reasonable match between theory and experiments results.

To conclude, the following key insights of the experimental evaluation may be summarized:

1. The theoretical analysis is suitable to predict the optimal performance of a haptic device, in particular if an artificial delay is present. Hence, the approximation formula (5.19) and the rule of thumb for the optimal settling time, which were both introduced in the previous chapter, can be used to estimate the optimal performance of a haptic device. However, it is not possible with the theoretical approach to predict the precise course of the stability boundary and the exact position of the optimum operation point, especially if the used haptic device has an internal controller that distorts the results.
2. The theoretical stability boundaries and the experimental costs of the energy criteria depend on the estimated value of inertia. A reasonable match between theory and experiments results only if the apparent inertia is considered, i.e. the inertia that is seen by the virtual environment. Depending on the device and its internal controller, this parameter value may drastically vary from the actual inertia. In comparison to the energy criteria, however, the optimal settling time does not depend on any estimate of the inertia.
3. The stabilizing effect of the human operator was confirmed. However, its influence on the cost maps is more complex than it was predicted by the theory. The respective experimental cost maps appear to be noisier than in the experiments without a human operator involved.

These experiments confirm that despite the various differences between the used haptic devices and the model employed in the theoretical analysis, the theoretical findings can still predict the behavior of the haptic system to a certain extent.

The study of the linear case is important since linear systems govern the behavior of nonlinear ones in the neighborhood of a particular motion and also because the results point the way towards a complete nonlinear theory.

Willems [121]

7

Conclusion

Providing haptic force feedback brings great benefits to users in a wide range of applications. In virtual reality applications, such feedback is generated by means of haptic rendering, i.e., it is artificially computed from a virtual environment. This thesis investigated various control aspects in haptic rendering to precisely understand the influence of the system parameters on performance and to facilitate setting the controllable parameters in an optimal way. This chapter summarizes the key contributions of this thesis and discusses its possible impact and future perspectives.

7.1 Summary

The theoretical approach introduced in this thesis considers a haptic system modeled as hybrid control system that contains both discrete- and continuous-time elements. For the first time, the combined effect of delay and human operator on such a hybrid control system was investigated. In addition, optimal control methods were introduced to the field of haptic rendering and applied to this system. The model of the investigated haptic system was deliberately kept simple only consisting of linear elements. Thus, a linear analysis could be conducted that comes with clear benefits, as it is an essential and fundamental part of a more complete nonlinear approach, and approximates the behavior of more complex and realistic nonlinear models in the vicinity of a local operating point [121]. Throughout the thesis, normalized dimensionless system parameters were used that facilitate the analysis and its presentation and, even more importantly, they led to general results with broad applicability.

The theoretical contributions of this thesis may be separated into stability, passivity, and optimal control. The theoretical part is complemented by an experimental study to verify the theoretical findings. The following sections summarize the contributions accordingly.

7.1.1 Stability

Stability is a necessary precondition to safely and efficiently generate and provide haptic feedback. In the course of analyzing stability, an exact form of the closed-loop transfer function of the hybrid system was determined in the discrete-time domain. This function revealed parameter dependencies that led to the definition of normalized dimensionless parameters. Their introduction had the direct benefit of reducing by two the number of system parameters that must be explicitly considered in the analysis. Thus, the system's stability boundaries were determined in the parameter plane of the normalized parameters. The normalizations imply that the stable regions scale linearly with the mass and grow with faster sampling rate.

On the basis of the stability boundaries, the influence of delay and human operator was investigated. Time delay has a detrimental influence on stability that was graphically and numerically analyzed. The effect of the human operator modeled as mass-spring-damper system is mainly constituted by its mass contribution. In comparison, the influence of human stiffness and damping is small for realistic parameter values. Thus, in total, the human operator is beneficial with respect to the size of the stable regions.

For small values of virtual stiffness and damping, the relationship between all system parameters can be approximated by a linear stability condition. It states that the instability introduced by the product of virtual stiffness and effective delay can be compensated by any kind of viscous damping, discrete- or continuous-time one. The dynamic mass and the human stiffness both have no influence on this linear condition.

7.1.2 Passivity

Passivity is a frequently utilized tool to obtain robustly stable haptic systems as it does not require a model of the human arm. In this thesis, the analytical passivity boundaries for the considered time-invariant hybrid haptic system were calculated using the passivity approach of Colgate and Schenkel [24] and extending it to time delayed systems.

It turned out that for passivity, substantially different parameter dependencies result than for stability. Hence, the passivity boundaries can be drawn in a normalized parameter plane different to that of stability. In detail, these normalizations involve a linear dependency of the passive regions on continuous-time damping. In addition, they reveal that an increase of the sampling rate causes the passive regions to grow only towards higher virtual stiffness gains. The total dynamic mass, which is a combination of human arm and device mass, has no influence on passivity. Time delay highly affects the passive regions, although its relative influence for passivity is weaker compared to stability. A section of the passivity boundaries is linear and coincides with the linear stability condition for small parameter values.

In a comparison to stability for realistic parameter values, the passive regions appeared as small subregions of the stable regions. This vast difference in size emphasizes

the fact that passivity for time-invariant systems is highly conservative with regard to stability. It was shown that the reason for this high conservativeness of passivity is in the range of covered oscillation frequencies ranging up to the Nyquist frequency. However, to let a real haptic system oscillate with the Nyquist frequency, stiffness values are needed that are up to 10,000 times greater than that of real human arms.

7.1.3 Optimal Control

While the analysis of stability and passivity yielded stable and passive regions in the parameter space and revealed fundamental parameter dependencies, these results are only of limited use for tuning the system parameters in order to optimize its performance. However, they set the fundament for an optimal control analysis of haptic systems. To this end, design objectives for haptic systems were postulated and various performance criteria were investigated that are based on the system poles or the transient response. The criteria take into account settling time, system damping, overshoot, and system energy.

For each criterion, a dimensionless performance measure was defined to generate results that hold for any positive mass and sampling rate. On this basis, three-dimensional cost maps inside the stable parameter regions were determined, which disclose the respective optimal points with minimum cost. For the settling time, the results revealed a clear mismatch of pole-based and response-based optimal solutions. Consequently, the pole-based approach is only of limited use when aiming at optimizing the transient behavior of a haptic system. For the overshoot criterion, a subregion of the stable region was identified, in which the system exhibits no overshoot in its step response.

It was further found that the costs in the optimal points approximately increase linearly, quadratically, or cubically with delay, depending on the criterion. Thus, a polynomial approximation function could be given for each criterion to predict these optimal performance values under the influence of delay. These dependencies can be formulated as easy-to-remember rules of thumb, as it was exemplarily done for the settling time criterion.

7.1.4 Experiments

Experiments on two different devices were performed, a Falcon and a DLR/KUKA light-weight robot. The shape of the stability boundaries and the location of the optimal points was distorted by internal controllers and unmodeled properties of the devices. Nevertheless, for both devices, there was a remarkable accordance to the theoretical results with respect to the optimal costs. Also, the predicted influence of the human operator and time delay was supported by the experiments. These experiments confirm that despite various differences between the used haptic devices and the model employed in the theoretical analysis, the theoretical findings can still predict the behavior of the haptic system to a certain extent.

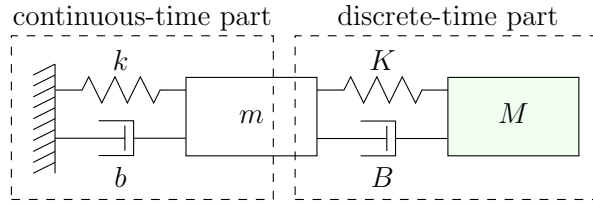


Figure 7.1: Physical model similar to the one investigated in this thesis (see Fig. 3.2) but extended by a virtual mass M that is coupled by means of virtual coupling to the haptic device.

7.2 Future Research Work and Perspectives

The presented approach already proved its practical benefits for the two applications of virtual assembly verification and training of mechanics (see the introductory chapter). Equally, the research findings also hold for other promising haptic rendering applications, comprising training of surgeons [64, 119], rehabilitation [113], and computer games [43]. The successful usage emphasizes the importance of continuing research in this direction. There are various and diverse aspects with which regard the approach may be enhanced, as discussed in the following lines.

More accurate results may be obtained by considering **more comprehensive and realistic models** of the haptic system. Such extended models may take into account various factors. In particular, velocity filtering is often required for real haptic systems to prevent them from oscillating [17]. Similar, the mechanical compliance of haptic devices that typically comes with their lightweight design affects the performance of a haptic system [31, 28]. In addition, nonlinearities such as static friction, sensor quantization, or the unilateral constraints of virtual walls were found to have a significant influence [4, 33] and appear to be worth investigating further. More realistic models may also consider more complex virtual environments, which not only consist of virtual walls, but which render more physical phenomena, too. The diploma thesis of Magana [76] already points into this direction and introduces a virtual mass to the analysis (see Fig. 7.1). With such extensions, the approach becomes applicable to tele-manipulated systems, as already shown with respect to stability by Miandashti and Tavakoli [79].

Enhancing the theoretical approach by using **different analysis methodologies and controllers** may lead to improvements with regard to accuracy, robustness, and applicability of the results. In this way, analytical representations of the optimal curves and points and of the stability boundaries for long delays may be determined, e.g., by the method of singular frequency [9, 10]. Also, delays that are not a whole multiple of the sampling period may be exactly taken into account, e.g., by using the advanced or modified Z-transform introduced by Jury [61]. Optimal points that are robust with respect to parameter uncertainties may be determined by considering other optimiza-

tion criteria or other control approaches, e.g., the H_∞ method [1] or fractional-order control [83] respectively. Most promising, however, seems the extension of the analysis towards time-variant control, where the control parameters may change with time. Such controllers were already successfully employed in haptics with the time-domain passivity controller [42], but also in other domains such as the variable impedance control in robotics [15].

Even though there are many possible ways of enhancing the theoretical approach, the findings of the thesis facilitate also other future research activities. Firstly, the optimal control analysis presented in this thesis provides a theoretical basis for future **psychophysical studies**. In particular, the optimal points that were determined in the analysis can be considered as candidate solutions for optimizing the human perception in haptic rendering. And secondly, the findings are valuable for **designing new haptic devices** with high performance. The results of the optimal control study may be used to predict the optimal performance of a haptic device. And, even more importantly, the design guidelines that were derived from the stability analysis give recommendations for the mechanical system parameters.

In summary, the findings presented in this thesis are important (I) for understanding the influence of the parameters on a haptic system performance, (II) for being able to optimally tune these parameters, (III) for designing new haptic devices, and (IV) function as a basis for future psycho-physical studies. However, not only haptic rendering applications may benefit from these results because various other control systems exhibit a hybrid characteristic similar to the investigated system, too. In fact, similar control systems occur in the related domain of impedance controlled robots [26], but also for motor controllers in general [60], or even — due to the electromechanical analogies (see Appendix E) — for electrical systems [19, 63].

A

Discrete-Time Equivalents

In this appendix, the discrete-time zero-order hold (ZOH) equivalent transfer functions of the continuous-time elements of a damped mass respectively of a mass-spring-damper system are calculated. In comparison to the solution of text books (e.g. [2, 75]), the calculated formula for the mass-spring damper does not require a distinction of cases depending on the system damping.

The used approach calculates the the states (position and velocity) of the system at the sampling instants in the time-domain. In order to clearly demonstrate how the calculation of a ZOH-equivalent can be performed, the equivalent of a damped mass is calculated first as a simple example. Then, the ZOH-equivalent of the mass-spring-damper system is calculated analogically. In both cases, $H_0(s)$ denotes the transfer function of the ZOH-element as it was introduced in Chapter 3.

A.1 Damped Mass

Theorem A.1. *The zero-order hold equivalent of the transfer function of a damped mass $H_x(s) = 1/(ms^2 + bs)$ from force to position is*

$$\mathcal{Z} \{H_x(s)H_0(s)\} = \frac{Tb(z - c) + m(1 - z)(1 - c)}{b^2(z - 1)(z - c)} \quad (\text{A.1})$$

with

$$c = e^{-Tb/m}, \quad (\text{A.2})$$

under the condition that the force is constant between two sampling instants.

Proof. The differential equation of a damped mass m is

$$F = b\dot{x} + m\ddot{x} \quad (\text{A.3})$$

with viscous damping b , mass m , force F , and position x . Solving this differential equation for velocity \dot{x} given the force F being constant yields

$$\dot{x}(t) = \dot{x}_\infty - (\dot{x}_\infty - \dot{x}_0) e^{-tb/m} \quad (\text{A.4})$$

with $\dot{x}_0 = \dot{x}(0)$ the initial velocity and $\dot{x}_\infty = F/b$. Therefore, by assuming that the force F is not changing during one sampling period T , for the velocity at the points in time $t = \kappa T$ with $\kappa \in \mathbb{N}_0$ yields

$$\dot{x}_{\kappa+1} = c\dot{x}_\kappa + (1-c)\frac{F_\kappa}{b} \quad (\text{A.5})$$

with

$$c = e^{-Tb/m}. \quad (\text{A.6})$$

Thus, the exact transfer function from force to velocity is

$$H_v(z) = \frac{\dot{x}}{F} = \frac{1-c}{b(z-c)}. \quad (\text{A.7})$$

The position results as integral from the velocity $\dot{x}(t)$ in (A.4) with respect to time t as

$$\begin{aligned} x(t) &= \int_0^t \dot{x}(\tau) d\tau + x(0) \\ &= \dot{x}_\infty t + \frac{m}{b} (\dot{x}_0 - \dot{x}_\infty) (1 - e^{-tb/m}) + x(0). \end{aligned} \quad (\text{A.8})$$

Thus, for discrete points in time $t_\kappa = \kappa T$ with $\kappa \in \mathbb{N}_0$, and under the condition that the force F does not change during a sampling period T yields

$$x_{\kappa+1} = x_\kappa + \frac{F_\kappa}{b} T + \frac{m}{b} \left(\dot{x}_\kappa - \frac{F_\kappa}{b} \right) (1-c). \quad (\text{A.9})$$

Hence, the exact transfer function from force to position is

$$H_x(z) = \frac{x}{F} = \frac{Tb(z-c) + m(1-z)(1-c)}{b^2(z-1)(z-c)}. \quad (\text{A.10})$$

□

A.2 Mass-Spring-Damper System

Theorem A.2. *The zero-order hold equivalent of a continuous-time mass-spring-damper system $H_x(s) = 1/(ms^2 + bs + k)$ is*

$$\mathcal{Z}\{H_x(s)H_0(s)\} = \frac{2(z + e^{-bT/m}) - (z + 1)(c_2 + c_3) + bT(z - 1)(c_2 - c_3)/(mc_1)}{2k(z^2 - (c_2 + c_3)z + e^{-bT/m})} \quad (\text{A.11})$$

with

$$\begin{aligned} c_1 &= \sqrt{(bT/m)^2 - 4kT^2/m} \\ c_2 &= e^{-(bT/m+c_1)/2} \\ c_3 &= e^{-(bT/m-c_1)/2}, \end{aligned} \quad (\text{A.12})$$

under the condition that the force is constant between two sampling instants.

Proof. The differential equation of a mass-spring-damper system is

$$F = kx + b\dot{x} + m\ddot{x} \quad (\text{A.13})$$

with stiffness k , viscous damping b , mass m , force F , and position x . Solving this differential equation for position x and velocity \dot{x} , given the force F being constant yields

$$\begin{aligned} x(t) &= \frac{(2km\dot{x}_0 + (b+c)(kx_0 - F))e^{-t(b-c)/(2m)}}{2kc} \\ &\quad - \frac{(2km\dot{x}_0 + (b-c)(kx_0 - F))e^{-t(b+c)/(2m)}}{2kc} \\ &\quad + F/k \end{aligned} \quad (\text{A.14})$$

and

$$\begin{aligned} \dot{x}(t) &= \frac{(b+c)(2km\dot{x}_0 + (b-c)(kx_0 - F))e^{-t(b+c)/(2m)}}{4kmc} \\ &\quad - \frac{(b-c)(2km\dot{x}_0 + (b+c)(kx_0 - F))e^{-t(b-c)/(2m)}}{4kmc} \end{aligned} \quad (\text{A.15})$$

with $c = \sqrt{b^2 - 4km}$, initial position $x_0 = x(0)$, and initial velocity $\dot{x}_0 = \dot{x}(0)$. Therefore, by assuming that the force F is not changing during one sampling period T , for the velocity at the points in time $t = \kappa T$ with $\kappa \in \mathbb{N}_0$ yields

$$\begin{aligned} x_{\kappa+1} &= \frac{(2km\dot{x}_\kappa + (b+c)(kx_\kappa - F_\kappa))e^{-T(b-c)/(2m)}}{2kc} \\ &\quad - \frac{(2km\dot{x}_\kappa + (b-c)(kx_\kappa - F_\kappa))e^{-T(b+c)/(2m)}}{2kc} \\ &\quad + F_\kappa/k \end{aligned} \quad (\text{A.16})$$

and

$$\begin{aligned} \dot{x}_{\kappa+1} &= \frac{(b+c)(2km\dot{x}_\kappa + (b-c)(kx_\kappa - F_\kappa))e^{-T(b+c)/(2m)}}{4kmc} \\ &\quad - \frac{(b-c)(2km\dot{x}_\kappa + (b+c)(kx_\kappa - F_\kappa))e^{-T(b-c)/(2m)}}{4kmc}. \end{aligned} \quad (\text{A.17})$$

Solving (A.17) in the z-domain for \dot{x} , and substituting the velocity \dot{x} in (A.16) by its result yields (A.11). □

B

Tables for the Influence of Delay on the Maximum Virtual Stiffness and Damping

This appendix contains value tables for the curves in Fig. 3.9, showing the influence of the delay factor d on the maximum stable virtual stiffness α_{\max} and damping β_{\max} . The tables also show the relative drop of α_{\max} and β_{\max} with respect to the case without delay $d = 0$. They also contain the corresponding parameters in the maximum points $\beta|_{\alpha_{\max}}$ and $\alpha|_{\beta_{\max}}$ that are needed to achieve maximum stable stiffness α_{\max} and damping β_{\max} respectively. There are four tables, one for each corner of the rectangle defined by the admitted parameter range (3.17).

Table B.1: Maximum stable discrete-time parameters for $\gamma = 0$ and $\delta = 0$.

delay d	maximum stiffness			maximum damping		
	α_{\max}	$\frac{\alpha_{\max}}{\alpha_{\max} _{d=0}}$	$\beta _{\alpha_{\max}}$	β_{\max}	$\frac{\beta_{\max}}{\beta_{\max} _{d=0}}$	$\alpha _{\beta_{\max}}$
0	0.68629	100.00%	0.828	2.00000	100.00%	0.000
1	0.14447	21.05%	0.425	0.82843	41.42%	0.000
2	0.06243	9.10%	0.291	0.53590	26.79%	0.000
3	0.03478	5.07%	0.222	0.39782	19.89%	0.000
4	0.02216	3.23%	0.180	0.31677	15.84%	0.000
5	0.01535	2.24%	0.151	0.26330	13.17%	0.000
6	0.01126	1.64%	0.130	0.22535	11.27%	0.000
7	0.00862	1.26%	0.115	0.19698	9.85%	0.000
8	0.00680	0.99%	0.102	0.17498	8.75%	0.000
9	0.00551	0.80%	0.092	0.15740	7.87%	0.000
10	0.00455	0.66%	0.084	0.14304	7.15%	0.000
11	0.00382	0.56%	0.077	0.13109	6.55%	0.000
12	0.00326	0.47%	0.071	0.12098	6.05%	0.000

Table B.2: Maximum stable discrete-time parameters for $\gamma = 0.001$ and $\delta = 0$.

delay d	maximum stiffness			maximum damping		
	α_{\max}	$\frac{\alpha_{\max}}{\alpha_{\max} _{d=0}}$	$\beta _{\alpha_{\max}}$	β_{\max}	$\frac{\beta_{\max}}{\beta_{\max} _{d=0}}$	$\alpha _{\beta_{\max}}$
0	0.68576	100.00%	0.828	2.00017	100.00%	-0.001
1	0.14398	21.00%	0.424	0.82844	41.42%	-0.001
2	0.06195	9.03%	0.290	0.53569	26.78%	-0.001
3	0.03431	5.00%	0.221	0.39739	19.87%	-0.001
4	0.02169	3.16%	0.178	0.31610	15.80%	-0.001
5	0.01488	2.17%	0.149	0.26241	13.12%	-0.001
6	0.01079	1.57%	0.127	0.22422	11.21%	-0.001
7	0.00815	1.19%	0.111	0.19562	9.78%	-0.001
8	0.00634	0.92%	0.098	0.17338	8.67%	-0.001
9	0.00505	0.74%	0.088	0.15558	7.78%	-0.001
10	0.00409	0.60%	0.079	0.14098	7.05%	-0.001
11	0.00336	0.49%	0.072	0.12879	6.44%	-0.001
12	0.00280	0.41%	0.066	0.11845	5.92%	-0.001

Table B.3: Maximum stable discrete-time parameters for $\gamma = 0$ and $\delta = 0.02$.

delay d	maximum stiffness			maximum damping		
	α_{\max}	$\frac{\alpha_{\max}}{\alpha_{\max} _{d=0}}$	$\beta _{\alpha_{\max}}$	β_{\max}	$\frac{\beta_{\max}}{\beta_{\max} _{d=0}}$	$\alpha _{\beta_{\max}}$
0	0.71321	100.00%	0.824	2.02682	100.00%	0.000
1	0.15480	21.70%	0.423	0.84344	41.61%	0.000
2	0.06907	9.69%	0.291	0.54963	27.12%	0.000
3	0.03972	5.57%	0.222	0.41117	20.29%	0.000
4	0.02611	3.66%	0.180	0.32995	16.28%	0.000
5	0.01865	2.62%	0.152	0.27641	13.64%	0.000
6	0.01410	1.98%	0.131	0.23841	11.76%	0.000
7	0.01111	1.56%	0.116	0.21003	10.36%	0.000
8	0.00903	1.27%	0.103	0.18802	9.28%	0.000
9	0.00752	1.05%	0.094	0.17045	8.41%	0.000
10	0.00639	0.90%	0.086	0.15610	7.70%	0.000
11	0.00551	0.77%	0.079	0.14416	7.11%	0.000
12	0.00482	0.68%	0.073	0.13406	6.61%	0.000

Table B.4: Maximum stable discrete-time parameters for $\gamma = 0.001$ and $\delta = 0.02$.

delay d	maximum stiffness			maximum damping		
	α_{\max}	$\frac{\alpha_{\max}}{\alpha_{\max} _{d=0}}$	$\beta _{\alpha_{\max}}$	β_{\max}	$\frac{\beta_{\max}}{\beta_{\max} _{d=0}}$	$\alpha _{\beta_{\max}}$
0	0.71269	100.00%	0.824	2.02699	100.00%	-0.001
1	0.15433	21.65%	0.422	0.84346	41.61%	-0.001
2	0.06862	9.63%	0.290	0.54943	27.11%	-0.001
3	0.03928	5.51%	0.221	0.41074	20.26%	-0.001
4	0.02567	3.60%	0.178	0.32929	16.25%	-0.001
5	0.01822	2.56%	0.149	0.27553	13.59%	-0.001
6	0.01368	1.92%	0.128	0.23731	11.71%	-0.001
7	0.01069	1.50%	0.112	0.20870	10.30%	-0.001
8	0.00862	1.21%	0.100	0.18647	9.20%	-0.001
9	0.00712	1.00%	0.089	0.16868	8.32%	-0.001
10	0.00600	0.84%	0.081	0.15410	7.60%	-0.001
11	0.00513	0.72%	0.074	0.14193	7.00%	-0.001
12	0.00445	0.62%	0.068	0.13162	6.49%	-0.001

C

Tables for Optimal Control Design

This appendix contains value tables for the optimization criteria introduced in Chapter 5. Depending on time delay, different optimal parameter values result. This chapter contains values tables for delay factors $d \in \{0, 1, 2\}$.

C.1 No Delay ($d = 0$)

Table C.1: Optimal values for delay $d = 0$.

criterion	given parameters		resulting optimum		
	γ	δ	α_{opt}	β_{opt}	cost
α_{max}	0.000	0.00	0.6863	0.8283	–
	0.001	0.00	0.6858	0.8280	–
	0.000	0.02	0.7132	0.8244	–
	0.001	0.02	0.7127	0.8241	–
β_{max}	0.000	0.00	0.0000	2.0000	–
	0.001	0.00	–0.0010	2.0002	–
	0.000	0.02	0.0000	2.0268	–
	0.001	0.02	–0.0010	2.0270	–
O_{ζ}	0.000	0.00	0.0702	0.4054	1.000
	0.001	0.00	0.0693	0.4051	1.000
	0.000	0.02	0.0739	0.3991	1.000
	0.001	0.02	0.0730	0.3988	1.000
O_r	0.000	0.00	0.0703	0.4054	0.587
	0.001	0.00	0.0693	0.4052	0.587
	0.000	0.02	0.0740	0.3992	0.582
	0.001	0.02	0.0730	0.3989	0.582
O_{settle} with a 1% threshold	0.000	0.00	0.1521	0.5304	6.159
	0.001	0.00	0.1512	0.5302	6.157
	0.000	0.02	0.1590	0.5267	6.056
	0.001	0.02	0.1582	0.5265	6.054
O_{settle} with a 2% threshold	0.000	0.00	0.1771	0.5686	5.139
	0.001	0.00	0.1762	0.5685	5.137
	0.000	0.02	0.1850	0.5658	5.055
	0.001	0.02	0.1841	0.5656	5.053
O_{settle} with a 5% threshold	0.000	0.00	0.2303	0.6462	3.876
	0.001	0.00	0.2295	0.6460	3.875
	0.000	0.02	0.2400	0.6451	3.819
	0.001	0.02	0.2392	0.6449	3.817
O_{ov}	0.000	0.00	0.222	0.97	0.000
	0.001	0.00	0.221	0.97	0.000
	0.000	0.02	0.230	0.97	0.000
	0.001	0.02	0.230	0.97	0.000

	0.000	0.00	0.3220	0.9800	2.583
O_{E0}^{step}	0.001	0.00	0.3212	0.9798	2.582
	0.000	0.02	0.3341	0.9816	2.536
	0.001	0.02	0.3333	0.9815	2.535
	0.000	0.00	0.2816	0.8419	4.143
O_{E1}^{step}	0.001	0.00	0.2808	0.8417	4.140
	0.000	0.02	0.2922	0.8415	4.002
	0.001	0.02	0.2914	0.8413	3.999
	0.000	0.00	0.2474	0.7445	10.80
O_{E2}^{step}	0.001	0.00	0.2466	0.7443	10.79
	0.000	0.02	0.2569	0.7427	10.26
	0.001	0.02	0.2561	0.7425	10.25
	0.000	0.00	0.0001	0.9371	2.116
O_{E0}^{impulse}	0.001	0.00	-0.0010	0.9378	2.114
	0.000	0.02	0.0001	0.9371	2.051
	0.001	0.02	-0.0010	0.937	2.050
	0.000	0.00	0.1207	0.8371	5.611
O_{E1}^{impulse}	0.001	0.00	0.1198	0.8369	5.605
	0.000	0.02	0.1256	0.8359	5.368
	0.001	0.02	0.1247	0.8357	5.363
	0.000	0.00	0.1623	0.7592	20.37
O_{E2}^{impulse}	0.001	0.00	0.1615	0.7590	20.34
	0.000	0.02	0.1689	0.7572	19.18
	0.001	0.02	0.1680	0.7570	19.16
Ziegler-Nichols	0.000	0.00	0.270	0.900	-

C.2 One Sampling Step Delay ($d = 1$)

Table C.2: Optimal values for delay $d = 1$.

criterion	given parameters		resulting optimum		
	γ	δ	α_{opt}	β_{opt}	cost
α_{max}	0.000	0.00	0.1445	0.4247	–
	0.001	0.00	0.1440	0.4238	–
	0.000	0.02	0.1548	0.4227	–
	0.001	0.02	0.1543	0.4220	–
β_{max}	0.000	0.00	0.0000	0.8284	–
	0.001	0.00	–0.0010	0.8284	–
	0.000	0.02	0.0000	0.8434	–
	0.001	0.02	–0.0010	0.8435	–
O_{ζ}	0.000	0.00	0.0000	0.0000	1.000
	0.001	0.00	–0.0010	0.0000	1.000
	0.000	0.02	0.0000	0.0000	1.000
	0.001	0.02	–0.0009	0.0000	1.000
O_r	0.000	0.00	0.0191	0.2181	0.752
	0.001	0.00	0.0183	0.2174	0.752
	0.000	0.02	0.0211	0.2128	0.745
	0.001	0.02	0.0202	0.2120	0.744
O_{settle} with a 1% threshold	0.000	0.00	0.0391	0.2843	11.796
	0.001	0.00	0.0383	0.2836	11.774
	0.000	0.02	0.0426	0.2816	11.452
	0.001	0.02	0.0418	0.2810	11.431
O_{settle} with a 2% threshold	0.000	0.00	0.0449	0.3037	9.909
	0.001	0.00	0.0441	0.3032	9.890
	0.000	0.02	0.0487	0.3019	9.627
	0.001	0.02	0.0479	0.3013	9.610
O_{settle} with a 5% threshold	0.000	0.00	0.0566	0.3423	7.592
	0.001	0.00	0.0558	0.3417	7.579
	0.000	0.02	0.0611	0.3418	7.389
	0.001	0.02	0.0603	0.3413	7.377
O_{ov}	0.000	0.00	0.052	0.45	0.000
	0.001	0.00	0.051	0.45	0.000
	0.000	0.02	0.056	0.45	0.000
	0.001	0.02	0.055	0.45	0.000

	0.000	0.00	0.0702	0.4710	5.429
O_{E0}^{step}	0.001	0.00	0.0695	0.4705	5.419
	0.000	0.02	0.0753	0.4718	5.249
	0.001	0.02	0.0745	0.4713	5.240
	0.000	0.00	0.0642	0.4191	17.35
O_{E1}^{step}	0.001	0.00	0.0634	0.4185	17.29
	0.000	0.02	0.0688	0.4188	16.26
	0.001	0.02	0.0680	0.4182	16.21
	0.000	0.00	0.0582	0.3796	87.44
O_{E2}^{step}	0.001	0.00	0.0574	0.3790	86.97
	0.000	0.02	0.0625	0.3786	79.40
	0.001	0.02	0.0618	0.3778	79.06
	0.000	0.00	0.0000	0.4450	4.277
O_{E0}^{impulse}	0.001	0.00	-0.0010	0.4442	4.265
	0.000	0.02	0.0000	0.4446	4.018
	0.001	0.02	-0.0010	0.4439	4.007
	0.000	0.00	0.0293	0.4113	22.66
O_{E1}^{impulse}	0.001	0.00	0.0284	0.4106	22.56
	0.000	0.02	0.0317	0.4104	20.75
	0.001	0.02	0.0308	0.4097	20.66
	0.000	0.00	0.0396	0.3823	162.1
O_{E2}^{impulse}	0.001	0.00	0.0387	0.3817	161.1
	0.000	0.02	0.0427	0.3809	144.3
	0.001	0.02	0.0418	0.3802	143.4
Ziegler-Nichols	0.000	0.00	0.056	0.373	-

C.3 Two Sampling Steps Delay ($d = 2$)

Table C.3: Optimal values for delay $d = 2$.

criterion	given parameters		resulting optimum		
	γ	δ	α_{opt}	β_{opt}	cost
α_{max}	0.000	0.00	0.0624	0.2914	–
	0.001	0.00	0.0620	0.2902	–
	0.000	0.02	0.0691	0.2906	–
	0.001	0.02	0.0686	0.2895	–
β_{max}	0.000	0.00	0.0000	0.5359	–
	0.001	0.00	–0.0010	0.5357	–
	0.000	0.02	0.0000	0.5496	–
	0.001	0.02	–0.0010	0.5494	–
O_{ζ}	0.000	0.00	0.0000	0.0000	1.000
	0.001	0.00	–0.0010	0.0000	0.852
	0.000	0.02	0.0000	–0.0200	1.000
	0.001	0.02	–0.0008	0.0000	0.857
O_r	0.000	0.00	0.0087	0.1485	0.825
	0.001	0.00	0.0078	0.1472	0.824
	0.000	0.02	0.0100	0.1435	0.817
	0.001	0.02	0.0091	0.1423	0.816
O_{settle} with a 1% threshold	0.000	0.00	0.0175	0.1938	17.55
	0.001	0.00	0.0167	0.1927	17.48
	0.000	0.02	0.0198	0.1916	16.80
	0.001	0.02	0.0190	0.1906	16.73
O_{settle} with a 2% threshold	0.000	0.00	0.0200	0.2071	14.77
	0.001	0.00	0.0192	0.2060	14.70
	0.000	0.02	0.0225	0.2056	14.16
	0.001	0.02	0.0217	0.2046	14.10
O_{settle} with a 5% threshold	0.000	0.00	0.0251	0.2332	11.35
	0.001	0.00	0.0243	0.2322	11.30
	0.000	0.02	0.0280	0.2332	10.90
	0.001	0.02	0.0273	0.2323	10.86
O_{ov}	0.000	0.00	0.023	0.30	0.000
	0.001	0.00	0.022	0.30	0.000
	0.000	0.02	0.046	0.32	0.000
	0.001	0.02	0.025	0.30	0.000

	0.000	0.00	0.0305	0.3155	8.214
O_{E0}^{step}	0.001	0.00	0.0298	0.3145	8.180
	0.000	0.02	0.0338	0.3167	7.815
	0.001	0.02	0.0330	0.3157	7.785
	0.000	0.00	0.0280	0.2822	39.38
O_{E1}^{step}	0.001	0.00	0.0273	0.2812	39.06
	0.000	0.02	0.0311	0.2823	35.81
	0.001	0.02	0.0303	0.2813	35.53
	0.000	0.00	0.0256	0.2566	296.2
O_{E2}^{step}	0.001	0.00	0.0248	0.2556	292.5
	0.000	0.02	0.0284	0.2559	257.4
	0.001	0.02	0.0277	0.2549	254.4
	0.000	0.00	0.0000	0.2938	6.430
O_{E0}^{impulse}	0.001	0.00	-0.0010	0.2926	6.397
	0.000	0.02	0.0000	0.2933	5.858
	0.001	0.02	-0.0010	0.2922	5.822
	0.000	0.00	0.0130	0.2746	51.12
O_{E1}^{impulse}	0.001	0.00	0.0121	0.2735	50.59
	0.000	0.02	0.0145	0.2740	44.86
	0.001	0.02	0.0137	0.2728	44.42
	0.000	0.00	0.0175	0.2569	547.7
O_{E2}^{impulse}	0.001	0.00	0.0166	0.2558	539.7
	0.000	0.02	0.0196	0.2559	460.7
	0.001	0.02	0.0187	0.2548	454.4
Ziegler-Nichols	0.000	0.00	0.024	0.241	-

D

Experimental Results

This appendix contains value tables for the optimal points of the experiments described in Chapter 6. In these tables, it also shows the optimal points that would result for the cost functions based on the continuous-time position.

D.1 Falcon

Table D.1: Numerical values of the optimum points of Fig. 6.5.

criterion	condition	stiffness K	damping B	costs C
O_{settle}	theoretical optimum for C_{settle}^*	4469 N/m	73.05 Ns/m	24.00 ^a
	theoretical optimum for C_{settle}	4478 N/m	73.16 Ns/m	23.93
	experiment 1	5200 N/m	64 Ns/m	20.00
	experiment 2	4000 N/m	56 Ns/m	23.00
O_{ov}	theoretical optimum for C_{ov}^*	5109 N/m	106.57 Ns/m	0
	theoretical optimum for C_{ov}	5056 N/m	104.70 Ns/m	0
	experiment 1	6800 N/m	116 Ns/m	0
	experiment 2	6600 N/m	128 Ns/m	0

^aThe discrete-time optimization criterion C_{settle}^* results in an optimal region instead of an optimal point. The given values indicate the center point of the bounding box of this optimal region, which is ranging from $(K, B) = (4464 \text{ N/m}, 73.00 \text{ Ns/m})$ to $(K, B) = (4474 \text{ N/m}, 73.11 \text{ Ns/m})$.

Table D.2: Numerical values of the optimum points of Fig. 6.6.

criterion	condition	stiffness K	damping B	costs C_{Ew}
O_{E0}^{step}	theoretical optimum for C_{E0}^*	6689 N/m	111.18 Ns/m	13.84
	theoretical optimum for C_{E0}	6682 N/m	111.11 Ns/m	13.36
	experiment 1	4600 N/m	104 Ns/m	8.87
	experiment 2	5800 N/m	96 Ns/m	10.94
O_{E1}^{step}	theoretical optimum for C_{E1}^*	6154 N/m	99.70 Ns/m	106.57
	theoretical optimum for C_{E1}	6164 N/m	99.50 Ns/m	104.00
	experiment 1	8400 N/m	104 Ns/m	64.68
	experiment 2	5800 N/m	96 Ns/m	76.98
O_{E2}^{step}	theoretical optimum for C_{E2}^*	5645 N/m	90.79 Ns/m	1329.84
	theoretical optimum for C_{E2}	5645 N/m	90.49 Ns/m	1266.74
	experiment 1	6000 N/m	80 Ns/m	726.10
	experiment 2	5800 N/m	96 Ns/m	918.38

Table D.3: Numerical values of the optimum points of Fig. 6.7.

criterion	condition	stiffness K	damping B	costs C_{Ew}^{step}
O_{settle}	theoretical optimum for C_{settle}^*	9863 N/m	125.09 Ns/m	22.00 ^a
	theoretical optimum for C_{settle}	9879 N/m	125.26 Ns/m	21.94
	experiment 6	9200 N/m	140 Ns/m	36.00
	experiment 7	8000 N/m	100 Ns/m	35.00
O_{ov}	theoretical optimum for C_{ov}^*	10933 N/m	182.74 Ns/m	0
	theoretical optimum for C_{ov}	10813 N/m	179.80 Ns/m	0
	experiment 6	8800 N/m	140 Ns/m	0
	experiment 7	9200 N/m	100 Ns/m	0
O_{E2}^{step}	theoretical optimum for C_{E2}^*	12111 N/m	156.56 Ns/m	997.43
	theoretical optimum for C_{E2}	12113 N/m	155.99 Ns/m	946.83
	experiment 6	14400 N/m	140 Ns/m	863.24
	experiment 7	9200 N/m	100 Ns/m	703.60

^aThe discrete-time optimization criterion C_{settle}^* results in an optimal region instead of an optimal point. The given values indicate the center point of the bounding box of this optimal region, which is ranging from $(K, B) = (9847 \text{ N/m}, 124.91 \text{ Ns/m})$ to $(K, B) = (9880 \text{ N/m}, 125.26 \text{ Ns/m})$.

D.2 LWR

Table D.4: Numerical values of the optimum points of Fig. 6.10.

criterion	condition	stiffness K_{rot}	damping B_{rot}	costs C
O_{settle}	theoretical optimum for C_{settle}^*	3742 Nm/rad	38.96 Nms/rad	15.00 ^a
	theoretical optimum for C_{settle}	3798 Nm/rad	39.34 Nms/rad	14.77
	LWR	3200 Nm/rad	18 Nms/rad	15
O_{ov}	theoretical optimum for C_{ov}^*	4430 Nm/rad	57.39 Nms/rad	0
	theoretical optimum for C_{ov}	4358 Nm/rad	56.29 Nms/rad	0
	LWR	2000 Nm/rad	25 Nms/rad	0

^aThe discrete-time optimization criterion C_{settle}^* results in an optimal region instead of an optimal point. The given values indicate the center point of the bounding box of this optimal region, which is ranging from $(K, B) = (3725 \text{ Nm/rad}, 38.85 \text{ Nms/rad})$ to $(K, B) = (3760 \text{ Nm/rad}, 39.07 \text{ Nms/rad})$.

Table D.5: Numerical values of the optimum points of Fig. 6.11.

criterion	condition	stiffness K_{rot}	damping B_{rot}	costs C_{Ew}
O_{E0}^{step}	theoretical optimum for C_{E0}^*	5813 Nm/rad	60.04 Nms/rad	8.69
	theoretical optimum for C_{E0}	5796 Nm/rad	59.94 Nms/rad	8.21
	LWR	4400 Nm/rad	25 Nms/rad	10.51
O_{E1}^{step}	theoretical optimum for C_{E1}^*	5319 Nm/rad	53.84 Nms/rad	40.88
	theoretical optimum for C_{E1}	5328 Nm/rad	53.62 Nms/rad	39.38
	LWR	4600 Nm/rad	23 Nms/rad	55.36
O_{E2}^{step}	theoretical optimum for C_{E2}^*	4865 Nm/rad	49.05 Nms/rad	320.08
	theoretical optimum for C_{E2}	4861 Nm/rad	48.76 Nms/rad	296.18
	LWR	4400 Nm/rad	22 Nms/rad	440.38

Table D.6: Numerical values of the optimum points of Fig. 6.12.

delay	theoretical optimal costs				experimental optimal costs				relative deviation			
d	C_{settle}^*	C_{E0}^*	C_{E1}^*	C_{E2}^*	C_{settle}^*	C_{E0}^*	C_{E1}^*	C_{E2}^*	C_{settle}^*	C_{E0}^*	C_{E1}^*	C_{E2}^*
2	15	8.69	40.9	320.1	15	10.5	55.4	440.4	0.0%	20.9%	35.4%	37.6%
3	20	11.5	72.3	745.8	16	12.2	75.6	687.5	-20.0%	6.6%	4.5%	-7.8%
4	25	14.2	113	1441	21	14.9	110	1203	-16.0%	4.6%	-2.5%	-16.5%
5	30	17.0	162	2472	23	17.4	154	2019	-23.3%	2.4%	-4.6%	-18.3%
6	35	19.8	220	3904	32	20.0	209	3221	-8.8%	1.1%	-4.8%	-17.5%
7	40	22.5	286	5804	41	22.6	274	4882	2.5%	0.4%	-4.1%	-15.9%
8	45	25.3	362	8238	38	25.8	355	7583	-15.6%	2.2%	-1.8%	-8.0%

E

Electrical Analogon

This appendix shows in Fig. E.1 the electrical analogical model of the mechanical system that is considered in this thesis. It also shows the dual network of the electrical analogical model. This figure should emphasize the fact that the theoretical investigations and findings hold for any dynamically analogical system [13, 63].

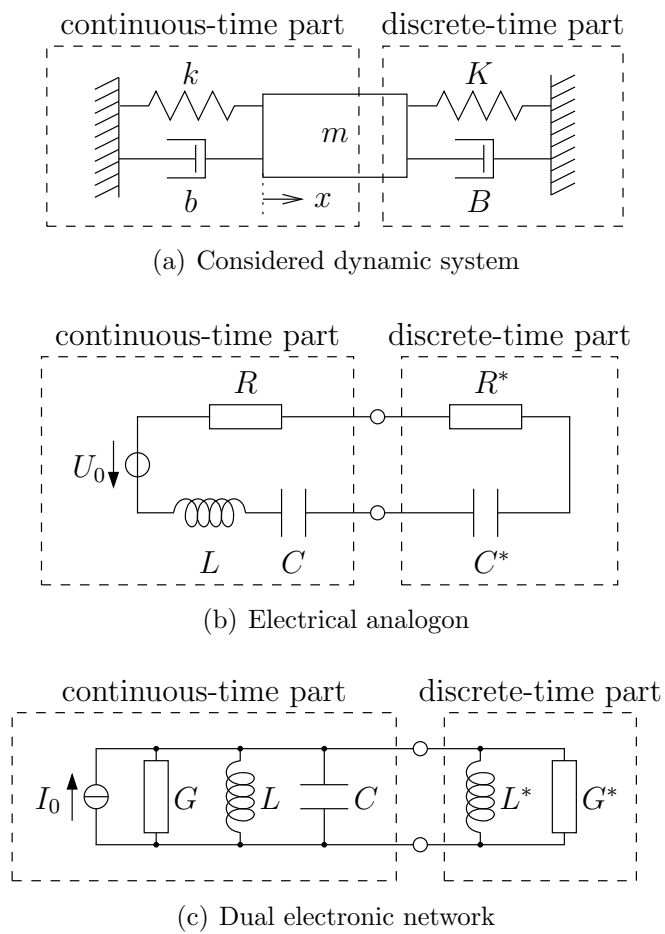


Figure E.1: Dynamical analogies: (a) the mechanical haptic system, (b) its electrical analogon, and (c) the dual electronic network.

Bibliography

- [1] K. J. Åström and R. M. Murray. *Feedback Systems: An Introduction for Scientists and Engineers*. Princeton University Press, September 2012.
- [2] K. J. Åström and B. Wittenmark. *Computer-Controlled Systems: Theory and Design*. Prentice Hall, 3rd edition, 1997.
- [3] K. J. Åström and B. Wittenmark. *Adaptive Control*. Addison-Wesley, 2nd edition, 2008.
- [4] J. J. Abbott and A. M. Okamura. Effects of position quantization and sampling rate on virtual-wall passivity. *IEEE Trans. on Robotics*, 21(5):952–964, October 2005.
- [5] J. Ackermann. *Sampled-Data Control Systems: Analysis and Synthesis, Robust System Design*. Springer Science & Business Media, 2012.
- [6] J. Ackermann, P. Blue, T. Bünte, L. Güvenc, D. Kaesbauer, M. Kordt, M. Muhler, and D. Odenthal. *Robust Control: The Parameter Space Approach*. Communications and Control Engineering Series. Springer-Verlag GmbH, 2002.
- [7] R. J. Adams and B. Hannaford. Stable haptic interaction with virtual environments. *IEEE Trans. on Robotics and Automation*, 15(3):465–474, June 1999.
- [8] R. J. Adams and B. Hannaford. Control law design for haptic interfaces to virtual reality. *IEEE Trans. on Control Systems Technology*, 10(1):3–13, January 2002.
- [9] N. Bajcinca and T. Hulin. RobSin: A new tool for robust design of pid and three-term controllers based on singular frequencies. In *IEEE Int. Conf. on Control Applications*, volume 2, pages 1546–1551. IEEE, 2004.
- [10] N. Bajcinca and T. Hulin. Menge aller robust stabilisierenden PID-Regler: Methodik und Software (Teil I–III). *at - Automatisierungstechnik*, 2005–2006.
- [11] C. Basdogan and M. A. Srinivasan. Haptic rendering in virtual environments. In K.M. Stanney, editor, *Handbook of Virtual Environments: Design, Implementation, and Applications*, pages 117–134. Erlbaum, 2002.

- [12] A. Bicchi, M. Buss, M.O. Ernst, and A. Peer. *The Sense of Touch and its Rendering: Progress in Haptics Research*. Springer, Berlin, Germany, 2008.
- [13] A. Bloch. Electromechanical analogies and their use for the analysis of mechanical and electromechanical systems. *Electrical Engineers - Part I: General, Journal of the Institution of*, 92(52):157–169, April 1945.
- [14] T. L. Brooks. Telerobotic response requirements. In *IEEE Trans. on Systems, Man, and Cybernetics*, pages 113–120, Los Angeles, CA, November 1990.
- [15] J. Buchli, F. Stulp, E. Theodorou, and S. Schaal. Learning variable impedance control. *The Int. Journal of Robotics Research*, 30(7):820–833, November 2011.
- [16] M. C. Cavusoglu, D. Feygin, and F. Tendick. A critical study of the mechanical and electrical properties of the PHANToM haptic interface and improvements for high performance control. *Presence*, 11(6):555–568, 2002.
- [17] V. Chawda, O. Celik, and M. K. O'Malley. A method for selecting velocity filter cut-off frequency for maximizing impedance width performance in haptic interfaces. *ASME Journal of Dynamic Systems, Measurement, and Control*, 137(2):024503, February 2015.
- [18] J. Y. C. Chen and J. E. Thropp. Review of low frame rate effects on human performance. *IEEE Trans. on Systems, Man, and Cybernetics*, 37(6):1063–1076, 2007.
- [19] D. Christiansen and C. Alexander. *Standard Handbook of Electronic Engineering*. McGraw-Hill Education, 5th edition, 2005.
- [20] P. Ciáurriz, I. Díaz, and J. J. Gil. Stable discrete-time impedances for haptic systems with vibration modes and delay. *IEEE Trans. on Control Systems Technology*, 22(3):884–895, May 2014.
- [21] J. E. Colgate and J. M. Brown. Factors affecting the z-width of a haptic display. In *IEEE Int. Conf. on Robotics and Automation (ICRA)*, pages 3205–3210, May 1994.
- [22] J. E. Colgate and N. Hogan. An analysis of contact instability in terms of passive physical equivalents. In *IEEE Int. Conf. on Robotics and Automation (ICRA)*, pages 404–409, Scottsdale, AZ, USA, May 1989.
- [23] J. E. Colgate and G. Schenkel. Passivity of a class of sampled-data systems: Application to haptic interfaces. In *1994 American Control Conference*, pages 37–47. AIAA, 1994.

- [24] J. E. Colgate and G. Schenkel. Passivity of a class of sampled-data systems: Application to haptic interfaces. *Journal of Robotic Systems*, 14(1):37–47, January 1997.
- [25] J. E. Colgate, M. C. Stanley, and J. M. Brown. Issues in the haptic display of tool use. In *IEEE/RSJ Int. Conf. on Intelligent Robots and Systems (IROS)*, volume 3, pages 140–145, Pittsburgh, PA, USA, Aug 1995.
- [26] J. J. Craig. *Introduction to Robotics Mechanics and Control*. Addison-Wesley Publishing Company, Inc., USA, 2nd edition, 1989.
- [27] Q. V. Dang, A. Dequidt, L. Vermeiren, and M. Dambrine. Experimental study on stability of a haptic system with variable time delays. In *IEEE/ASME Int. Conf. on Advanced Intelligent Mechatronics (AIM)*, pages 554–559, July 2014.
- [28] Q. V. Dang, L. Vermeiren, A. Dequidt, and M. Dambrine. Analyzing stability of haptic interface using linear matrix inequality approach. In *IEEE Int. Conf. on Robotics and Biomimetics*, pages 1129–1134, December 2012.
- [29] R. W. Daniel and P. R. McAree. Fundamental limits of performance for force reflecting teleoperation. *The Int. Journal of Robotics Research*, 17(8):811–830, August 1998.
- [30] I. Díaz and J. J. Gil. Influence of internal vibration modes on the stability of haptic rendering. In *IEEE Int. Conf. on Robotics and Automation (ICRA)*, pages 2884–2889, Pasadena, CA, May 2008.
- [31] I. Díaz, J. J. Gil, and T. Hulin. *Advances in Haptics*, chapter Stability Boundary and Transparency for Haptic Rendering, pages 103–125. INTECH, 2010.
- [32] I. Diaz and J.J. Gil. Influence of vibration modes and human operator on the stability of haptic rendering. *IEEE Trans. on Robotics*, 26(1):160–165, February 2010.
- [33] N. Diolaiti, G. Niemeyer, F. Barbagli, and J. K. Salisbury. Stability of haptic rendering: Discretization, quantization, time delay, and coulomb effects. *IEEE Trans. on Robotics*, 22(2):256–268, April 2006.
- [34] G. F. Franklin, J. D. Powell, and M. L. Workman. *Digital Control of Dynamic Systems*. Addison-Wesley, Menlo Park, 3rd edition, 1998.
- [35] J. J. Gil, A. Avello, Á. Rubio, and J. Flórez. Stability analysis of a 1 DOF haptic interface using the Routh-Hurwitz criterion. *IEEE Trans. on Control Systems Technology*, 12(4):583–588, July 2004.

- [36] J. J. Gil, E. Sánchez, T. Hulin, C. Preusche, and G. Hirzinger. Stability boundary for haptic rendering: Influence of damping and delay. In *IEEE Int. Conf. on Robotics and Automation (ICRA)*, Rome, Italy, April 2007.
- [37] J. J. Gil, E. Sánchez, T. Hulin, C. Preusche, and G. Hirzinger. Stability boundary for haptic rendering: Influence of damping and delay. *Journal of Computing and Information Science in Engineering*, 9(1):011005–1–011005–8, March 2009.
- [38] R. B. Gillespie and M. R. Cutkosky. Stable user-specific haptic rendering of the virtual wall. In *1996 International Mechanical Engineering Congress and Exhibition*, volume 58, pages 397–406, Atlanta, November 1996.
- [39] A. H. C. Gosline and V. Hayward. Time-domain passivity control of haptic interfaces with tunable damping hardware. In *IEEE World Haptics Conference (WHC)*, pages 164–169, March 2007.
- [40] D. Graham and R. C. Lathrop. The synthesis of optimum transient response: Criteria and standard forms. *Trans. of the AIEE, Part II: Applications and Industry*, 72(5):273–288, November 1953.
- [41] G. Habib, G. Rega, and G. Stepan. Stability analysis of a two-degree-of-freedom mechanical system subject to proportional–derivative digital position control. *Journal of Vibration and Control*, 21(8):1539–1555, April 2015.
- [42] B. Hannaford and J.-H. Ryu. Time-domain passivity control of haptic interfaces. *IEEE Trans. on Robotics and Automation*, 18(1):1–10, February 2002.
- [43] V. Hayward, O. R. Astley, M. Cruz-Hernandez, D. Grant, and G. Robles-De-La-Torre. Haptic interfaces and devices. *Sensor Review*, 24(1):16–29, 2004.
- [44] V. Hayward and K. E. MacLean. Do it yourself haptics, part-i. *IEEE Robotics and Automation Magazine*, 14(4):88–104, December 2007.
- [45] K. Hertkorn, T. Hulin, P. Kremer, C. Preusche, and G. Hirzinger. Time domain passivity control for multi-degree of freedom haptic systems with time delay. In *IEEE Int. Conf. on Robotics and Automation (ICRA)*, pages 1313–1319, Anchorage, Alaska, USA, May 2010.
- [46] G. Hirzinger, N. Sporer, M. Schedl, J. Butterfaß, and M. Grebenstein. Torque-controlled lightweight arms and articulated hands: Do we reach technological limits now? *The Int. Journal of Robotics Research*, 23(4-5):331–340, June 2004.
- [47] N. Hogan. Controlling impedance at the man/machine interface. In *IEEE Int. Conf. on Robotics and Automation (ICRA)*, volume 3, pages 1626–1631, Scottsdale, AZ, USA, May 1989.

- [48] T. Hulin, A. Albu-Schäffer, and G. Hirzinger. Passivity and stability boundaries for haptic systems with time delay. *IEEE Trans. on Control Systems Technology*, 22(4):1297–1309, July 2014.
- [49] T. Hulin, J. J. Gil, E. Sánchez, C. Preusche, and G. Hirzinger. Experimental stability analysis of a haptic system. In *Int. Conf. on Enactive Interfaces*, pages 157–158, Montpellier, France, November 2006.
- [50] T. Hulin, R. González Camarero, and A. Albu-Schäffer. Optimal control for haptic rendering: Fast energy dissipation and minimum overshoot. In *IEEE/RSJ Int. Conf. on Intelligent Robots and Systems (IROS)*, pages 4505–4511, Tokyo, Japan, November 2013.
- [51] T. Hulin, K. Hertkorn, P. Kremer, S. Schätzle, J. Artigas, M. Sagardia, F. Zacharias, and C. Preusche. The DLR bimanual haptic device with optimized workspace. In *IEEE Int. Conf. on Robotics and Automation (ICRA)*, pages 3441–3442, Shanghai, China, May 2011.
- [52] T. Hulin, K. Hertkorn, and C. Preusche. Interactive features for robot viewers. In *Int. Conf. on Intelligent Robotics and Applications (ICIRA)*, pages 181–193, Montreal, Canada, October 2012.
- [53] T. Hulin, C. Preusche, and G. Hirzinger. Haptic rendering for virtual assembly verification (poster). In *IEEE World Haptics Conference (WHC)*, Pisa, Italy, March 2005.
- [54] T. Hulin, C. Preusche, and G. Hirzinger. Stability boundary and design criteria for haptic rendering of virtual walls. In *Int. IFAC Symp. on Robot Control (SYROCO)*, Bologna, Italy, September 2006.
- [55] T. Hulin, C. Preusche, and G. Hirzinger. Stability boundary for haptic rendering: Influence of physical damping. In *IEEE/RSJ Int. Conf. on Intelligent Robots and Systems (IROS)*, pages 1570–1575, Beijing, China, October 2006.
- [56] T. Hulin, C. Preusche, and G. Hirzinger. Stability boundary for haptic rendering: Influence of human operator. In *IEEE/RSJ Int. Conf. on Intelligent Robots and Systems (IROS)*, pages 3483–3488, Nice, France, September 2008.
- [57] T. Hulin, C. Preusche, E. Yechiam, A. Telpaz, V. Schmirgel, and U. E. Zimmermann. Haptic and visual training of system behavior—a case study for robotic programming-by-demonstration. In *The International SKILLS Conference*, Montpellier, France, December 2011.
- [58] T. Hulin, M. Sagardia, J. Artigas, S. Schätzle, P. Kremer, and C. Preusche. Human-scale bimanual haptic interface. In *Int. Conf. on Enactive Interfaces*, pages 28–33, Pisa, Italy, November 2008.

- [59] T. Hulin, V. Schmirgel, E. Yechiam, U. E. Zimmermann, C. Preusche, and G. Pöhler. Evaluating exemplary training accelerators for programming-by-demonstration. In *IEEE Int. Symp. in Robot and Human Interactive Communication (Ro-Man)*, pages 467–472, Viareggio, Italy, September 2010.
- [60] R. Iskakov, A. Albu-Schäffer, M. Schedl, G. Hirzinger, and V. Lopota. Influence of sensor quantization on the control performance of robotics actuators. In *IEEE/RSJ Int. Conf. on Intelligent Robots and Systems (IROS)*, pages 1085–1092, San Diego, CA, USA, October 2007.
- [61] E. I. Jury. *Sampled-Data Control Systems*. John Wiley & Sons, 1958.
- [62] H. Kazerooni, T.-I. Tsay, and K. Hollerbach. A controller design framework for telerobotic systems. *IEEE Trans. on Control Systems Technology*, 1(1):50–62, March 1993.
- [63] T. A. Kern, M. Matysek, J. Rausch, A. Rettig, A. Röse, O. Meckel, and S. Sindlinger. *Engineering Haptic Devices: A Beginner's Guide for Engineers*. Springer, 2009.
- [64] R. Konietzschke, A. Tobergte, C. Preusche, P. Tripicchio, E. Ruffaldi, S. Webel, and U. Bockholt. A multimodal training platform for minimally invasive robotic surgery. In *IEEE Int. Symp. in Robot and Human Interactive Communication (Ro-Man)*, pages 422–427, Viareggio, Italy, September 2010.
- [65] R. Kories and H. Schmidt-Walter. *Taschenbuch der Elektrotechnik: Grundlagen und Elektronik*. Harri Deutsch, 2000.
- [66] K. Kosuge, Y. Fujisawa, and T. Fukuda. Mechanical system control with man-machine-environment interactions. In *IEEE Int. Conf. on Robotics and Automation (ICRA)*, pages 239–244, May 1993.
- [67] K. J. Kuchenbecker, J. G. Park, and G. Niemeyer. Characterizing the human wrist for improved haptic interaction. In *ASME Int. Mechanical Engineering Congress and Exposition*, volume 72, pages 591–598, Washington, DC, USA, November 2003.
- [68] A. Kugi. Nichtlineare Systeme I – Vorlesung und Übung. Technical report, Johannes Kepler University Linz, 2013.
- [69] D. Lakatos, F. Petit, and P. van der Smagt. Conditioning vs. excitation time for estimating impedance parameters of the human arm. In *IEEE-RAS Int. Conf. on Humanoid Robots (Humanoids)*, volume 11, pages 636–642, Bled, Slovenia, October 2011.
- [70] D. A. Lawrence. Stability and transparency in bilateral teleoperation. *IEEE Trans. on Robotics and Automation*, 9(5):624–637, October 1993.

- [71] D. A. Lawrence and J. D. Chapel. Performance trade-offs for hand controller design. In *IEEE Int. Conf. on Robotics and Automation (ICRA)*, volume 4, pages 3211–3216, San Diego, CA, USA, May 1994.
- [72] S. J. Lederman and R. L. Klatzky. Haptic perception: A tutorial. *Attention, Perception, & Psychophysics*, 71(7):1439–1459, 2009.
- [73] S. Lee and H. Lee. Modeling, design, and evaluation of advanced teleoperator control systems with short time delay. *IEEE Trans. on Robotics and Automation*, 9(5):607–623, October 1993.
- [74] J. E. Luntz, T. R. Kurfess, and M. L. Nagurka. Explicit parameter dependency in digital control systems. In *ASME Winter Annual Meeting*, New Orleans, LA, November 1993.
- [75] H. Lutz and W. Wendt. *Taschenbuch der Regelungstechnik*. Harri Deutsch, 2005.
- [76] A. Magana. Stability analysis for a surgical simulator. Diploma thesis, Dresden University of Technology, December 2013.
- [77] S. Martin and N. Hillier. Characterisation of the Novint Falcon haptic device for application as a robot manipulator. In *Australasian Conf. on Robotics and Automation (ACRA)*, December 2009.
- [78] J. Mehling, J. E. Colgate, and M. A. Peshkin. Increasing the impedance range of a haptic display by adding electrical damping. In *IEEE World Haptics Conference (WHC)*, pages 257–262, Pisa, Italy, March 2005.
- [79] N. Miandashti and M. Tavakoli. Stability of sampled-data, delayed haptic interaction and teleoperation. In *IEEE Haptics Symp.*, pages 215–220, Houston, Texas, USA, February 2014.
- [80] B. E. Miller, J. E. Colgate, and R. A. Freeman. Guaranteed stability of haptic systems with nonlinear virtual environments. *IEEE Trans. on Robotics and Automation*, 16(6):712–719, December 2000.
- [81] M. Minsky, M. Ouh-young, O. Steele, F. Brooks Jr., and M. Behensky. Feeling and seeing: Issues in force display. *ACM SIGGRAPH Computer Graphics*, 24(2):235–243, March 1990.
- [82] S. Moberg, J. Öhr, and S. Gunnarsson. A benchmark problem for robust feedback control of a flexible manipulator. *IEEE Trans. on Control Systems Technology*, 17(6):1398–1405, November 2009.
- [83] C. A. Monje, Y. Chen, B. M. Vinagre, D. Xue, and V. Feliu-Batlle. *Fractional-order systems and controls: fundamentals and applications*. Springer, 2010.

- [84] F. A. Mussa-Ivaldi, N. Hogan, and E. Bizzi. Neural, mechanical, and geometric factors subserving arm posture in humans. *The Journal of Neuroscience*, 5(10):2732–2743, October 1985.
- [85] K. Ogata. *Modern Control Engineering*. Prentice Hall, 5th edition, 2010.
- [86] M. K. O’Malley and A. Gupta. *HCI Beyond the GUI: Design for Haptic, Speech, Olfactory, and Other Nontraditional Interfaces*, volume 1, chapter Haptic Interfaces, pages 25–73. Elsevier Inc., USA, 2008.
- [87] M. Ortega, S. Redon, and S. Coquillart. A six degree-of-freedom god-object method for haptic display of rigid bodies with surface properties. *IEEE Trans. on Visualization and Computer Graphics*, 13(3):458–469, May 2007.
- [88] R. Ortega, A. J. van der Schaft, I. Mareels, and B. Maschke. Putting energy back in control. *IEEE Control Systems Magazine*, 21(2):18–33, April 2001.
- [89] Ch. Ott, J. Artigas, and C. Preusche. Subspace-oriented energy distribution for the time domain passivity approach. In *IEEE/RSJ Int. Conf. on Intelligent Robots and Systems (IROS)*, pages 665–671, San Francisco, CA, USA, September 2011.
- [90] N. Paine and L. Sentis. A closed-form solution for selecting maximum critically damped actuator impedance parameters. *ASME Journal of Dynamic Systems, Measurement, and Control*, 137(4):041011, April 2015.
- [91] C. Preusche, T. Hulin, and G. Hirzinger. *Human Haptic Perception: Basics and Applications*, chapter 33: Haptic rendering and control. Birkhäuser Basel, 1st edition, October 2008.
- [92] D. C. Ruspini, K. Kolarov, and O. Khatib. The haptic display of complex graphical environments. In *ACM SIGGRAPH Computer Graphics*, pages 345–352, Los Angeles, CA, USA, August 1997.
- [93] J.-H. Ryu, C. Preusche, B. Hannaford, and G. Hirzinger. Time domain passivity control with reference energy behavior. *IEEE Trans. on Control Systems Technology*, 13(5):737–742, September 2005.
- [94] M. Sagardia, K. Hertkorn, T. Hulin, Simon Schätzle, R. Wolff, J. Hummel, J. Dodiya, and A. Gerndt. VR-OOS: The DLR’s virtual reality simulator for telerobotic on-orbit servicing with haptic feedback. In *IEEE Aerospace Conference*, Big Sky, Montana, USA, March 2015.
- [95] M. Sagardia, K. Hertkorn, T. Hulin, R. Wolff, J. Hummel, J. Dodiya, and A. Gerndt. An interactive virtual reality system for on-orbit servicing. In *IEEE Virtual Reality Conference*, March 2013. (Video).

- [96] M. Sagardia and T. Hulin. Fast and accurate distance, penetration, and collision queries using point-sphere trees and distance fields. In *ACM SIGGRAPH Computer Graphics*, page 83, Anaheim, CA, USA, July 2013.
- [97] M. Sagardia, T. Hulin, C. Preusche, and G. Hirzinger. Improvements of the voxmap pointshell algorithm — fast generation of haptic data structures. In *53rd IWK - Internationales Wissenschaftliches Kolloquium*, Ilmenau, Germany, September 2008.
- [98] M. Sagardia, T. Stouraitis, and J. L. e Silva. A new fast and robust collision detection and force computation algorithm applied to the physics engine Bullet: Method, integration, and evaluation. In *EuroVR*, pages 65–76, Bremen, Germany, December 2014.
- [99] S. E. Salcudean and T. D. Vlaar. On the emulation of stiff walls and static friction with a magnetically levitated input/output device. *ASME Journal of Dynamic Systems, Measurement, and Control*, 119(1):127–132, March 1997.
- [100] K. Salisbury, D. Brock, T. Massie, N. Swarup, and C. Zilles. Haptic rendering: programming touch interaction with virtual objects. In *SI3D '95: Symp. on Interactive 3D graphics*, pages 123–130, Monterey, California, United States, 1995.
- [101] K. Salisbury, F. Conti, and F. Barbagli. Haptic rendering: Introductory concepts. *IEEE Computer Graphics and Applications*, 24(2):24–32, 2004.
- [102] S. Schätzle, T. Hulin, C. Preusche, and G. Hirzinger. Evaluation of vibro-tactile feedback to the human arm. In *EuroHaptics*, pages 557–560, Paris, France, July 2006.
- [103] M. E. Schlarmann and R. L. Geiger. Relationship between amplifier settling time and pole-zero placements for second-order systems. In *IEEE Midwest Symp. on Circuits and Systems*, volume 1, pages 54–59, Lansing, MI, USA, August 2000.
- [104] V. Schmirgel, U. E. Zimmermann, T. Hulin, and C. Preusche. *beyond movement*, chapter Position Paper: Human Skills for Programming-by-Demonstration of Robots, pages 144–167. Alinea editrice s.r.l., November 2008.
- [105] V. Schmirgel, U. E. Zimmermann, E. Yechiam, T. Hulin, and C. Preusche. Comprehension of operating a robot by enactive learning: Exemplary approaches with programming-by-demonstration. In *SKILLS09 Int. Conf. on Multimodal Interfaces for Skills Transfer*, Bilbao, Spain, December 2009.
- [106] V. Schmirgel, U. E. Zimmermann, E. Yechiam, A. Telpaz, T. Hulin, and C. Preusche. *Skill Training in Multimodal Virtual Environments*, chapter Training Approaches for Improving Robot Programming-by-Demonstration Skills, pages 241–252. CRC Press, 2012.

- [107] D. Schröder. *Elektrische Antriebe - Regelung von Antriebssystemen*. Springer, 3rd edition, 2009.
- [108] R. Sepulchre, M. Janković, and P. V. Kokotović. *Constructive Nonlinear Control*. Communications and Control Engineering. Springer London, 1997.
- [109] S. M. Shinnars. *Modern Control System Theory and Design*, chapter Performance Criteria. John Wiley and Sons, Inc., 2nd edition, 1998.
- [110] N. K. Sinha. *Control Systems*. New Age International (P) Limited, 2008.
- [111] T. Sinkjaer, E. Toft, S. Andreassen, and B. C. Hornemann. Muscle stiffness in human ankle dorsiflexors: intrinsic and reflex components. *Journal of Neurophysiology*, 60(3):1110–1121, September 1988.
- [112] W. J. Staszewski and D. M. Wallace. Wavelet-based frequency response function for time-variant systems—an exploratory study. *Mechanical Systems and Signal Processing*, 1(47):35–49, 2014.
- [113] P. Staubli, T. Nef, V. Klamroth-Marganska, and R. Riener. Effects of intensive arm training with the rehabilitation robot ARMin II in chronic stroke patients: four single-cases. *Journal of NeuroEngineering and Rehabilitation*, 6(46), December 2009.
- [114] S. Stramigioli, C. Secchi, A. J. van der Schaft, and C. Fantuzzi. Sampled data systems passivity and discrete port-hamiltonian systems. *IEEE Trans. on Robotics*, 21(4):574–587, August 2005.
- [115] K. A. Stroud and D. J. Booth. *Advanced Engineering Mathematics*. Palgrave Macmillan, 5th edition, 2011.
- [116] T. Tsuji, Y. Takeda, and Y. Tanaka. Analysis of mechanical impedance in human arm movements using a virtual tennis system. *Biological Cybernetics*, 91(5):295–305, November 2004.
- [117] B. Weber, M. Sagardia, T. Hulin, and C. Preusche. Visual, vibrotactile, and force feedback of collisions in virtual environments: Effects on performance, mental workload and spatial orientation. volume 8021 of *Lecture Notes in Computer Science*, pages 241–250. Springer Berlin Heidelberg, July 2013.
- [118] B. Weber, S. Schätzle, T. Hulin, C. Preusche, and B. Deml. Evaluation of a vibrotactile feedback device for spatial guidance. In *IEEE World Haptics Conference (WHC)*, pages 349–354, Istanbul, Turkey, June 2011.
- [119] H. Weiss, T. Ortmaier, H. Maass, G. Hirzinger, and U. Kuehnappel. A virtual-reality-based haptic surgical training system. *Computer Aided Surgery*, 8(5):269–272, 2003.

- [120] R. Weller, M. Sagardia, D. Mainzer, T. Hulin, G. Zachmann, and C. Preusche. A benchmarking suite for 6-DOF real time collision response algorithms. In *ACM Symp. on Virtual Reality Software and Technology*, pages 63–70, Hong Kong, China, 2010.
- [121] J. C. Willems. Dissipative dynamical systems part II: Linear systems with quadratic supply rates. *Archive for Rational Mechanics and Analysis*, 45(5):352–393, January 1972.
- [122] J. W. Yeol, R. W. Longman, and Y. S. Ryu. On the settling time in repetitive control systems. In *Int. IFAC World Congress*, pages 12460–12467, Seoul, Korea, July 2008.
- [123] Y. Yokokohji and T. Yoshikawa. Bilateral control of master-slave manipulators for ideal kinesthetic coupling – formulation and experiment. *IEEE Trans. on Robotics and Automation*, 10(5):605–620, October 1994.
- [124] J. G. Ziegler and N. B. Nichols. Optimum settings for automatic controllers. *Transactions of ASME*, 64:759–768, November 1942.
- [125] C. B. Zilles and J. K. Salisbury. A constraint-based god-object method for haptic display. In *IEEE/RSJ Int. Conf. on Intelligent Robots and Systems (IROS)*, volume 3, pages 146–151, Pittsburgh, PA, USA, August 1995.

